CHEMICAL MODIFICATION BY DOPING OF GRAPHITIC CARBON

AND SILICON BASED ANODE MATERIALS

by

Isabelle Pedersen Gordon

A thesis submitted in partial fulfillment
of the requirements for the degree

of

Doctor of Philosophy

in

Materials Science

MONTANA STATE UNIVERSITY
Bozeman, Montana

December 2023

DEDICATION

Dad, you are always right.

ACKNOWLEDGEMENTS

I would first and foremost like to thank my advisor, Dr. Nicholas P. Stadie, for your mentorship and guidance over the years. It is your meticulous and systematic nature that I believe has guided my research in such an elegant way. You have provided a graduate experience rich with opportunities that I feel so deeply appreciative for. I would like to thank my committee members, Dr. Robert Walker, Dr. Stephen Sofie, Dr. Paul Gannon, and Dr. Jerome Downey for your thought-provoking questions relating to future research directions. I would like to thank all past and present members of the Stadie research group for your collective comradery and exchange of scientific ideas. I would like to specifically thank Wei Xu for pioneering the electrochemistry lab; my research truly flourished under your guidance in all things electrochemistry related. I would like to thank Grace Suenram for your early synthetic efforts on aluminum-doped graphitic carbon. I would like to thank Charles McDaniel and Juan M. Marmolejo-Tejada for running computational calculations. I would like to thank collaborator, Laura Piveteau, for your collection of ssNMR data; I consider this data integral to the phosphorus/carbon story. I would like to thank Dr. Richard T. Jow for your guidance on the silicon project. To all my friends and family close and far, thank you. You have held me during the highs and lows of this process. To my dearest friend, Isabelle, you have so beautifully encouraged me to lean into my feminine intuition in a field that is at times dry and thick with masculinity. Your vibrant energy has propelled me forward. To my brothers, who for the last five years have asked me what exactly it is that I do, I am pleased to be able to present this thesis to you. And lastly, I extend my deepest gratitude to my mom and dad, Ingrid and Richard, for whom without your consistent encouragement, I would be nowhere near to where or who I am today, I love you.

TABLE OF CONTENTS

TABLE OF CONTENTS CONTINUED

TABLE OF CONTENTS CONTINUED

viii

LIST OF TABLES

LIST OF TABLES CONTINUED

LIST OF FIGURES

LIST OF FIGURES CONTINUED

LIST OF FIGURES CONTINUED

LIST OF FIGURES CONTINUED

LIST OF FIGURES CONTINUED

LIST OF FIGURES CONTINUED

LIST OF FIGURES CONTINUED

NOMENCLATURE

BP	Black Phosphorus
CV	Cyclic Voltammetry
DSC	Differential Scanning Calorimetry
EDX	Energy Dispersive X-Ray Spectroscopy
EC	Ethylene Carbonate
GCD	Galvanostatic Charge-Discharge
HF	Hydrofluoric Acid
LIB	Lithium-Ion Battery
NP	Nanoparticle
PAH	Polyaromatic Hydrocarbon
PC	Propylene Carbonate
RP	Red Phosphorus
SEI	Solid Electrolyte Interphase
SOC	State of Charge
SEM	Scanning Electron Microscopy
ssNMR	Solid-State Nuclear Magnetic Resonance Spectroscopy
WP	White Phosphorus
XAS	X-Ray Absorption Spectroscopy
XPS	X-Ray Photoelectron Spectroscopy
XRD	X-Ray Diffraction

ABSTRACT

This body of work investigates the structural, chemical, and electrochemical effects of substitutional doping on three distinct materials systems: phosphorus-doped graphitic carbon, aluminum-doped graphitic carbon, and phosphorus-doped silicon. Success of doping is found to depend on the synthetic route employed (bottom-up or top-down) as well as the selection of dopant with respect to the host material. Al- and P-doped graphitic carbons were prepared by bottom-up pyrolysis of liquid precursors at low to modest temperatures (800-1100 °C). In both cases, doping was found to be challenging to achieve without the formation of byproducts and phase segregation. Efforts to synthesize phosphorus-doped graphitic carbons led to an interesting discovery that the phosphorus allotrope side-product could be controlled by altering the precursor. This work quantifies the relative phosphorus allotropes present (white, red, or a combination thereof) in each composite using a combination of materials characterization techniques. Such materials are interesting lithium-ion anode materials that exhibit the first evidence of the reversible lithiation of white phosphorus, enabled by stabilization of P_4 domains between graphitic sheets. Aluminum-doped graphitic carbon, on the other hand, was found to be extremely difficult to obtain without forming mullite ($3Al_2O_3 \cdot 2SiO_2$) as a byproduct. Nevertheless, we report the first signature of trigonal planar or puckered AlC_3 type doping sites. Lastly, we explored phosphorus-doped silicon materials prepared via top-down solid-state synthesis strategies. Homogenously and heterogeneously doped silicon nanoparticles were obtained by exploring a wide range of synthetic parameters and successful doping was confirmed by X-ray diffraction. Phosphorus doping in dilute quantities (1000 ppm) is found to unambiguously and positively impact the electrochemical performance of silicon as a lithium-ion anode. Ultimately, the work presented in this thesis illuminates the challenges associated with doping by both bottom-up and top-down synthesis strategies while also exploring the electrochemical relevance of chemically-modified graphitic and silicon-based materials.

CHAPTER ONE

INTRODUCTION AND MOTIVATION

Applications of Batteries

The electrification of transportation is acknowledged as one of the most substantial opportunities for mitigating the social and environmental challenges that stem from global warming.[1, 2] The push towards electrification is prompted by advances made within battery technology: notably the rechargeable lithium-ion battery (LIB). Total life cycle emissions (including product manufacturing, production, existence, use and disposal) of internal combustion engine vehicles and electric vehicles (EVs) are respectively 55 and 39 metric tons of CO_2 equivalent.[3] Replacing internal combustion engine vehicles with electric vehicles can reduce CO_2 emissions by ~30%. For this reason, the adoption of EVs is highly incentivized; for example, in the United States over a dozen states plan to ban the manufacturing and sales of internal combustion engine vehicles by 2035.[4] Further, the Bipartisan Infrastructure Law under the Biden Administration has invested $7.5 billion to build 500,000 EV chargers making it more accessible and reliable, more than $7 billion for critical minerals and necessary battery components to make batteries and over $10 billion for clean public transportation.[5] At present, EV batteries predominately utilize lithium-ion technology due to its high energy density (250 Wh kg^{-1}, 600 Wh L^{-1})[6] and long cycle life. Nevertheless, there exist opportunities for technological development aimed at rapid fast charging (80% state of charge in under 15 minutes)[7] and increased mileage range comparable to current internal combustion engine vehicles. This thesis will delve into the advancements and intricacies of lithium-ion battery chemistry pertaining to the anode.

State-of-the-Art Lithium-Ion Battery

The development of the first rechargeable LIB is rich in history, involving numerous scientific contributions, each addressing not only individual cell components but also the eventual chemical compatibility at each component interface. Key components include the anode, cathode, electrolyte, and separator, as shown in Figure 1.1.[8] In a fully charged cell, lithium atoms reside in the anode material. Upon discharging, lithium ions flow through a liquid or solid electrolyte towards the cathode whilst electrons flow in the same direction through an external circuit. The electrolyte facilitates the movement of lithium ions between the electrodes; meanwhile, the separator, typically a thin and porous material, serves to prevent contact between the anode and cathode while still enabling the flow of lithium ions.[6, 8]
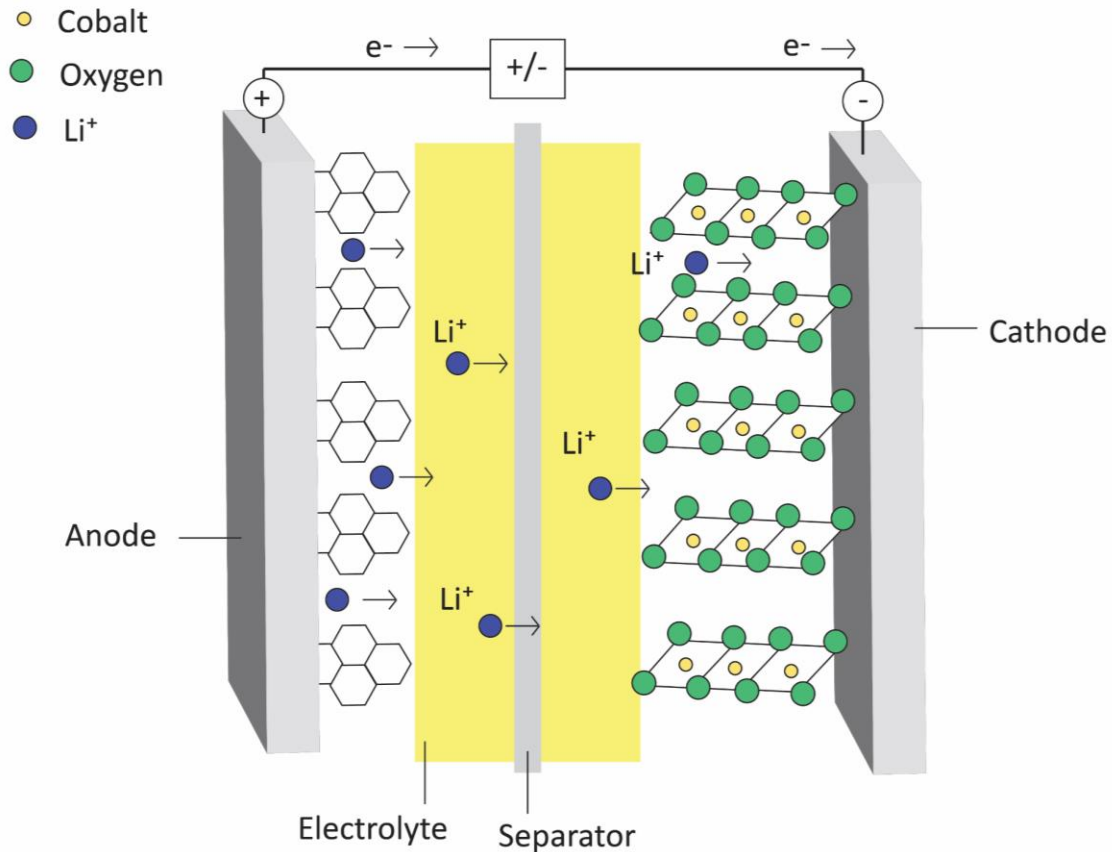
Figure 1.1. Conventional lithium-ion battery containing an anode, cathode, electrolyte, and separator. Upon discharge, lithium-ions flow from the anode to the cathode upon discharge and the electrons flow through the external circuit in the same direction.

The harmonious operation of the rechargeable LIB arose from three major contributions made by Stanley Whittingham, John B. Goodenough and Akiro Yoshino who were eventually awarded the Nobel Prize in Chemistry in 2019 for their finding in the 1970s and 1980s.[6, 8] Whittingham first identified an innovative cathode material, titanium disulfide (TiS_2), capable of housing lithium ions, which in its lithiated state is $LiTiS_2$.[9] This was a crucial development towards rechargeable LIB technology, but at the time was incompatible with the current lithium metal anode and carbonate liquid electrolyte being used in non-rechargeable LIBs.[9] The spirit of Whittingham's work was carried forward by Goodenough who discovered lithium cobalt oxide

(LiCoO$_2$), a layered oxide capable of housing lithium ions while also enabling a higher voltage than previous cathode materials.[8] Shortly after, Yoshino paired the LiCoO$_2$ cathode with a petroleum coke anode, a less graphitized carbon, to make the very first rechargeable LIB.[10] This general technology was commercialized in 1991 by Sony and has since revolutionized our world.[6, 8, 11]

Rocking Chair Battery

Early designs of LIBs utilized pure Li metal (Li$_{(m)}$) as the anode material owing to its high energy density and low potential.[6, 12, 13] It was quickly realized, however, that the intrinsic instability and passivation of pure Li$_{(m)}$ at the anode interface when it reacts with liquid electrolytes leads to a series of safety hazards: most notably dendritic formation, short-circuiting, and the subsequent thermal runoff, which can result in explosions and fire.[12-14] Nonmetal compounds (e.g., Li$_x$M$_n$Y$_m$) which can instead store and exchange lithium ions were adopted to avoid stripping and plating of the Li$_{(m)}$.[14] The most commonly used cathode materials of this form today are lithium cobalt oxide (LiCoO$_2$), lithium manganese oxide (LiMn$_2$O$_2$), Lithium iron phosphorus (LiFePO$_4$, LFP)¸ and lithium nickel manganese cobalt oxide (LiNiMnCoO$_2$, NMC).[15] A cyclical transfer and storage of lithium ions can be achieved when another Li-accepting compound, A$_z$B$_w$, is used as the anode. Equation 1.1 shows the charge and discharge of compounds Li$_x$M$_n$Y$_m$ and A$_z$B$_w$. The "rocking" of lithium ions between electrodes during (dis)charging has been coined as the "rocking chair" battery.[14]

$$(1.1) \quad Li_yM_nY_m + A_zB_w \leftrightarrow Li_{(y-x)}M_nY_m + Li_xA_zB_w$$
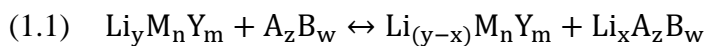
<u>Energy Storage Mechanisms</u>

Li^+ storage is dominated by three mechanisms: intercalation, alloying, and conversion, as depicted in Figure 1.2. Intercalation facilitates the transport of lithium ions in one-, two- or three-dimensional channels with minimal disruption to the electrode structure.[9] Perhaps the most prominent example of an intercalation-based material is graphite whereby lithium ions are stored in the interlayer galleries.[16] [17]Alloying occurs when lithium ions insert into the host material "M" (where M can be either a compound or element) forming new bonds: Li-M.[18] Anode materials that undergo alloying reactions are promising owing to their relatively high energy densities, however, are associated with severe volume expansion during the (de)alloying/(de)lithiation process.[19, 20] Lastly, the conversion mechanism involves binary compounds, M_aX_b, where M and X are metal cations and non-metal anions, respectively (e.g., a metal oxide).[21, 22] Li^+ insertion along with electrons results in complete reduction of the M^+ state to a M^0 state and the subsequent formation of Li-X bonds[21, 23]. The above three mechanisms are highly dependent on the host material structure, morphology, and chemistry and can result in vastly different lithiation capacities. The work presented herein will focus on intercalation and alloying mechanisms in the context of graphitic carbon and silicon-based anode materials, respectively.
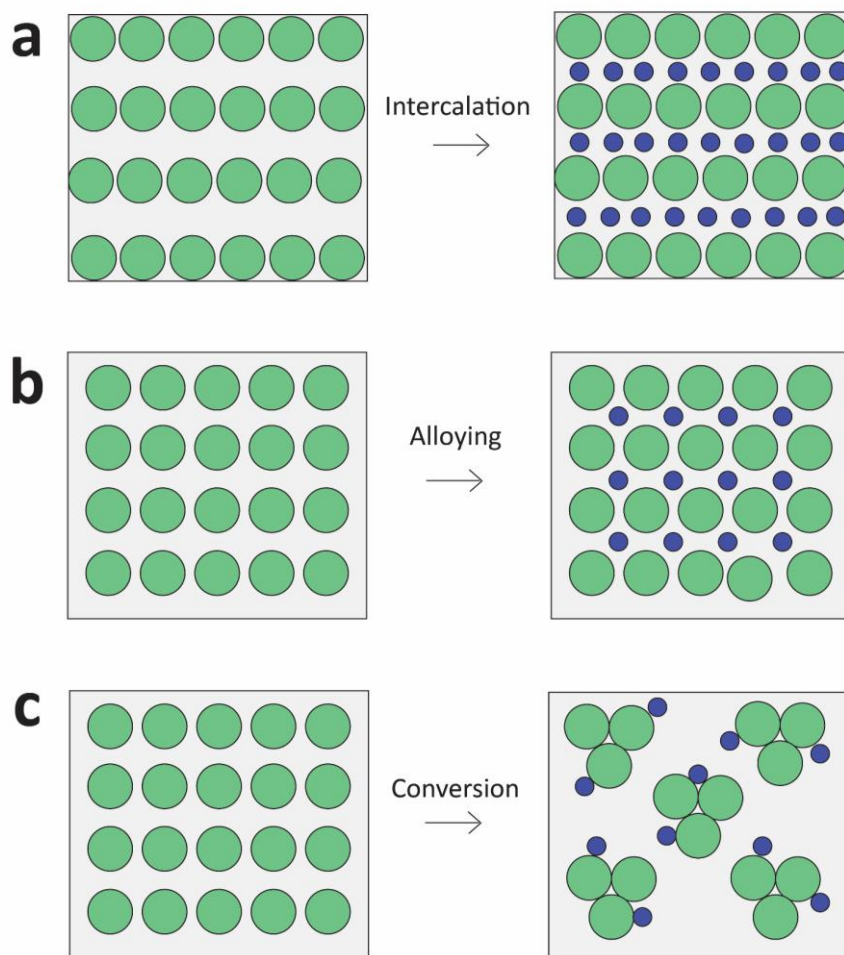
Figure 1.2. Lithium-ion charge storage mechanism; a) intercalation, b) alloying and c) conversion.

Charging Conventions

The meaning and convention of the words, (dis)charging, (de)alloying, and (de)intercalation are relative to the system of discussion. When *charging* in a full-cell, lithium-ions migrate from the cathode to the anode where *intercalation* occurs. Upon *discharging* of the anode *de-intercalation* occurs.[24] It is important to note that in a lithium half-cell configuration, Li_m serves as the anode acting as both the counter and reference electrode and the material of interest

serves as the cathode or working electrode. In this work the above conventions will always be used with respect to the anode material.

The Graphite Anode

Graphite is the conventional LIB anode material owing to its environmental benignity, abundance, strong cycling stability, low intercalation potential (0.01 V vs. Li/Li$^+$) and its modest theoretical capacity of 372 mAh g^{-1} (upon lithiation to LiC$_6$).[11] The structure of graphite, which consists of sp^2 hybridized graphene layers stacked via van der Waals forces in an ABAB stacking sequence, play an important role in the intercalation of lithium.[17, 25] Figure 1.3 shows the structure of graphite and stoichiometric positioning of lithium atoms in graphite.
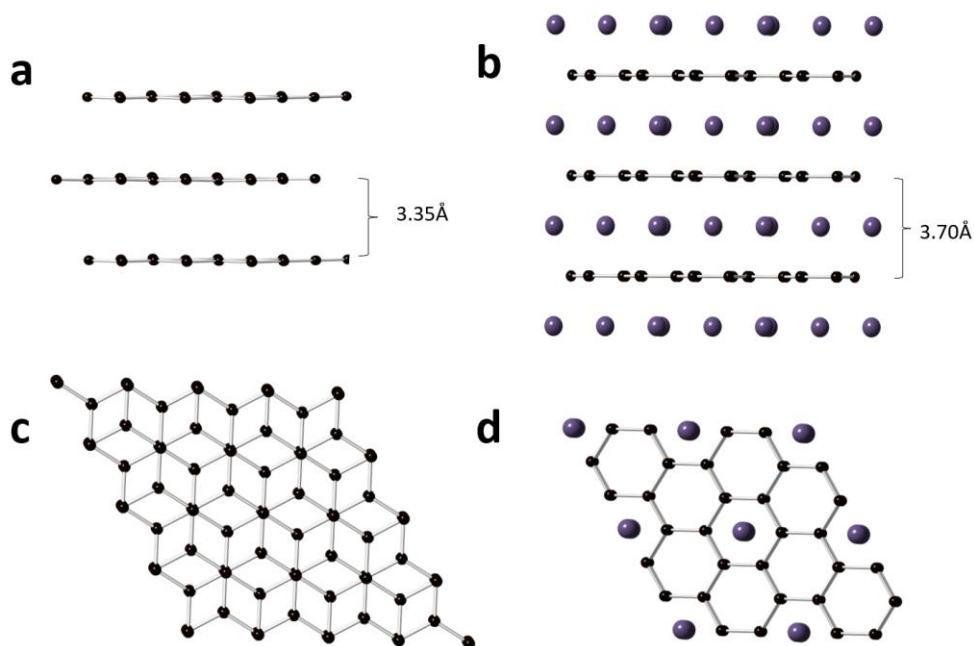
Figure 1.3. Structure of a) crystalline graphite and b) fully intercalated graphite (LiC$_6$) where carbon and lithium atoms are respectively black and purple. (c-d) show graphite and LiC$_6$ from a bird's eye view. Note, when fully lithiated, the graphite structure shifts from an ABAB stacking sequence to AAAA.

Lithium intercalation was known to exist as early as 1975 through molten lithium[26] or compressed lithium powder[25] techniques. Electrochemically reversible lithiation of LiC_6, however, remained a challenge owing to decomposition and co-intercalation of carbonate based liquid electrolytes (i.e., propylene carbonate (PC)) and exfoliation of the graphite sheets.[27] Yazami and Touzain were the first to reversibly intercalate graphite in 1983 with use of a solid polymer electrolyte. Successful reversible intercalation using liquid electrolyte was eventually also demonstrated 1990 with the use of co-solvent ethylene carbonate (EC).[27]

To achieve a maximum stoichiometry of LiC_6, a staging phenomenon occurs whereby lithium ions intercalate into graphite sheets at every nth layer (where n equals an integer number ≥ 1). As the concentration of lithium increases eventually n =1 where every layer is occupied by lithium. This model was first proposed by Rüdorff and Hofmann in 1938 and is illustrated in Figure 1.4.[28] It does not however explain how a material goes from stage 4 to 3 per se and assumes the complete de-intercalation of state 4 and then re-intercalation at stage 3 in order to fill empty graphite sheets. Albert Hérold and N. Daumas attempt to correct for this model suggesting that for stages where n > 1, graphite sheets behave in a flexible manner, in which they can deform and form intercalant islands for lithium ions to move from one layer to another (See Figure 1.4).[17, 29] Still, it remains a matter of question as to how exactly this staging mechanism works.
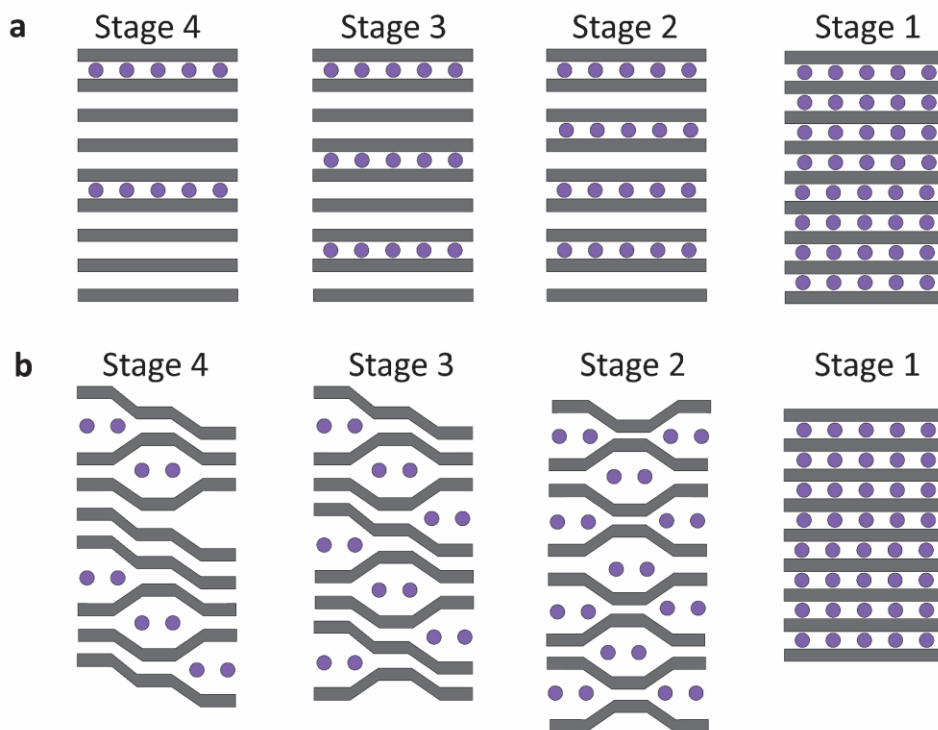
Figure 1.4. Schematic of proposed intercalant staging mechanisms. a) Rüdorff and Hofmann model[28] and b) Daumas-Hérold model.[17, 29]

<u>Limitations and Modifications of the Graphite Anode</u> While graphite has remained the state-of-the-art LIB anode material since its commercialization in the 1990's owing to its structural and electrochemical stability it is limited by relatively low theoretical capacity and rapid charging capabilities when considering the rising energy demand.[11] This is especially true within the electric vehicle (EV) market where desired charging times are <15 minutes.[7] Currently, such necessary rapid charging in the graphite anode is limited by the de-solvation of lithium ions out of solution at the electrolyte-anode interface despite strong diffusion between graphitic sheets (10^{-7}–10^{-6} cm^2 s^{-1})[30], therefore, careful selection of the lithium containing salt and organic based solvents in liquid electrolytes is important. For example, ethylene carbonate (EC) is often paired with LiPF$_6$ salt because of its high solvation ability and more so its formation of stable solid electrolyte interphase

(SEI) at the electrolyte-anode interface.[31, 32] The SEI plays an important role in preventing cointercalation of lithium salt-solvent pairs into graphite which can consequently results in exfoliation of the graphite structure and unstable cycling. [27, 33]

Well known solvents such as propylene carbonate (PC), 1,2 dimethoxyethane (DME) and tetrahydrofuran (THF), can dissolve Li^+ in high concentrations and are suitable for the lithium metal anode but unfortunately are incompatible with the graphite anode due to cointercalation.[33] To overcome undesired cointercalation effects, the use of gylme solvents have been explored to help dissociate and dissolve lithium ions.[34] Another challenge of the graphite anode intimately related to the formation of SEI is irreversible capacity loss on the first cycle and therefore low initial coulombic efficiency. This is a result of reductive electrolyte decomposition and irreversible consumption of Li^+ by SEI formation. Surface modification of graphite particles and careful electrolyte selection attempt to target the issues mentioned above.[35-38]

Many of the above issues associated with the graphite electrode relate to electrolyte selection which affect the formation and behavior of the SEI and thereon overall cell performance. A much more intrinsic limitation of the graphite anode, however, is its limited theoretical capacity of 372 mAh g^{-1} (upon lithiation to LiC_6). Simply replacing the graphite anode with a high-capacity alloying based material, such as silicon, is an option that is being heavily explored but requires new selection and compatibility of the electrolyte, cathode and operating cell voltage.[20, 39, 40] Main focus of the graphite anode material in this work aims to increase the theoretical capacity to meet rising energy demands.

Research Directions Related to the Graphite Anode

The first project presented in this thesis (chapter 4) details structural and chemical modification of turbostratic graphitic carbon by phosphorus doping. Doping under different synthetic parameters, mainly phosphorus containing precursors, leads not only to substitutionally doped carbon but also composite P/C materials. The inherent high capacity of phosphorus domains within the graphitic carbon system was quickly realized with aims to increase the theoretical capacity of graphite while also leveraging high surface area and conductivity of turbostratic graphitic carbon. Chapter 5 addresses aluminum-doped graphitic carbon in an attempt to understand how n-type and p-type dopants affect the resulting structure and chemistry of graphitic carbon. This proved to be much more synthetically challenging and has not yet been studied electrochemically but remains a material of interest for future work.

Pushing the Frontier of the Lithium-Ion Battery

The graphite LIB anode has remained state-of-the-art since its commercialization in the early 1990's beyond those of lead-acid and nickel-metal hydride type batteries; it today exists as our primary energy source in all mobile devices (e.g., smart phones and tablets).[12] To meet rising energy demands graphite is being overlooked in exchange for alternative materials capable of high volumetric/gravimetric energy density and fast rate capabilities. This is particularly important in the electric vehicle market where long range (>300 miles) and short charging times (<15 min) are desired.[41] The Department of Energy (DOE) launched the Battery 500 consortium in 2017 to develop next generation LIBs capable of delivering 500 Wh kg^{-1},[42] where for reference, current graphite-based LIBs are only able to deliver around 220 kW kg^{-1}.[43, 44] Future anode materials of interest are alloy-based (i.e., primarily phosphorus and silicon) due to their large stoichiometric

ratio of lithium they can accommodate compared to intercalation-based materials.[45] Lithium metal, phosphorus and silicon will be discussed as potential anode materials owing to their high energy densities.[12] Particular emphasis will be given to silicon, a primary focal point of this dissertation.

Lithium metal is a long-time contender as an energy dense anode material owing to its high theoretical capacity of 3860 mAh g^{-1} and low standard potential (-3.04 V vs. SHE).[13] Stanley Whittingham was the first to use lithium metal as the negative electrode in the 1970's where he studied the intercalation mechanisms of the TiS_2 positive electrode and founded the concept of intercalation-based materials.[9, 13] The use of lithium metal has, however, been at a standstill since the 1980's owing to safety concerns. During charging/discharging, lithium metal undergoes stripping and platting resulting in dendritic growth.[13] The continuous formation of dendrites further exposes new surfaces to the electrolyte and leads to the continuous formation of SEI and decomposition reactions. Further, dendrites can separate from the active material acting as "dead lithium", contributing to poor coulombic efficiency.[13, 46] Issues associated with dendritic growth can be catastrophic especially if the cell shorts resulting in a cascade of events; high current discharge, rapid heat evolution, fire and/or explosions.[13] To curb the effects of dendritic growth, many have focused on the formation of stable protective layers at the lithium/electrolyte interface that still allows for passivation and diffusion of Li ions.[47-49] Similarly, electrolyte engineering has been studied.[50, 51] Nevertheless, the high reactivity of lithium metal and dendritic formation in liquid electrolyte still pose inherent risk especially when considering flammability and leakage of electrolytes.[12, 13] Replacing standard carbonate liquid electrolyte with solid electrolyte such as ceramic Li-ion conductors demonstrates diminished dendritic growth.[13, 52] There are, however, challenges associated with all solid-state batteries mainly concerning low ionic conductivity of the

solid electrolyte and the interface between solid components.[12, 52] The implementation of lithium metal anodes in either liquid or solid electrolyte batteries still today remains a worthwhile challenge.

Phosphorus has also warranted attention as a promising anode material in LIBs due to its high theoretical capacity of 2596 mAh g^{-1} (as it lithiates towards Li$_3$P), low redox potential, and its elemental abundance within the earth's crust.[12, 53] Furthermore, phosphorus exists in three primary allotropic forms; black P (BP), red P (RP), and white P (WP).[12, 54] BP is the most stable of the allotropes consisting of layered sheets with high in-plane electrical conductivity (~1×10^2 S m^{-1}) and Li$^+$ diffusion channels between the sheets.[55] This material however is challenging to synthesize requiring high pressures (>1.2 GPa) therefore researchers have devoted attention towards RP a more commercially available allotrope but far less conductive (~1×10^{-12} S m^{-1}).[56-58] The use of RP in conductive carbon composite materials can be used to enhance conductivity.[59] Lastly, WP at this point in time, has little to no electrochemical relevance due to its pyrophoric nature.[60] An in-depth overview of phosphorus allotropes, respective structures, and applicability towards lithiation will be given in Chapter 4. Like many alloy-based materials, phosphorus is largely hindered by large volume expansion upon (de)lithiation on the order of 300% resulting in pulverization of the electrode.[61, 62] Attempts to alleviate severe volume expansion involve size engineering, structural hierarchical engineering and most commonly, the formation of composite materials (e.g., ball-milling phosphorus and carbon).[63-65]

The Silicon Anode

As the demand for longer driving range and faster charging times for EV's intensifies, silicon has received increasing attention due to its practical theoretical capacity (3579 mAh g^{-1},

$Li_{15}Si_4$) at room temperature and low voltage window.[12, 20, 66] Like bulk phosphorus, silicon undergoes an alloying storage mechanism during lithiation. Figure 1.5 shows the structures of pure and fully lithiated silicon ($Li_{15}Si_4$). At elevated temperature (415 °C) silicon can achieve an even higher theoretical capacity of 4200 mAh g^{-1} as it lithiates to $Li_{22}Si_5$.[66, 67] Discrete voltage plateaus at elevated temperatures are observed for $Li_{12}Si_7$, $Li_{14}Si_6$, $Li_{13}Si_4$, and $Si_{22}Si_5$ alloy phases.

The Si-Li reaction process is shown in equations 1.1-4.[40] At room temperature when crystalline silicon is lithiated it forms an amorphous Li_xSi alloy. If further lithiated below 0.05 mV (vs Li/Li^+) the Li_xSi alloy transforms to crystalline $Li_{15}Si_4$. Upon delithation of either Li_xSi or $Li_{15}Si_4$ phases, amorphous silicon forms.[18] Pure crystalline silicon is never achieved again in this process.
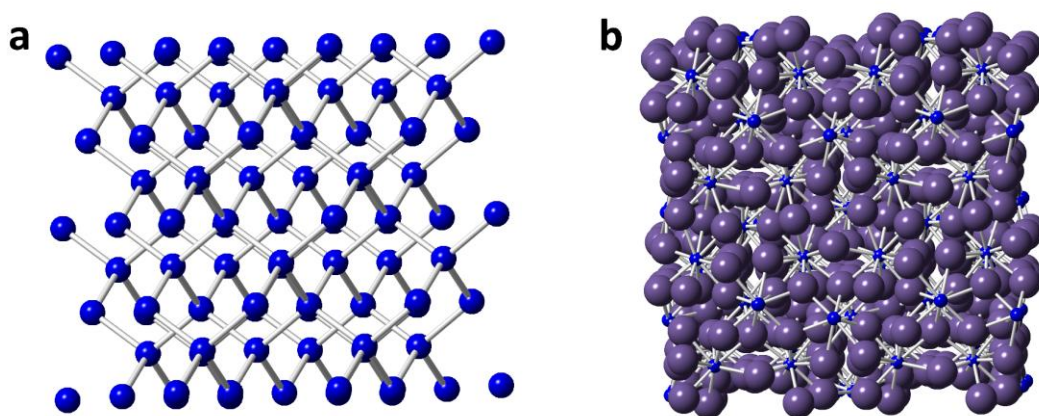
Figure 1.5. crystal structure of a) crystalline silicon and b) $Li_{15}Si_4$. Depiction shows a 2x2x2 unit cell. Silicon and lithium atoms are represented in blue and purple, respectively.

$$(1.1) \quad Si_{(c)} + xLi^+ + xe^- \rightarrow Li_xSi_{(a)}$$

$$(1.2) \quad Li_xSi_{(a)} + (3.75 - x)Li^+ + (3.75 - x)e^- \rightarrow Li_{15}Si_{4(c)}$$

$$(1.3) \quad Li_{15}Si_{4(c)} \rightarrow Li_xSi_{y(a)} + yLi^+ + ye^- + Li_{15}Si_{4(c,residual)}$$

$$(1.4) \quad Li_xSi_{(a)} \rightarrow Si_{(a)} + xLi^+ + xe^-$$
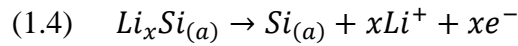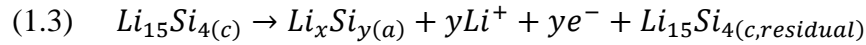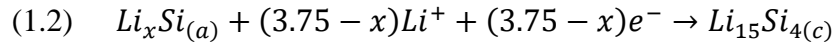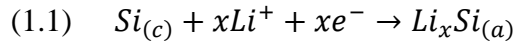
<u>Limitations and Modifications of the Silicon Anode</u> Several challenges exist associated with silicon as an anode material. Most prohibitive is large volume expansion on the order of 300-400 % experienced during (de)lithiation, leading to mechanical stress, pulverization of the electrode, loss of electrical contact with the current collector, reduced life cycle and even cell failure.[40] Repeated mechanical stress on the silicon particles during (de)lithiation can lead to particle cracking and thereon the formation of unstable SEI on the surface of silicon. The cascading events following volume expansion during (de)lithiation of the silicon anode are of serious concern when attempting to scale and commercialize the material: perhaps most concerning is the potential for thermal runaway, a self-accelerating reaction that occurs due to internal reactions and decomposition of the liquid carbonate-based electrolyte which can result in a rapid rise in temperature, release of gas, or even fire and explosions.[68]

Creative solutions attempting to directly control for volume expansion experienced by silicon during (de)lithiation involve size engineering, hierarchical engineering, development of core-shell structures, pre- or partial- lithiation strategies and perhaps most simply, the formation of composite materials. Limitations of the silicon anode are not only limited to volumetric expansion but also the stability between standard carbonate electrolyte, SEI, and silicon surfaces that are responsible for decomposition reactions and thermal runaway. Thermal stability of silicon

is addressed by considering electrolyte selection, surface modifications, and perhaps most interesting and far less explored, stabilization of the silicon lattice through chemical doping.

Nanoengineering of silicon by particle size reduction and structural engineering (i.e., nanowires, nanorods, or porous structures) is advantageous when mitigating volume expansion, lithium induced strain and pulverization. This was first determined by Liu et al., who demonstrated that crystalline silicon particles below a critical size (<150 nm) do not experience particle fracture and cracking.[69] It was later shown by McDowell et al., that amorphous silicon spheres up to 870 nm in diameter do not fracture upon lithiation[70]; this is much larger than the previously reported 150 nm critical particle size. Presently, for crystalline silicon, sub 150 nm nanoparticles hail as a top performing material without pulverization/cracking.[71] Low-dimensional structures such as silicon nano-rods, -wires[72], -tubes, and porous structures[39] can also be used to mitigate radial volume expansion while also enhancing overall electrical conductivity in the one-dimensional direction[72]. Chan et al., demonstrated this concept with nanowires, achieving the theoretical capacity for silicon (4,200 mAh g^{-1} for Li$_{4.4}$Si) on the first cycle with little to no fading within the first 10 cycles between 0.01-2.0 V versus Li/Li$^+$.[72] This excellent performance can be attributed to the core-shell phase distribution of crystalline (core) and amorphous silicon (shell) and enhanced electrical conductivity in the one-dimensional direction of the nanowires.

Nevertheless, from an industry perspective, an important consideration remains regarding scalability of the above-mentioned silicon structures in a commercial setting. For this reason, there is still strong emphasis on large-grain, low-cost silicon electrode fabrication.[73, 74] The use of micro-particle silicon can be accomplished by partial lithiation strategies, where the full capacity of silicon is not fully utilized. For example, macro sized silicon particles (4.5 µm) retain 80% residual

capacity over 250 cycles when lithiated 20% whereas <50 cycles when lithiated 70%.[74] Partial lithiation of silicon results in lower overall capacities but corresponds to smaller volume expansion and generally electrochemical longevity.[75]

Thermal runaway during cycling is another limiting factor towards the commercialization of the silicon anode unless containing very low silicon loadings (<20% silicon in carbon composites). Current mitigation practices involve careful battery management systems where cells are carefully monitored and deconstructed based on their electrochemical performance and physical state (i.e., temperature and/or SOC). Material-based solutions are far less explored. Chemical modification by doping alkaline earth metal and/or p-block heteroatom dopants is a proposed method to increase stability of nano-silicon phases. For example, it has been shown that the incorporation of small amounts of aluminum into $Li_{15}Si_4$ lead to the formation of $Li_{15-x}Al_xSi_4$ (0.4 <x<0.8) which is stable up to 700 °C.[76] In contrast, $Li_{15}Si_4$, has a limited stability window, decomposing at 200 °C. This prompted further exploration of magnesium and zinc dopants to form $Li_{14}MgSi_4$ and $Li_{14.05}Zn_{0.95}Si_4$ phases.[76] In both cases incorporation of dopants in low quantities (5.2 at% Mg, 4.7 at% Zn) show increased thermal stability and shifted decomposition temperature by more than 400 °C.[76] Another study further expanded on the above stable Li-M-Si ternaries and demonstrated incorporation of M dopants (M=Mg, Zn, Al, and Ca) via electrochemical cointercalation using $M(TFSI)_x$ as secondary salts in the electrolyte.[77] Significant stabilization in these systems was observed leading to improved coulombic efficiencies, longer cyclability and improved capacity retention.

Research Directions Related to the Silicon Anode

Herein, we attempt to stabilize the silicon lattice by chemical doping of phosphorus (chapter 6) and later explore alternative dopants (chapter 7). The primary goal of the work is to identify the role of substitutional doping on the silicon lattice towards electrochemical properties, as decoupled from other properties such as particle size and distribution of the dopant. Homogenous and heterogenous doped materials are obtained over a wide range of synthetic parameters (phosphorus composition (at%), temperature set point (°C), ramp rate (°C min^{-1}), dwell time(h)) through a facile solid-state synthesis. Indeed, improved capacity retention and cycling stability is observed when silicon is doped with phosphorus. Questions in this work remain as to what mechanism, mechanical stabilization, thermal stabilization, or combination thereof, gives rise to increased stability.

CHAPTER TWO

CHEMICAL MODIFICATION OF MATERIALS VIA DOPING

Structural and Chemical Modification to Materials

Structure-property relationships of materials are heavily influenced by synthesis and processing techniques including but not limited to chemical treatment[78-80], electrochemical treatment,[81-83] surface modification[84, 85] and thermal treatment.[85-87] Several ingenious discoveries based on materials modifications has vastly advanced our technology today, for example allowing for the development of optoelectronic,[88, 89] photovoltaic[90, 91] and semiconductor applications.[78, 92] A common strategy within materials modification efforts is elemental doping, involving the addition of impurity elements to a crystalline lattice in small quantities (e.g., in the parts per million (ppm) scale).[93] Structural changes due to doping of such materials are reflected in gradual changes in the lattice parameters, change in level of crystallinity, and in atomic positions and symmetry. From a chemical perspective, dopants can alter electric, thermal and optical properties.[94] A very famous application of doping is in the realm of electronic materials for semiconductor and photovoltaic applications. The p-n junction, a crucial building block of electrical circuits, would not be possible in our devices today without using doping.

Herein we investigate doping as a "tuning knob" to chemically modify materials properties in silicon- and graphitic carbon-based materials for electrochemical applications. Three primary materials systems interconnected by the common theme of doping are presented in this thesis; phosphorus-doped silicon, phosphorus-doped graphitic carbon and aluminum-doped graphitic carbon (Figure 2.1). This chapter outlines several accepted definitions of doping (and identifies

one that is adopted herein), and broadly treats aspects of doping theory as well as synthesis strategies to carry out doping in the laboratory.
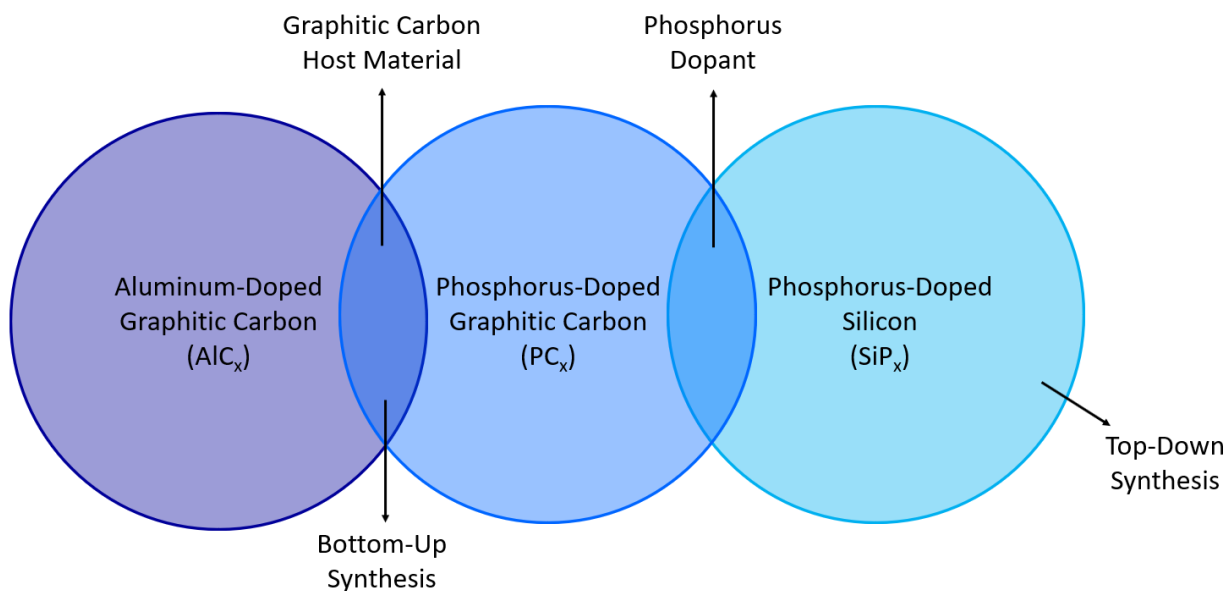
Figure 2.1. Venn diagram showing similarities among phosphorus-doped silicon, phosphorus-doped graphitic carbon, and aluminum-doped graphitic carbon.

<u>Definitions of Doping</u>

Doping can widely be defined as the substitution of a host atom with an impurity atom within a crystalline lattice. An early example of doping was performed by American physicist John Robert Woodyard during his work on radar technology during World War II.[95] He discovered that the addition of small quantities of phosphorus, antimony, or arsenic into pure germanium improved performance of semiconductors.[96] Findings from this work were patented in 1950 and laid the groundwork for doping in the semiconductor industry first by solid-state diffusion methods and later by ion-implantation or a combination thereof.[96, 97] Since then, doping has become a widespread strategy for the modification of many different types of materials including organic[98]

or inorganic materials,[78, 94] 2D films,[88, 99] nanomaterials,[100] biomaterials[101] and so on; simultaneously, doping strategies have become far more creative beyond traditional substitutional doping used in the semiconductor industry and include chemical doping,[102] charge-transfer doping,[103] molecular doping,[92, 98] formation of hybrid composites by nanoparticle decoration,[104, 105] and surface functionalization.[106, 107] When defining doping of a particular system one must consider the physical nature of the dopant as well as quantity and concentration.

The physical nature of the dopant is varied across different communities and materials; for example, from the solid-state perspective, a dopant can be considered a small-sized atom that diffuses through a crystalline lattice and occupies either an interstitial or substitutional site. This is very different from molecular doping of organic semiconductors where dopants of molecular size drive a charge transfer across the difference in energy between the highest occupied molecular orbital of the dopants and the lowest unoccupied molecular orbital of the organic semiconductor.[98] Noncovalent interactions in the form of molecular dopants are also applied to physisorption of gas molecules and metal ions.[108, 109] This is particularly advantageous for thin film materials, such as graphene, where structural and electrical integrity of the material is preserved while also producing p- or n-type structures. A drawback of surface doping, however, is lack of stability owing to the reversible adsorption and desorption processes.[99] Another form of doping is defect doping in which defects can act as an intrinsic dopant site or serve to attract dopants. Lastly, and perhaps most ambiguous, is "doping" by nanoparticle decoration on a materials surface. This is commonly cited in the hydrogen storage community, for example, where palladium nanoparticles are dispersed on a material's surface.[105, 110, 111] This form of doping often results in large micron sized regions of

agglomerated nanoparticles doped on a material's surface and arguably strays away from conventional doping of a single atom or molecule.

Doping concentration must also be considered; in the semiconductor industry doping concentrations on the order of parts per million (ppm) is satisfactory to alter intrinsic charge carriers within a material and thereby its electronic structure. For instance, the introduction of just one boron atom into 1×10^5 silicon atoms increased the electrical conductivity by 10^3.[93] Other reports of doping, however, dope on the order of 1-25 at%.[65, 112-114] At these larger concentrations it is important to discern the differences between doping, surface decoration, and formation of composites or even new phases altogether. For example, the difference between doping silicon with 3 at% and 6 at% phosphorus under identical synthesis conditions leads to in one case a solid solution of phosphorus-doped silicon and in another the formation of a silicon phosphide (SiP) phase.[115] When dealing with a completely miscible binary solution, however, doping at high concentrations is possible. The silicon-germanium binary system is a famous example of this where up to 50 at% silicon can be doped in germanium at which point silicon becomes the majority component and germanium would then act as the dopant.[116]

The definition of doping is largely up to interpretation given the various strategies and concentrations within different materials systems. We caution overuse of the word doping without clear vision of the goal at hand. In this thesis we are focused on substitutional doping which we define as the substitution of a host atom with an impurity atom. The electron donating (n-type) and withdrawing (p-type) character of the dopant atom with respect to the host material is of interest as well as structural modifications to the materials based on the atomic size of the dopant. Dopant concentrations are varied based on the materials system; heteroatom doped graphitic carbon

materials explore the high end of doping concentrations ($\sim \leq 25$ at%) to study metastable phases. Doping in silicon explores low dopant concentrations (0.1 at%) and are selected based on solubility limits of the binary system at hand.

Substitutional Doping

Substitutional doping is best understood from a solid-state perspective whereby dopant atoms diffuse through a material and occupy lattice sites of host atoms. A counterpart to substitutional dopants are interstitial dopants which occupy interstitial sites in a crystalline lattice. Both can form solid-solutions whereby the atomic structure of the host material is unchanged and the dopant is accommodated non-homogenously. For the purposes of this work, we will focus on substitutional solid-solutions. The formation of a substitutional solid-solution is largely guided by the Hume-Rothery rules which state that the dopant and host atoms must have similar size, electronegativity, crystal structure, and valency.[117] The difference in ionic radius of the dopant atom and host atom must be less than 15% (equation 2.1). A famous example of a fully miscible solid-solution is the silicon-germanium system in which both elements have a diamond cubic crystal structure, a valence of 4 and similar atomic radii (111 and 125 pm respectively) and electronegativity (1.90, and 2.01, respectively). In many cases, however, the solubility of the dopant atom is limited, for example, as in the case of phosphorus-doped silicon (discussed in chapter 6). The Hume-Rothery rules best apply to metal and ceramic systems but are generally a good rule of thumb when determining the successful addition of dopants to a material system.

$$(2.1) \quad \frac{r_{dopant} - r_{host}}{r_{host}} \times 100\% \leq 15\%$$

Theory of Substitutional Doping

Diffusion Mechanisms Substitutional doping can be achieved by several different synthetic routes (discussed in the *Synthesis of Substitutional Doping*), however, most simply it is understood from the perspective of solid-state diffusion in a crystalline lattice described herein. In a periodic crystal, host atoms reside at distinct lattice sites: when provided sufficient thermal energy for lattice vibrations, host atoms, interstitial atoms and vacancy sites can swap places allowing for the diffusion of dopants.[118, 119] Figure 2.2 shows relevant host, substitutional, interstitial and vacancy sites within a periodic crystal lattice. The diffusion of dopants occurs by three primary mechanisms; the vacancy mechanism, the direct interstitial mechanism, and the interstitialcy mechanism.[117] In the vacancy mechanism, substitutionally incorporated dopants can diffuse to an open vacancy site. To avoid continuous swapping between the same vacancy and substitutional sites, the vacancy must move to at least a third-neighbor site away from the dopant.[118] It is traditionally assumed that for phosphorus-doped silicon, the phosphorus diffusion in silicon obeys a vacancy-mediated mechanism,[120] however, conflating studies suggest interstitial-mediated mechanism to dominate.[118, 121] In the direct interstitial mechanism, foreign atoms migrate through the lattice by diffusion between interstitial sites. Interstitial mediated impurities typically have small ionic radii and are fast diffusers.[122] Ultimately, literature on phosphorus-doped silicon agrees it is a combination of the vacancy and direct interstitial mechanisms that allow for phosphorus doping.[123] Lastly, the interstitialcy mechanism combines host atoms, dopant atoms, vacancy sites, and interstitial sites; interstitial atoms can replace a substitutionally doped site thereby creating a new interstitial in the form of the dopant. The interstitial dopant can now repeat this "kick-out" process by creating a new interstitial site and so on. It is harder to assign one of these mechanisms

to phosphorus- or aluminum-doped graphitic carbon owing to bottom-up pyrolysis synthesis which is not inherently diffusion controlled.

a) Host site
b) Substitutional site
c) Vacancy site
d) Interstitial site
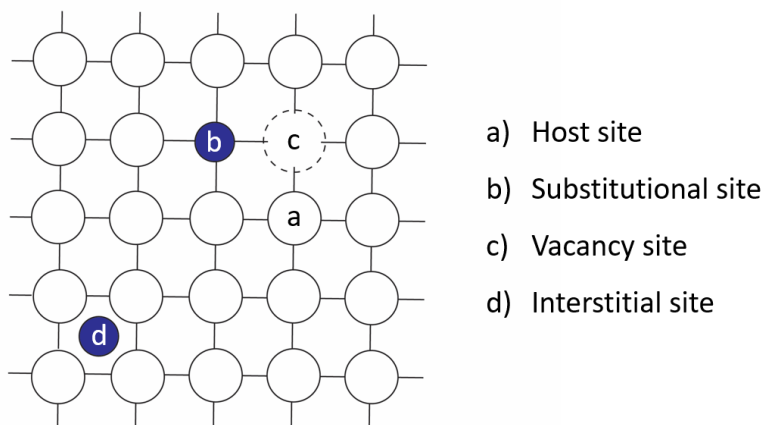
Figure 2.2. Relevant host, substitutional, interstitial and vacancy sites within a periodic crystal lattice.

Electronic Structure Semiconductor materials in their pure state have a band gap between the conduction and valence band. The probability that electrons will occupy either the conduction or valence band are equal and defines what is known as the Fermi level.[93] At any time, the number of electrons and hole carrier concentrations are equal, where the carrier concentration is the conduction band's number or electrons per unit volume or the valence band's number of holes per unit volume.[93, 124] The addition of dopants artificially controls for the number of charge carriers through the intentional addition of either electron donating (n-type) or electron withdrawing (p-type) dopants.[93, 124] In silicon, for example, the addition of pentavalent (i.e., As, P, Sb) and trivalent (i.e., Al, B, Ga) dopants shift the fermi level towards the conduction and valence band respectively. In this thesis we explore phosphorus doping in both graphitic carbon and silicon anode systems. We expect phosphorus's electron rich nature with respect to graphite and silicon to attract

positively charged lithium ions (or other alkali metals). A third system examined is aluminum-doped graphitic carbon in attempts to elucidate the effects of n-type and p-type doping on similar bulk graphitic systems.

Synthesis of Substitutional Doping

Synthesis strategies to achieve substitutional doping fall under two classes: top-down and bottom-up synthesis. A top-down synthesis is the modification of already existing bulk material whereas bottom-up involves reactions on the atomistic level to build desired materials.[125-127] Classically, top-down and bottom-up refer to the synthetic route to achieve a nanomaterial (1-100 nm size).[125, 128] In this work we refer to bottom-up and top-down simply as the pathway to the final material irrespective of resulting size. When incorporating phosphorus or aluminum into graphitic carbon (chapter 4 and 5) we rely on bottom-up synthesis whereby chemical precursors are pyrolyzed and the resulting structure and incorporation of dopants can be controlled by the synthesis reaction, temperature, dwell time, and ramp rate etc. To achieve phosphorus-doped silicon (chapter 6) a top-down strategy, solid-state diffusion, is used to incorporate phosphorus into already existing silicon powder at elevated temperatures (1100-1200 °C).

Bottom-Up Approach Bottom-up synthesis is based on self-assembly at the atomic and molecular scale allowing for synthetic control over resulting materials.[125, 129] Common bottom-up synthesis strategies include pyrolysis,[100, 130] chemical vapor deposition (CVD),[131, 132] and hydrothermal templating (sol-gel).[133] Pyrolysis is a common method explored by the Stadie group to synthesize turbostratic graphitic carbon material derived by benzene or polyaromatic hydrocarbon (PAH) precursors.[134-137] Simultaneous incorporation of dopants can be achieved through the addition of other chemical precursors. Simply, pyrolysis is the thermal decomposition

of chemical precursors at elevated temperatures under inert atmosphere. Successful incorporation of dopants into the graphitic-lattice have been shown to be related to the decomposition energies of each precursor whereby, when close in decomposition energy it is more likely the dopant is incorporated upon formation. This was experimentally demonstrated in boron-doped graphitic carbon for a nominal stoichiometry of BC_3; materials synthesized with boron tribromide showed better boron incorporation compared to diborane and decaborane.[135] Findings from this work are supported by thermochemical analysis where benzene (the carbon containing precursor) and boron tribromide have similar decomposition energies of 9.1 eV per carbon atom and 8.8 eV per boron atom, respectivley.[135] Pyrolysis is a relatively simple bottom-up synthesis technique that allows for careful control of resulting material structure and chemistry by tuning synthetic parameters including temperature, ramp rate, dwell time, pressure of reaction and chemical precursors. A more intricate technique is chemical vapor deposition (CVD) involving the flow of volatile precursors over a wafer at elevated temperatures and under vacuum. Reacted precursors deposit on the wafer while any byproducts formed flow though the reaction chamber. CVD is commonly used in the semiconductor industry to produce thin films and more recently in the last decade has gained traction for controlled synthesis of large-area and high-quality graphene.[99, 102, 126, 132] Nitrogen-doped graphene, for example, is attainable by CVD using a transition metal catalysis wafer (Cu or Ni) where a reactive mixture of carbon (CH_4, C_2H_4) and nitrogen (NH_3 or N_2) precursors are introduced at temperatures between 700-1000 °C.[131] In-situ growth of nitrogen-doped graphene happens upon dissociation and precipitation of carbon and nitrogen precursors. Typical nitrogen incorporation is ~0.2-6.0 at%.[131] CVD synthesis of thin films has also been adopted towards three-dimensional carbon materials such as zeolite template carbon (ZTC) or carbon nanotubes

(CNTs).[138-140] Other bottom-up strategies include hydrothermal (sol gel) templating or solvothermal methods.[141-143] For the synthesis of heteroatom doped graphitic carbon materials we rely on a co-pyrolysis method owing to its inherent single-step simplicity as well as oxygen-free nature.

Top-Down Approach Top-down synthesis strategies targeting substitutional doping include ball-milling, ion-implantation or heat treatment. Generally top-down synthesis techniques are affordable, easily controlled, and simple from a scalability perspective.[125, 126] Ball-milling is carried out by high energy mechanochemical milling of powdered materials. It is often used to reduce particle size but can also be used to introduce new chemical bonds in the case of elemental doping.[144] From a silicon anode manufacturing perspective, this is quite desirable and has proven successful at introducing new covalent bonds to silicon systems for enhanced lithiation kinetics and overall conductivity.[64, 65] Another bottom-up approach is ion-implantation. In this technique dopant atoms are charged to behave as ions, accelerated by an electric field (1-3000 keV) and directed at a target material (typically a silicon wafer) for implantation.[97] Upon entering the target material, ions undergo a series of collisions with host atoms until they lose energy and come to rest in either interstitial or vacancy sites.[119] These collision events lead to lattice disruption and implantation-induced crystal damage which can be remedied by high temperature post implant annealing under optimal temperatures (900-1100 °C).[97] Penetration depth of dopants can be determined by the dopant, substrate material and accelerating voltage. With many tunable parameters and the precise and reliable nature of ion-implantation, it has become the primary technique used in silicon semiconductor chip manufacturing. One of the simplest bottom-up strategies, however, is solid-state synthesis which involves the heating of two solid reactants to

high temperatures.[121, 145] In this work we rely on solid-state diffusion of phosphorus into silicon

powder at low to medium temperatures (800-1200 °C) to achieve substitutionally doped silicon.

CHAPTER THREE

MATERIALS SYNTHESIS AND PRIMARY CHARACTERIZATION TECHNIQUES

Synthetic Goals and Themes

Fundamental synthesis goals of this dissertation are to explore how substitutional doping affects materials structure and chemistry. A single direct-step ampule synthesis is used for all materials presented herein where a wide range of synthetic parameters (e.g., temperature set point, ramp rate, dwell time, chemical precursors, reaction pressure, and mols of reactant) can be fine-tuned, allowing for investigation of systematic trends within material structure and chemistry. To solely investigate the role of the dopant it is important to mitigate oxygen impurities and oxygen containing functional groups. This principle is best upheld in this work through the selection of oxygen-free chemical precursors and performing synthesis under inert conditions.

Bottom-Up Synthesis Routes to Heteroatom-Doped
Graphitic Carbon

Heteroatom-doped graphitic carbon materials are synthesized via a single-step "direct" method from liquid or solid precursors, following previously established protocols.[134, 136, 137] It should be highlighted that this synthesis is completely air-free (including the use of oxygen-free containing precursors), as to minimize structural and chemical modifications from oxygen impurities and functional groups. Chosen chemical precursors (benzene and a phosphorus or aluminum containing halide) are mixed in appropriate molar ratios and charged into quartz ampules under inert conditions in an argon filled glovebox (<0.5 ppm O_2 and <0.5 ppm H_2O). Molar ratios of chemical precursors are determined based on maximum synthesis temperature and

pressure conditions and relevant reaction schemes (Appendix A). Note that all materials are referred to as their nominal composition; for example, aluminum-doped graphitic carbon would be referred to as AlC_x where x represents the molar ratio of Al:C in the initial reaction mixture, whereas, the total measured phosphorus content is how much aluminum is incorporated into AlC_x after synthesis and workup. A Swagelok ultra-torr adapter will be placed over the open end of the ampule which will then be removed from the glovebox and partially submerged in liquid nitrogen to solidify the precursor solution. The quartz ampule will then be connected to a stainless steel Schlenk line and evacuated to 1×10^{-3} mbar before being flame sealed under vacuum. Figure 3.1 shows the Schlenk line set up. The sealed ampule will then be placed on an elevated platform in the center of a chamber furnace and heated to low to medium pyrolysis temperatures (800-1100 °C) via a programmable PID controller. The temperature setpoint will be held for 0-2 hours and then the sample will be allowed to cool to below 100 °C at which point the furnace can be opened and the ampule removed. The sealed ampule will then be carefully opened using a diamond blade saw in a fume hood where gaseous byproducts (e.g., H_2 or X_2 where X= Cl, Br, I) will be released. The solid product will be collected in a filter fret and rinsed with deionized water and acetone, and finally air dried at 80 °C for 24 hours before further analysis.
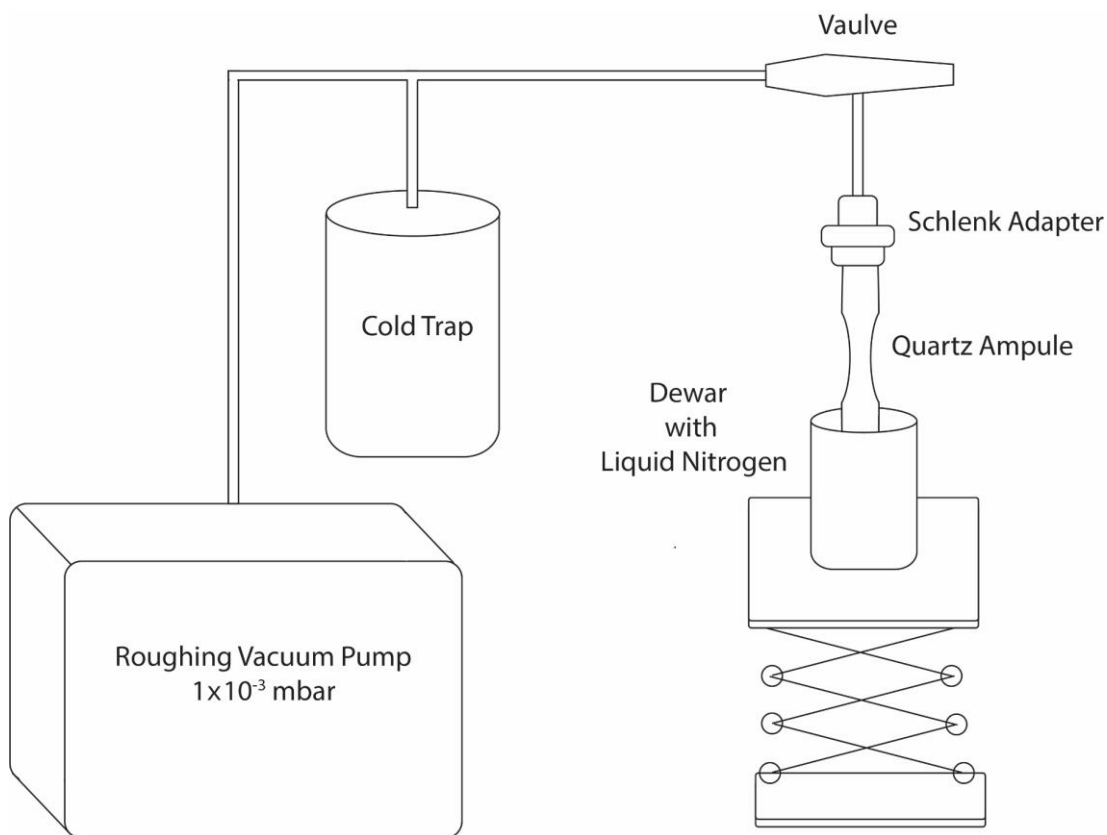
Figure 3.1. Schematic of the Schlenk line setup.

<u>Top-Down Synthesis Routes to Doped Silicon</u>

Synthesis of "M" doped silicon (where M = Al, B, Mg, P, or Zn) utilizes the same ampule synthesis method as described in *Bottom-Up Synthesis Routes to Heteroatom-Doped Graphitic Carbon* with several modifications; most notably, the use of powder precursors instead of liquid.

Commercially available silicon powder is mixed with "M" dopants under solid-state conditions whereby dopant concentration is determined by maximum solubility and temperature setpoint is determined by the eutectic temperature unless retrograde solubility exists. For example, the maximum solubility of phosphorus in silicon is 3 at% and can be achieved at 1131 °C. This composition and temperature were selected as initial synthesis parameters. See Appendix B for the relevant Si-"M" phase diagrams, eutectic temperatures, and maximum solubility limits.

Silicon and "M" powders are prepared by a dilution series (10, 1.0, and 0.1 at% mixtures) to ensure homogeneity using a mortar and pestle for 5 minutes under inert conditions in an argon filled glovebox (<0.5 ppm O_2 and <0.5 ppm H_2O). SiM_x powder is carefully transferred from the mortar and pestle into a quartz ampule using plastic flexible spatulas. Procedures for transferring and sealing the ampule are the same as for heteroatom-doped graphitic carbon materials; a Schlenk adapter is placed over the top of the ampule, transferred out of the glove box, submerged in liquid nitrogen, connected to the Schlenk line and evacuated. The sealed ampule is placed on an elevated platform in the center of the chamber furnace and heated to low-medium temperatures (800-1200 °C) via a programmable PID controller. The temperature set point will be held for 0-2 hours and then the sample will be allowed to cool to below 100 °C at which point the furnace can be opened and the ampule removed. The sealed ampule will then be carefully opened using a diamond blade saw in a fume hood. SiM_x powder is collected and stored before further analysis.

Characterization Techniques

A host of characterization tools are used to assess structural, chemical, and electrochemical modifications to graphitic carbon and silicon materials by doping. This section outlines the most routine characterization techniques including powder X-ray diffraction (XRD), Raman spectroscopy, elemental dispersive X-ray spectroscopy (EDX), scanning electron microscopy (SEM), galvanostatic charge-discharge (GCD) and cyclic voltammetry (CV).

Structural Characterization

Powder X-Ray Diffraction Powder XRD is used to assess overall crystallinity, phase composition and crystallographic properties (e.g., interlayer spacing and crystallite size). Incident

X-rays elastically scatter off atoms within materials. When constructive interference occurs, Bragg's law (shown in Equation 3.1) is satisfied and the relative intensities and scattering angles of crystallographic planes are measured by a detector,[117] where n is the order of reflection, λ is the wavelength of incident energy, d_{hkl} is the d-spacing between crystallographic planes and θ is the scattering angle. The interlayer spacing between two adjacent planes with indices (*hkl*), referred to as d_{hkl}, is calculated along a line perpendicular to the planes. The lattice parameter of simple cubic materials can then be determined using Equation 3.2 where a is the lattice parameter.[117]

$$(3.1) \quad n\lambda = d_{hkl} 2 \sin \theta$$

$$(3.2) \quad a = d_{hkl}\sqrt{(h^2 + k^2 + l^2)}$$

Graphitic materials exhibit two main features centered at $2\theta = \sim 26°$ and $\sim 44°$ (using Cu Kα radiation) which represent the (002) and (10l) family of planes in graphite. The full width half maximum (FWHM) of these reflections can be used to assess the crystallite size of the graphitic carbon via the Scherrer equation (Equation 3.3); in many cases the 101 and 100 are possible to individually resolve, allowing for a determination of relative crystallinity along the a/b (in-plane) and c (layer-to-layer) axes independently. K is the geometric factor (0.94), λ is the incident wavelength, β is the FWHM and θ is the Bragg angle.

$$(3.3) \quad L = \frac{K\lambda}{\beta \cos \theta}$$

In the silicon system the (111) reflection, centered around $\sim 28°$ (using Cu Kα radiation), is of most interest owing to its high symmetry. Successful doping of silicon is determined by shifts in the (111) reflection corresponding to either an expansion or contraction of the lattice. Change

in FWHM of the (111) reflection is examined as a function of doping concentration (e.g., crystallization of the silicon lattice) and synthesis temperature.

Figure 3.2 shows typical XRD patterns for crystalline graphite and silicon presented in this work. When comparing pure crystalline graphite to turbostratic graphite, broadening of the (002) peak and a shift to lower 2θ is observed corresponding to decreased crystallite size and increased d-spacing, respectively. These metrics will be used in assessing structure and relative crystallinity in both graphite and silicon systems presented herein.
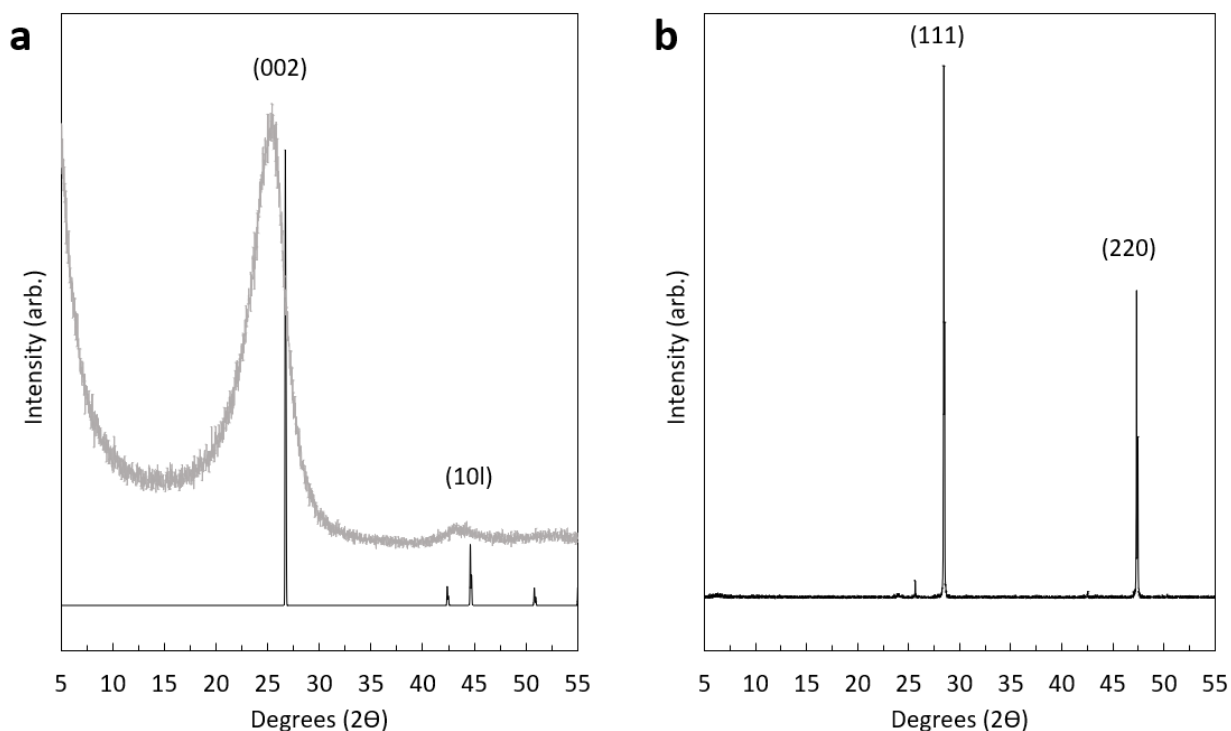
Figure 3.2. Standard XRD patterns of pure graphite (black trace), turbostratic graphitic carbon (gray trace) synthesized by pyrolyzing benzene at 800 °C with a 1 °C min⁻¹ ramp rate and 1 hour dwell time, and b) crystalline silicon.

Raman Spectroscopy Raman spectroscopy will be used as a complementary technique to further elucidate the detailed structural characteristics of the graphitic and silicon lattice. Raman

spectroscopy relies on inelastic scattering of a monochromatic light source in the visible to ultra-violet range on a materials surface. The change in energy between incident photons and scattered photons is a Raman shift. When the energy of the scattered photon is less than that of the incident photon the Raman shift is called Stokes scattering; whereas, when the energy of the scattered photon is greater than that of the incident photon the Raman shift is called anti-Stokes scattering. For a material or molecule to be Raman active it must undergo a change in polarizability during vibration.

Raman spectra of graphitic materials exhibit two prominent features in the 800-2000 cm^{-1} range: the D peak (~1350 cm^{-1}) and the G peak (~1580 cm^{-1}).[146] The D peak is present in sp^2 hybridized carbon domains containing defects and arises from the "breathing" mode of 6 membered rings. The G peak arises from the concerted motion of C-C bonds in any graphitic lattice and is always present (with or without defects). The peak positions, peak FWHM, and the $I_{(D)}/I_{(G)}$ ratio will be used to determine how graphitic structure changes as a function of substitutional doping, the precursors used, synthesis temperature, and overall material composition. Key features of a graphitic Raman spectra are highlighted in Figure 3.3. Graphitic materials at the most disordered end of the graphitization trajectory exhibit distinct Raman features and combinations of features that allow much more detailed characterization than permissible by XRD alone.

The Raman spectrum of silicon shows one distinct feature between 480 and 520 cm^{-1} depending on crystallinity: highly crystalline silicon materials have a sharp band at 520 cm^{-1}, whereas, the band for amorphous silicon is broad and centered around 480 cm^{-1}. Raman spectra is complementary to XRD patterns in assessing crystallinity of commercially available silicon powders. Successful doping of the silicon lattice can be corroborated with Raman spectroscopy

based on a shift in the Silicon band. The shift in band position can be related to Hooke's law which states that the frequency of the vibration of a spring is related to the mass and the force constant of the spring. Therefore, the difference in vibration between Si-Si bonds a Si-P bonds within a Si lattice should results in shift towards lower wavenumbers. Figure 3.3 shows a standard Raman spectrum for crystalline silicon.
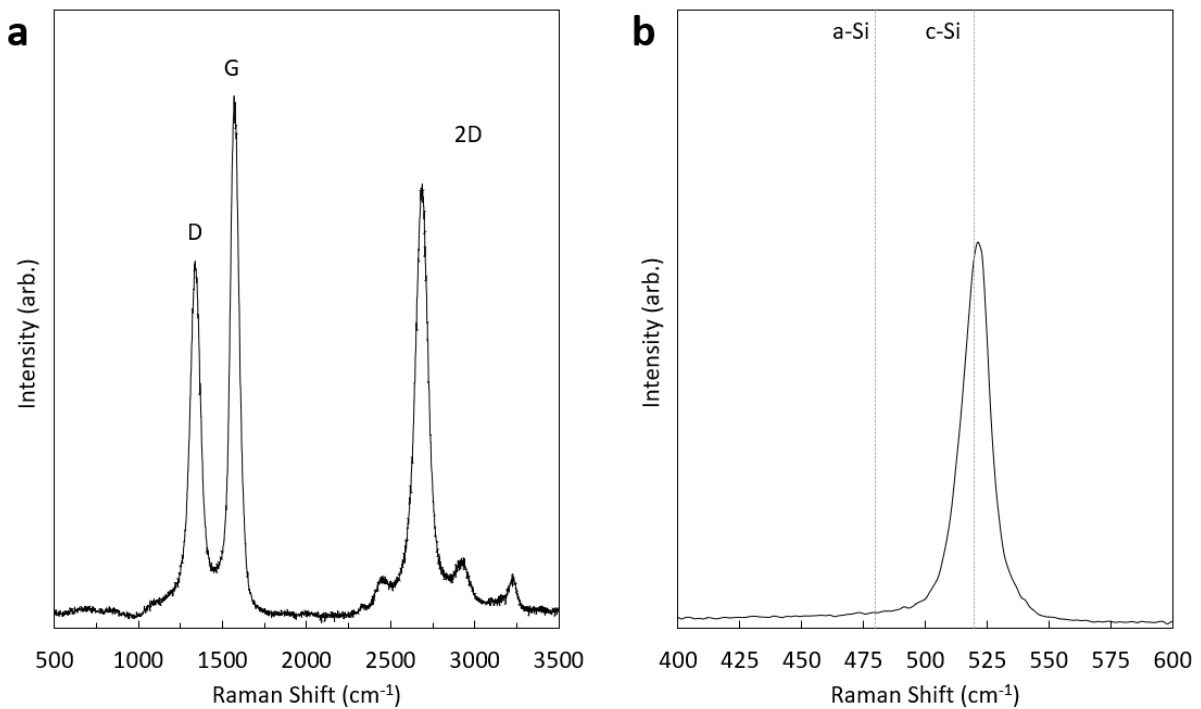
Figure 3.3. Raman spectroscopy and main features of a) graphitic carbon and b) crystalline silicon.

Chemical and Morphological Characterization

SEM coupled with EDX will be used to assess the morphology and composition of materials obtained in this work. A high energy electron beam is applied to the sample which generates secondary electrons, backscattered electrons, and characteristic X-rays. Secondary electrons and backscattered electrons are detected to produce contrast in the generation of SEM

images. An EDX detector will be used to resolve the emitted X-ray energies, providing the quantitative chemical composition of materials and especially, individual morphological features such as flakes, spheres, crystalline surface impurities, etc. These two techniques combined provide both qualitative and quantitative information on material morphology, elemental composition and elemental mapping.

Energy Dispersive X-Ray Spectroscopy Elemental composition of materials can be determined via EDX spectroscopy. In this technique an incident beam is generated using high voltage (10-20 kV) and accelerated onto the sample surface under vacuum (10^{-5} mbar). The incident beam probes the bulk material and with sufficient energy from the incident beam electrons in the core shell or inner shell of an atom are excited and ejected from the inner shell creating a hole. Electrons from an outer shell fill the hole and the difference in energy between the high energy and low energy shell is released in the form of an X-ray. The discrete energy of X-rays released and detected are specific to each individual element and can be used to identify and quantify relative atomic compositions.

Scanning Electron Microscopy SEM is used in a similar fashion to EDX except with a lower accelerating voltage (1-2 kV) to produce an electron beam that interacts with the material surface. Secondary and backscattered electrons are emitted by atoms excited by the electron beam

and are detected using a secondary electron detector. Image resolution can be on the order of several nanometers.[147]

Electrochemical Characterization

Electrochemical techniques are adopted not only to access material performance in secondary lithium-ion batteries but also as a characterization tool to understand subtle differences in material chemistry.

Galvanostatic Charge-Discharge Galvanostatic charge-discharge (GCD) is useful in assessing long term cycling, stability, and coulombic efficiency. A current at a constant rate (i.e., 1 A g^{-1}) is applied between a predetermined voltage window, where the total charge stored at each voltage is then measured. GCD data can be displayed in numerous ways, the two most common in this work are to look at voltage profiles and cycling stability as shown in Figure 3.4. Voltage profiles containing distinct plateaus are representative of a distinct (de)lithiation chemistry. For example, graphite exhibits three distinct voltage plateau's corresponding to different staging mechanisms of lithium in interlayer galleries.[148]
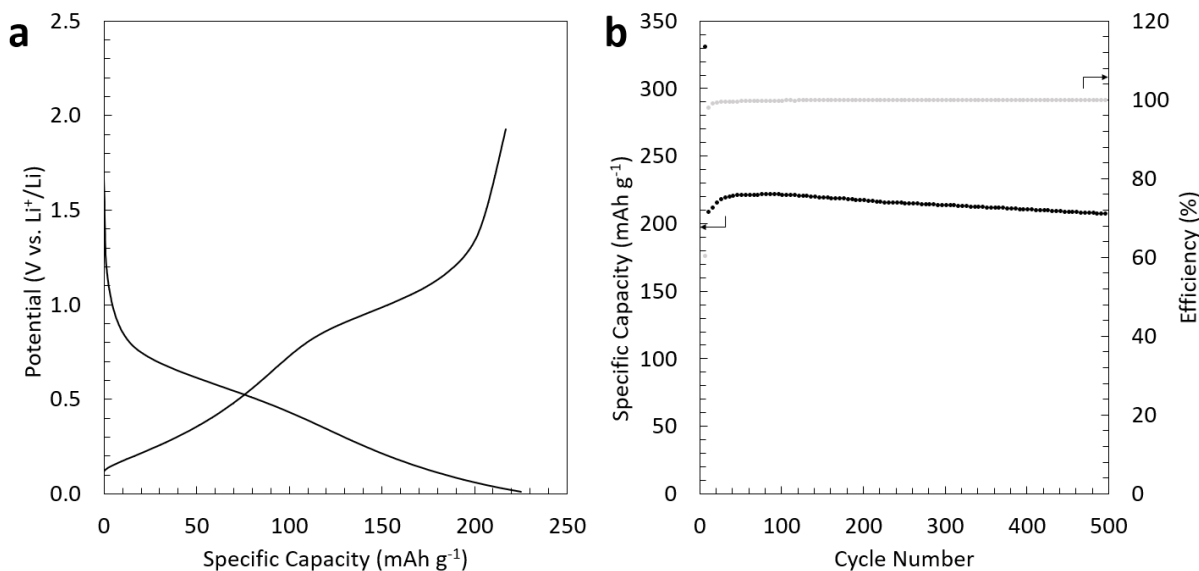
Figure 3.4. a) GCD voltage profile of a single charge-discharge cycle and b) GCD cycling stability over 500 cycles of disordered graphitic carbon in a lithium-ion half-cell.

Cyclic Voltammetry Cyclic voltammetry (CV) is used to study unique redox pair chemistries upon (de)lithiation. It uses a sweeping scan rate (typically 0.1 mV s^{-1}) across a predetermined voltage window. Potential is swept negatively from a starting potential, E_i, to a switching potential, E_f, which is called a cathodic trace. The scan is then reversed positively and is referred to as the anodic trace. During (de)intercalation or (de)alloying reactions between the ion (Li$^+$) and the active material a rapid increase, or decrease in current, is measured and highlights electrochemically relevant reactions in the system. The shape of cyclic voltammograms are useful in determining faradaic, capacitive and pseudocapacitive storage mechanisms as shown in Figure 3.5. Faradic storage is represented by a duck shaped cyclic voltammogram where peaks represent distinctive redox chemistries. In contrast, capacitive materials are more box-like in nature indicating charge can rapidly be stored on the surface of material where no intercalation or alloying reactions occurs.[149] This technique is used to determine reversible (de)lithiation of phosphorus (Li

→ Li$_3$P) within graphitic/phosphorus composite systems. Scan rate is also examined to assess kinetic limitations.
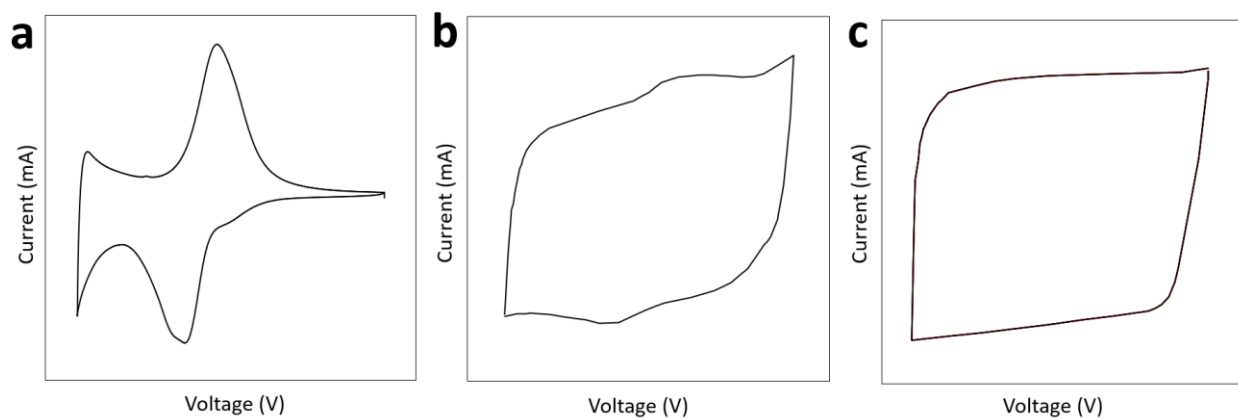
Figure 3.5. cyclic voltammogram shapes (a) faradic, (b), pseudocapacitive, and (c) capacitive.

CHAPTER FOUR

CONTROL OF PHOSPHORUS ALLOTROPES IN PHOSPHORUS-DOPED GRAPHITIC CARBON

Introduction

Graphite is the current state-of-the-art LIB anode due to its low voltage of lithium intercalation, abundance, and safety; however, its storage capacity is limited to 372 mAh g^{-1} as LiC$_6$.[11] Several significant advantages can be expected by replacing graphite with a heteroatom-doped graphitic carbon[112, 133, 150] or composite material.[12, 40, 151-153] This class of anode material has been demonstrated to have higher capacity and rate capability owing to structural and electronic modifications of the graphitic lattice, making such materials very promising next-generation battery anodes. In this body of work, we initially focus on a strategy at the far end of the simplicity spectrum: heteroatom-doping of the graphite anode. Phosphorus has been selected as the heteroatom dopant of choice due to its electron-rich substitutional environment within the graphitic lattice which should serve to attract cation intercalants such as lithium and thereby increase energy storage capacity. Notably, we discover an intimate synthetic relationship between heteroatom doping and phosphorus/carbon (P/C) composite formation which can be structurally and compositionally tuned by the modification of synthetic parameters. The inadvertent discovery of P/C composite materials leads to unique and exciting electrochemical performance. This work will shed insight into the mechanism of charge storage in P/C composite anodes of varying composition and disorder to guide future understanding of electrochemical energy storage across wide-ranging applications.

Phosphorus Incorporation into Graphitic Carbon

Our past work, aimed at substitutional phosphorus-doping of graphitic carbon, revealed that the co-pyrolysis of benzene and PCl_3 at temperatures between 800-1050 °C was only partially successful at achieving graphitic lattice substitution; in addition, partial phase segregation led to the formation of P/PC_x composites (here, PC_x refers to the solid-solution, turbostratic graphitic phase) with a significant content of phosphorus in the form of white phosphorus (WP) (See Figure 4.1).[134] In general, phase segregation in such reactions occurs due to poorly compatible thermal decomposition profiles of the co-pyrolysis precursors.[135] An initial goal of the work presented herein is to control for substitutionally incorporated phosphorus in graphitic carbon by exploring the role of thermal decomposition profiles of the phosphorus precursor. Previous efforts using PCl_3 were extended herein to include the higher halide precursors with lower cracking temperatures: PBr_3 and PI_3 (see Figure 4.2 and Table 4.1). We hypothesize phosphorus halide precursors containing better leaving groups (e.g., iodine > bromide > chloride) drive the reaction forward and allow for phosphorus incorporation into graphitic carbon during co-pyrolysis; this effect is also observed by inspecting the trend in enthalpy of formation of the phosphorus trihalides, as shown in Equations 4.1-4.3.
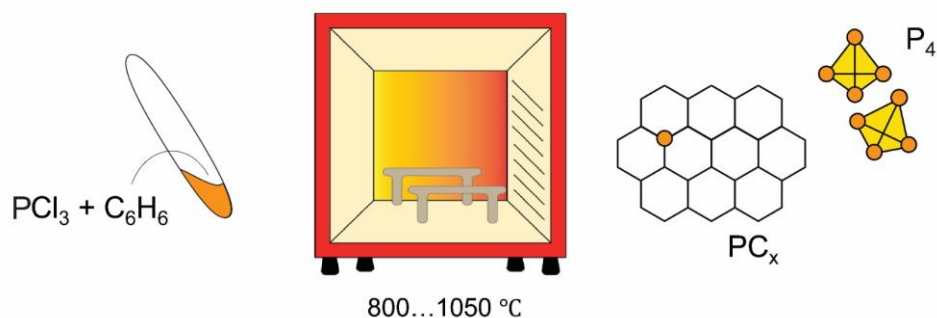
Figure 4.1. Bulk phosphorus-doped graphitic carbon synthesized from liquid precursors (benzene and phosphorus trichloride) at low to medium pyrolysis temperatures (800-1050 °C).[134]
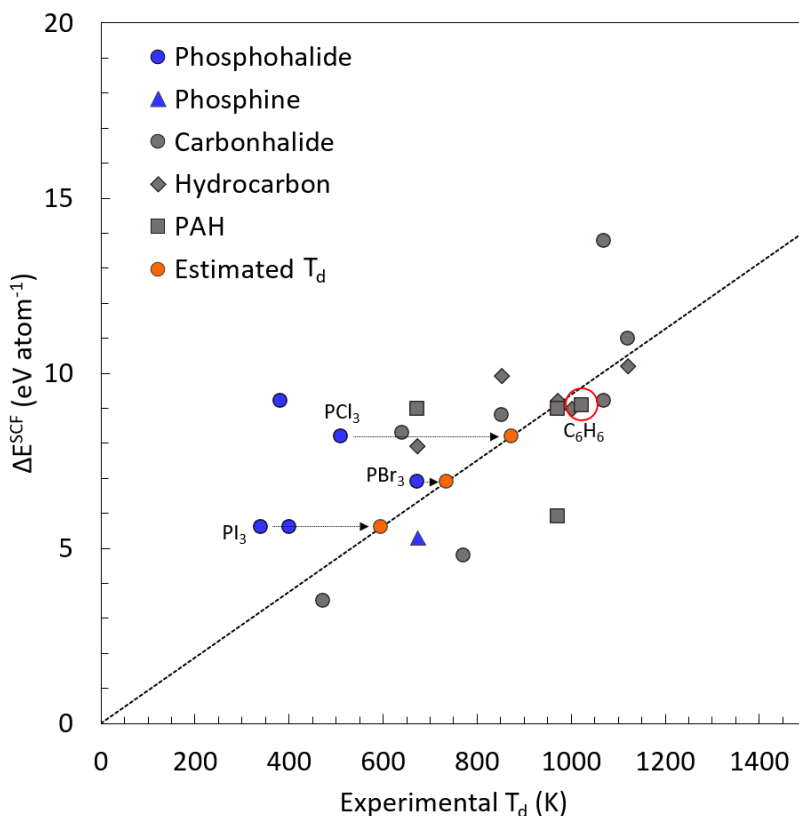
Figure 4.2. Theoretical decomposition energies and experimental decomposition temperatures of several phosphorus and carbon precursors. Note: the decomposition energies (ΔE^{SFC}) are normalized per atom of relevance (P or C). The expected correlation (dashed line) is adapted from previous work.[135]

Table 4.1. Decomposition energies (ΔE^{SFC}), experimental decomposition temperature (T_d), and corresponding references for small molecules of interest in co-pyrolysis reactions to produce phosphorus- and carbon-containing products.

Decomposition Reaction	ΔE^{SFC*} (eV atom^{-1})	Experimental T_d (K)	Experimental SI Reference
$CF_4 \rightarrow C + 2F_2$	13.8	1073	135
$C_6F_6 \rightarrow 6C + 3F_2$	11	1123	135
$CH_4 \rightarrow C + 2H_2$	10.2	1123	135
$C_2H_6 \rightarrow 2C + 3H_2$	9.9	853	135
$C_6Cl_6 \rightarrow 6C + 3\ Cl_2$	9.2	1073	135
$C_3H_6 \rightarrow 3C + 3H_2$	9.2	973	135
$2PCl_5 \rightarrow 2P + 5Cl_2$	9.2	383	154
$C_6H_6 \rightarrow 6C + 3H_2$	9.1	1023	135
$C_2H_4 \rightarrow 2C + 2H_2$	9.0	1003	135
$C_{10}H_{10} \rightarrow 10C + 5H_2$	9.0	673	135
$C_{24}H_{12} \rightarrow 24C + 6H_2$	9.0	973	135
$C_6Br_6 \rightarrow 6C + 3Br2$	8.8	853	135
$C_6I_6 \rightarrow 6C + 3I_2$	8.3	643	135
$2PCl_3 \rightarrow 2P + 3Cl_2$	8.2	512	155
$C_2H_2 \rightarrow 2C + H_2$	7.9	673	135
$2PBr_3 \rightarrow 2P + 3Br_2$	6.9	673	156
$C_{10}H_8 \rightarrow 10C + 4\ H_2$	5.9	973	135
$2PI_3 \rightarrow 2P + 3I_2$	5.6	340.5	157
$P_2I_4 \rightarrow 2P + 2I_2$	5.6	403	157
$2PH_3 \rightarrow 2P + 3H_2$	5.3	673	158
$CCl_4 \rightarrow C + 2Cl_2$	4.8	773	135
$CBr_4 \rightarrow C + 2Br_2$	3.5	473	135

*Note: the decomposition energy (ΔE^{SFC}) is normalized per heteroatom of relevance (C or P)

(4.1) $PCl_3 \rightarrow P + \frac{3}{2}Cl_2$ $\Delta H^{\circ}_{rxn} = 287.0 \text{ kJ mol}^{-1}$

(4.2) $PBr_3 \rightarrow P + \frac{3}{2}Br_2$ $\Delta H^{\circ}_{rxn} = 146.02 \text{ kJ mol}^{-1}$

(4.3) $PI_3 \rightarrow P + \frac{3}{2}I_2$ $\Delta H^{\circ}_{rxn} = 24.7 \text{ kJ mol}^{-1}$
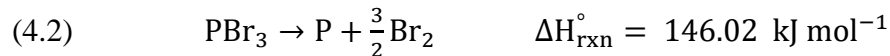
Control over Phosphorus Allotropes

We discover that controlling for substitutional phosphorus doping is challenging: by altering the phosphorus containing precursor a diversity of P/C products with the phosphorus component ranging from exclusively WP inclusions to phase segregated red phosphorus (RP), and linear combinations thereof are obtained. Herein materials are referred to as P/C-1:x-PX$_3$ were 1:x denotes the molar ratio of P:C and PX$_3$ represents the halide (PCl$_3$, PBr$_3$, and PI$_3$). Bottom up co-pyrolysis between benzene and PCl$_3$ leads to solid solutions of phosphorus-doped graphitic carbon and significant WP content determined by X-ray photoelectron spectroscopy (XPS) and ^{31}P solid-state nuclear magnetic resonance (ssNMR).[134] WP content was found to be stabilized within the graphitic domains, protected from oxidation in air.[134] It remains unknown whether that P$_4$ content exists as isolated intercalant-type molecular species or whether larger P$_4$ nanodomains exist that warrant labelling such materials as WP/carbon composites. By altering the halide precursor to PBr$_3$ and keeping all other synthetic parameters the same, a new material (P/C-1:x-PBr$_3$) was discovered which contains both WP and RP. Lastly, materials synthesized by PI$_3$ precursor leads to the formation of RP but in much lower quantities. The work presented herein attempts to understand why changing the phosphorus containing precursor drastically alters the structure and chemistry of resulting P/C composite materials.

Types of Phosphorus Allotropes Phosphorus exists in over a dozen allotropic forms;[54, 159] paradoxically, the most common form, white phosphorus (WP), is also the least thermodynamically stable. Upon heating to 300 °C, WP is slowly converted to amorphous RP, which is both denser and less reactive. Under pressures of >1.2 GPa and with modest heating to 200 °C, RP is converted to the densest and most thermodynamically stable allotrope: black

phosphorus (BP).[54] Figure 4.3 shows the various phosphorus allotropes and synthetic pathways. Owing to phosphorus's high theoretical capacity (2596 mAh g^{-1}, Li_3P) upon lithiation it is of high interest as an anode material. Further, unique electrochemical benefits arise from each allotropic structure (shown in Figure 4.4), particularly BP and RP. Herein the three most common allotropes of phosphorus (RP, BP, and WP) will be discussed from a structural and electrochemical perspective.

Figure 4.3. Synthetic diagram of phosphorus allotropes. Figure adapted from elsewhere.[54]
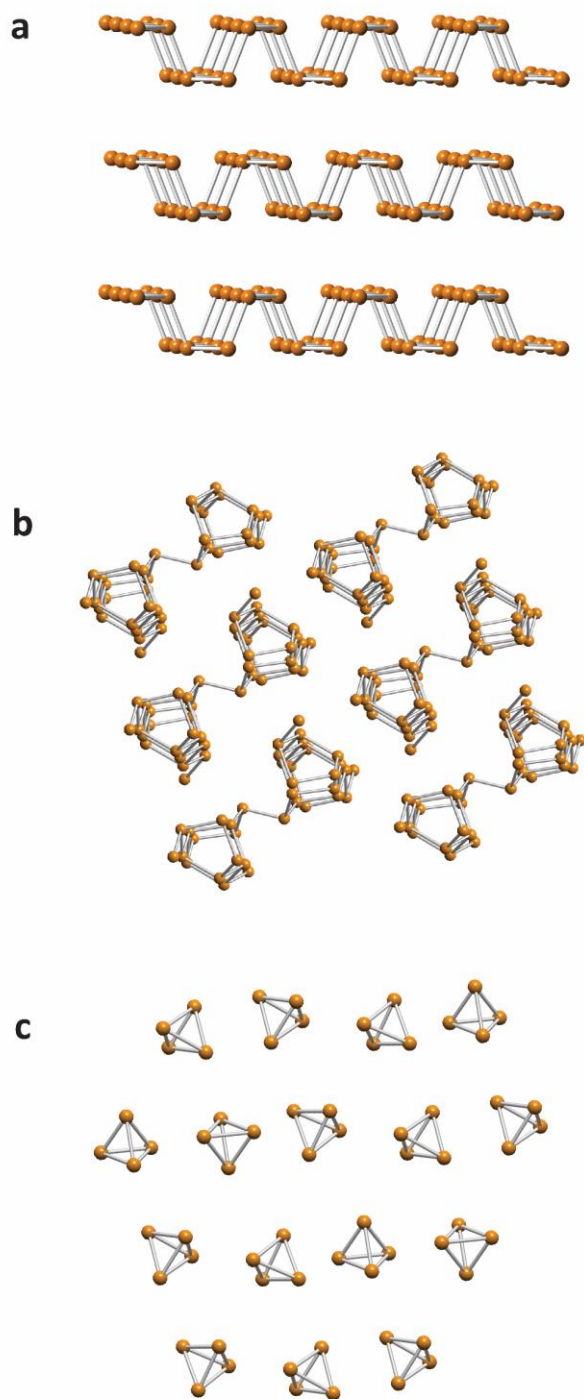
Figure 4.4. Structure of the three primary allotropes of phosphorus; a) orthorhombic black, b) red, and c) white phosphorus.

Orthorhombic BP is well suited as a neat phosphorus allotrope for electrode applications. Similar to graphite, BP is a semiconducting, layered solid that exhibits a modest electrical conductivity ($\sim 1 \times 10^2$ S m^{-1}).[160] Hence, electrochemical studies have revealed well-defined lithiation/sodiation pathways for BP involving anisotropic volumetric changes.[55] While BP has classically been prepared via high pressure routes (1.2 GPa),[161] recent progress has shown high-quality crystals to be accessible at low pressures by heating RP to 600 °C in the presence of gold, tin, and tin(IV) iodide.[162] Owing to its higher crystalline density than RP, the large volumetric expansion of BP inevitably remains an important challenge in the use of BP as a neat electrode material and therefore attention has been primarily directed towards RP-carbon composites to realize the large capacity of phosphorus for energy storage applications.

Many past investigations of phosphorus as an alkali metal ion storage material have focused on RP owing to its stability and ease of handling in air. While several crystalline forms of RP exist, it is most commonly obtained as an amorphous solid; all forms comprise a polymeric network of chains and/or tubes of five-and six-membered rings with low electrical conductivity ($\sim 1 \times 10^{-12}$ S m^{-1} [57, 163]). Hence, pure RP exhibits relatively slow electrochemical lithiation and sodiation reactions and is therefore studied primarily in the context of composites with more electrically conductive matrices.[164, 165] Other challenges in the use of RP as a neat electrochemical energy storage material include large volume expansion upon lithiation/sodiation (243 and 384%, respectively, see Appendix C) and unstable SEI formation.[53, 58] Numerous researchers have instead focused on synthesizing RP-graphite and other carbon-containing composites which benefit from the conductivity of graphitic carbon and the high capacity of phosphorus,[59, 151-153, 166, 167] in a similar strategy as for silicon. Top-down synthesis approaches such as ball-milling are the most common

route to obtaining RP-carbon composites.[151, 165, 168, 169] In summary, representative such composites containing ~70-80 wt% P have been reported to acheive 960-1890 mAh g^{-1} of capacity (normalized to the entire active mass of the composite) within the first 10 to 300 cycles, [57, 151, 165, 168, 169] along with a reduction in volume expansion and higher conductivity compared to that pure RP.

Far less or no attention has been paid to WP as an electrochemical lithium- or sodium-ion storage material. The molecular allotrope of phosphorus, WP is typically an off-white, waxy solid whose structure consists of isolated P_4 tetrahedra, most commonly crystallized in cubic symmetry at room temperature (denoted as α-P_4).[170] Due to high angular strain within the tetrahedral bonding arrangement and the strong thermodynamic driving force associated with the formation of P–O bonds, WP is highly pyrophoric, though it can be stored in liquid water upon forming a robust passivating oxide layer. WP has been shown to have been stabilized within self-assembled tetrahedral capsules[60] and carbon nanotubes[171]. Nevertheless, its high reactivity in addition to its significant toxicity[54] typically preclude WP from consideration as a standalone electrode material. To date, no studies of the lithiation of neat WP have been reported.

Utilizing Phosphorus in Lithiation

The unique and interesting structural P/C composites have not yet been explored in terms of reactivity towards lithium. Bulk elemental phosphorus is known to have a high theoretical capacity of 2596 mAh g^{-1} upon lithiation to Li_3P.[12] We predict that WP and RP domains may be utilized as an additional medium for lithiation (in addition to the graphitic carbon itself), capable of charge storage far exceeding that of phosphorus-free graphitic materials. For example, P/C-1:5-PCl_3 (assuming 50% phosphorus is substitutional and 50% forms as a stabilized P_4) can be expected to have a theoretical capacity of 699 mAh g^{-1} as shown in Equations 4.4 and 4.5. It is not

understood whether substitutionally incorporated phosphorus undergoes alloying similar to bulk elemental phosphorus to achieve a theoretical capacity of 2596 mAh g^{-1} (Li$_3$P). It is suspected that perhaps only one or two lithium ions alloy with the incorporated P.

$$(4.4) \quad P_4C_{20} + 4(PC_5) + 18Li^+ + 18e^- \rightarrow 4(Li_3P) + Li_3C_{20} + Li_4(PC_5)_4$$

$$(4.5) \quad Q_c = \frac{n \cdot F}{M_w} = \sim 699 \text{ mAh g}^{-1}$$

Primary Aims

In our own past efforts to synthesize phosphorus-substituted graphitic carbon via bottom-up reactions between benzene and PCl$_3$, we discovered that such solid-solutions could not be prepared without also forming a significant content of P$_4$ as an impurity.[134] The first aim of this work is to control for substitutional doping (in the absence of P$_4$) by altering the phosphorus containing precursor (-PCl$_3$, -PBr$_3$ and -PI$_3$). Unsuccessful in our attempt we instead discover control over the formation of WP and RP. Two questions arise from this finding; first, what are the relative quantities of WP and RP in resulting P/C composite materials and secondly, can P/C composites be utilized electrochemically. The observed intimate connectivity between RP/WP and the electrically conductive graphitic matrix led to the hypothesis that reversible electrochemical lithiation of phosphorus content in such composites may be feasible. Using a combination of materials characterization and electrochemical techniques we are able to quantify the relative amounts of WP and RP and total lithiable P content.

Synthesis and Characterization of Phosphorus-Doped Graphitic Carbon/Composites

<u>Materials Synthesis</u>

A series of phosphorus-carbon composite materials (P/C) was synthesized via the direct pyrolysis of benzene in the presence of a phosphorus trihalide precursor (either PCl_3, PBr_3, or PI_3) in a closed system at 1050 °C, based on a previously described approach.[134] A quartz ampule (inner ⌀ 0.8 mm, length ~20 cm) was charged with a mixture of benzene (anhydrous 99.8 %, Sigma Aldrich) and PX_3 (where X = Cl (99.999%), Br (99.0%), or I (99.0 %), Sigma Aldrich) inside a glovebox under inert argon conditions (< 0.5 ppm H_2O, < 0.5 ppm O_2). Each mixture consisted of ~0.09mL of benzene and a corresponding amount of PX_3 to achieve a desired overall P:C atomic ratio, while limiting the maximum pressure to < 20 bar. A Swagelok ultra-torr adapter was then placed over the open end of the ampule and the closed ampule was removed from the glovebox. After partial submersion in liquid nitrogen to solidify the benzene/PX_3 mixture, the ampule was connected to a stainless steel Schlenk line, evacuated to 10^{-3} mbar, and flame sealed under dynamic vacuum with a hydrogen-oxygen torch.

The sealed ampule was then placed on an elevated rack in the center of a chamber furnace (Carbolite CWF 12/13) and heated to the setpoint (1050 °C) via a programmable PID controller (Eurotherm 3216) at 1 °C min⁻¹. The temperature setpoint was held for 1 h and then the furnace was naturally cooled to below 100 °C, at which point the furnace was opened and the ampule was removed. The sealed ampule was scored using a diamond-bladed saw and carefully opened in a fume hood, typically resulting in a forceful release of gaseous byproducts (likely H_2, HX, and X_2 where X = Cl, Br, or I) and sometimes a flame. Note: the formation of surface and/or bulk white phosphorus is expectable under all conditions explored herein and caution should be exercised in

handling and opening all post-pyrolysis (pressurized) ampules. The final product was collected after washing with copious deionized water and acetone on a fritted glass funnel and drying at 80 °C under air for 24 h.

All final materials are referenced herein according to their nominal composition, "PC_x", or by the name "P/C-1:x-PX$_3$" where x refers to the molar ratio of C:P in the initial reaction mixture and X refers to the halide in the precursor used (X = Cl, Br, or I). For example, when 0.75 mmol of benzene was combined with 1.5 mmol of PBr$_3$, the resulting material was referred to as P/C-1:3-PBr$_3$.

Electrode Materials and Preparation

The following materials were used to prepare the electrochemical cells: LP58 (1.2 M LiPF$_6$ in EC/EMC (3:7) wt% battery grade, Gotion Inc.), fluoroethylene carbonate (FEC, battery grade, Gotion Inc.), lithium metal (chips, 99.9%, MTI Corp.), glass microfiber discs (0.67×257 mm, GF/D grade, catalogue number 1823-257, Whatman), carbon black (Super P, Timcal Ltd.), polyvinylidene fluoride (PVDF, 99.5%, MTI Corp.), N-methyl-2-pyrrolidone (NMP, 99.0%, Sigma-Aldrich), and copper foil (thickness: 9 μm, MTI Corp.). A pure carbon control material, referred to elsewhere as Ben800, was synthesized via the pyrolysis of neat benzene at 800 °C according to a previous report.[136]

P/C electrode slurries were prepared mixing active P/C material (80 wt%) with carbon black (10 wt%) and PVDF (10 wt%) in NMP. After grinding by hand for 15 min, the slurry was cast onto Cu foil using a doctor blade (16.5 μm height) then underwent a three-stage drying process: under air at room temperature for 8 h, under air at 80 °C for a further 8 h, and then under rough vacuum (Welch Chemstar Dry 2071B) at 100 °C for a further 10 h. Individual electrode disks were

cut using a benchtop punch ($\varnothing$ 10 mm), and then stored under inert argon atmosphere in a glovebox (< 0.1 ppm H_2O, < 0.1 ppm O_2) until further use.

Electrochemical Cell Fabrication

Half-cells were assembled under argon (< 0.1 ppm H_2O, < 0.1 ppm O_2) in coin cell format (316 stainless steel, size 2032, Xiamen AOT Electronics Technology Co.). A P/PC_x electrode served as the working electrode, a glass microfiber disk ($\varnothing$ 16 mm) served as the separator, and a lithium metal chip ($\varnothing$ 16 mm) served as the counter electrode; the cell was flooded with 125 µl of LP58 modified with an additional 2 wt% of FEC as the electrolyte, and fitted with a conical spring and spacer (1.0 mm thick) prior to crimping closed.

Materials Characterization

Structural Characterization Powder X-ray diffraction (XRD) measurements were performed using a Bruker D8 ADVANCE diffractometer using Cu K$\alpha_{1,2}$ radiation ($\lambda = 1.54$ Å) in reflection geometry. Samples were prepared for XRD by sonication in acetone for 5 min and then air drying at 80 °C for 24 h.

Raman spectroscopy was performed using a benchtop spectrometer (HR Evolution, Horiba Scientific Ltd.) equipped with a confocal microscope using a 532 nm (2.33 eV) frequency-doubled Nd:YAG laser with an incident power of 45 mW.

Chemical Environments Scanning electron microscopy (SEM) and energy dispersive X-ray (EDX) spectroscopy were measured using a Zeiss Supra 55VP microscope with the field

emission source operated at 10 nA and 10 kV. Samples were prepared for SEM and EDX by pressing the as-collected flakes onto carbon tape on an aluminum sample holder.

^{31}P MAS NMR spectroscopy was performed using a 400 MHz spectrometer (9.4 T, Bruker Corp.) equipped with an Avance III HD console and a 3.2 mm three-channel low-temperature MAS probe. Samples were packed into 3.2 mm zirconia rotors, which were weighed before and after packing. Sample spinning speeds were set to 20 kHz for the reference measurement ($NH_4H_2PO_4$) and 10 kHz for the P/C samples (due to their conductive behavior). Samples were handled and measured in air at room temperature. A simple one-pulse sequence was used with a $\tau_{90} = 4.4$ μs. The number of transients collected was 4 for the reference measurement and 512 for the P/C samples. Recycle delays were chosen to be at least $5 \times T_1$ whenever T_1 was known. In the case of the absence of signal, a maximal T_1 of 5 s was assumed. All experimental parameters (except the spinning speed and number of transients) were kept the same for all the samples, including the reference.

NMR spectral fitting was performed using the dmfit package.[172] The spectrum for $NH_4H_2PO_4$ was fit with a CSA MAS model combined with a Voigt lineshape. The signals corresponding to P_4 in the P/C samples were fitted with Gaussian lineshapes. The baseline was corrected using a linear function and/or a broad Gaussian lineshape. The quantification of P_4 content was assessed by integration of the peak fit minus the baseline, assuming a linear dependency of the peak area to the number of ^{31}P nuclei in the sample using $NH_4H_2PO_4$ as the external standard.

Electrochemical Characterization

Galvanostatic charge/discharge (GCD) cycling was performed in a temperature-controlled incubator (KB 53, Binder GmbH) at 25.0 °C using a battery cycler (CT30001A, Landt

Instruments). Charge and discharge were performed using a constant current (CC) protocol at either 1 or 0.02 A g^{-1} within the voltage range 0.01-2.00 V vs. Li/Li$^+$. Cyclic voltammetry (CV) was performed using a potentiostat (VMP-3e, BioLogic SAS). Cells were cycled at 0.1 mV s^{-1} between either 0.01-2.00 V or 0.25-2.00 V vs. Li/Li$^+$, as indicated.

Theoretical Calculations

All calculations were performed using a density functional theory (DFT) method with the MN15 functional[173] and the def2-QZVPP basis set[174], for both geometry optimization and determination of single point energy. The change in self-consistent field (SCF) energy of a given reaction was determined by:

$$\Delta E^{SCF} = \sum_i E_i^{SCF} - \sum_j E_j^{SCF}$$

where ΔE^{SCF} is the decomposition energy of a given precursor molecule, E^{SCF} is the SCF energy of a given species, i is the index over decomposition reaction products, and j is the index over decomposition reactants. The decomposition energy was typically normalized per P or C atom for intercomparison.

Results

Synthesis

P/C composite materials were synthesized via the direct pyrolysis of benzene together with a phosphorus trihalide precursor in a closed reactor at 800-1050 °C. A striking visual difference between the reaction products occurred, strongly delineated by the identity of the P precursor, as shown in Figure 4.5. In order to elucidate the structural and compositional trends within this series, all further analysis reported herein is focused only on the reaction products obtained after pyrolysis

at the highest temperature explored: 1050 °C. Upon opening materials with a diamond saw blade there is a release of gaseous byproducts (likely a mixture of H_2, HX, and X_2 where X = Cl, Br, or I). Any phosphorus residing on the graphitic carbon material is readily oxidized and is visibly seen be a white/yellowish color: this is most extreme in P/C-1:3-PCl$_3$, which is believed to initially contain the most white phosphorus before exposure to air. Visible red phosphorus is present in P/C-1:x-PBr$_3$ materials (see Figure 4.5), indicative of bulk RP. Finally, the PI$_3$-derived materials contain two distinct environments one in which polyiodide ions are deposited on the quartz ampule resulting in an orange/yellowish color and regions where red phosphorus (or a sub allotrope of phosphorus such as Hittorf's) is visible. Importantly, graphitic flakes collected in PI$_3$ materials most closely resemble pure graphitic carbon synthesized by the same synthetic method with pure benzene as a precursor. All resulting materials after work-up are metallic and lustrous in nature.
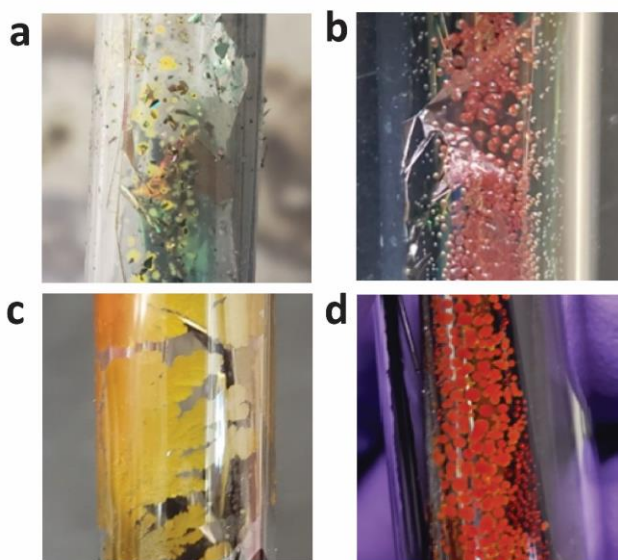
Figure 4.5. Representative photographs of the reaction products (referred to as P/C-1:x-PX$_3$) of the co-pyrolysis of benzene and PX$_3$ (X = Cl, Br, or I) after exposure to air and prior to washing: (a) P/C-1:3-PCl$_3$ showing off-white oxidized P$_4$/PO$_x$ side products, (b) P/C-1:3-PBr$_3$ showing RP as a dominant P product, (c) P/C-1:3-PI$_3$ showing polyiodide impurities, and (d) P/C-1:3-PI$_3$ showing RP as a side product.

Structure

The structure of the directly-synthesized P/C composites was determined by XRD and Raman spectroscopy (Figure 4.6). All of the XRD patterns show a broad reflection centered at 2θ = 23-26° which corresponds to the (002) reflection in graphite. The broadness of this feature (FWHM = 5-10°) indicates the existence of small crystallites and significant long-range disorder in the graphite structure. An additional peak at 2θ = 44-46° represents the (10l) family of planes in graphite. An abrupt structural transition of the (002) peak is observed as a function of increasing nominal phosphorus content (between 1:3 and 1:1) for both -PCl$_3$ and -PBr$_3$ derived materials, from a d-spacing of 3.55-3.77 and 3.56-3.88 Å, respectively (see Table 4.2). A similar but diminished trend is observed for the PI$_3$-derived materials. This is indicative of extremely disrupted graphitic ordering at high P contents, and hence further studies herein were focused on P/C materials of composition 1:3 and 1:5 only. Two additional reflections at 2θ = 15.5° and ~34° are present in P/C-1:x-PBr$_3$ materials (x<5), corresponding to amorphous red phosphorus (a-RP) and consistent with the visual observations described above. It is important to note that the white phosphorus, previously confirmed to exist in P/C-1:x-PCl$_3$ via ^{31}P ssNMR is amorphous and does not contribute to the measured XRD pattern.[134]
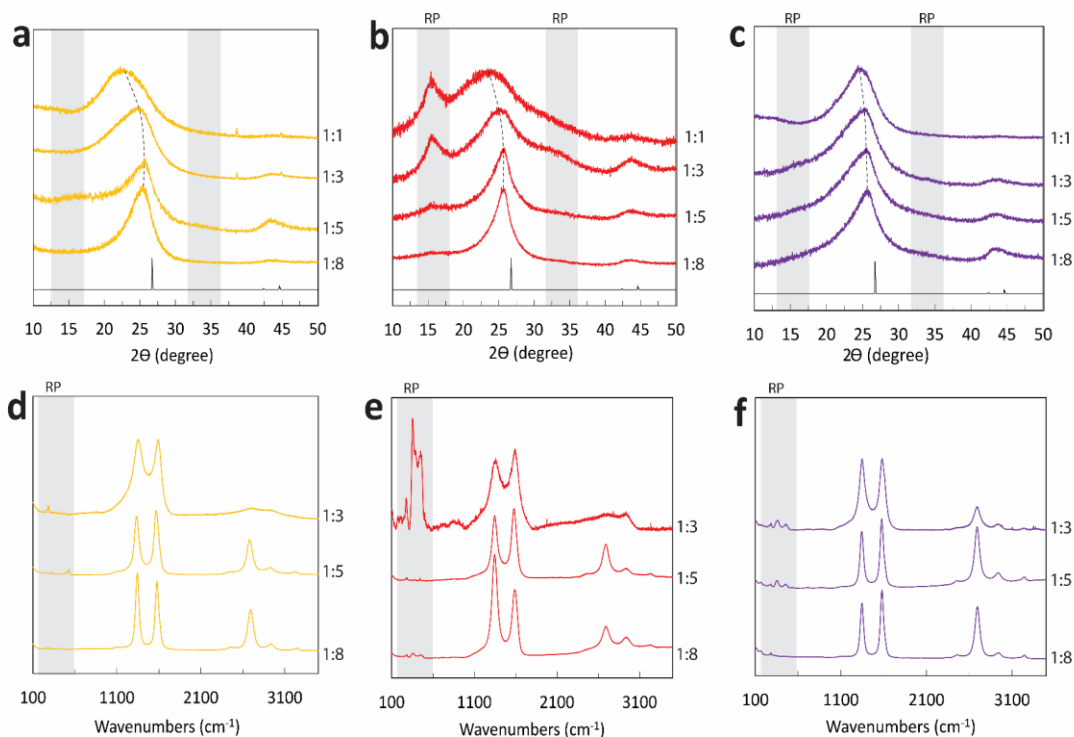
Figure 4.6. XRD patterns and Raman spectra of P/C composite materials synthesized using PCl_3 (yellow), PBr_3 (red), or PI_3 (purple) as the P precursor. The XRD patterns (a-c) for nominal compositions between $1 \leq x \leq 8$ are shown. Grey regions indicate reflections associated with RP. Crystalline graphite (black) is also shown for comparison. Representative Raman spectra (d-f) for nominal compositions between $3 \leq x \leq 8$ are shown, under irradiation at 532 nm.

Table 4.2. Nominal composition and d-spacing of P/C materials.

Nominal Composition	$d_{(002)}$ (Å)		
	P/C-1:x-PCl$_3$	P/C-1:x-PBr$_3$	P/C-1:x-PI$_3$
1:1	3.77	3.88	3.59
1:3	3.55	3.56	3.50
1:5	3.47	3.51	3.47
1:8	3.47	3.47	3.44

Raman spectra of all P/C materials are shown in Figure 4.6. The D and G peaks, representative

of graphitic material, exist in the higher wavenumber range (800-2000 cm^{-1}). The D peak (~1350

cm^{-1}) is present in sp^2 hybridized carbon domains containing defects and arises from the

"breathing" mode of 6 membered carbon rings. The G peak (~1580 cm^{-1}) arises from the concerted motion of C-C bonds in a graphitic lattice, and is always present (with or without defects).[146] Figure 4.7 show the D peak position as a function of nominal phosphorus content. P/C-1:x-PCl$_3$ and -PBr$_3$ materials undergo a D peak position maximum with increasing phosphorus content. Low phosphorus content (x≥5) materials behave as undoped turbostratic graphitic carbon where the D peak is centered at ~1350 cm^{-1}. Moderate phosphorus content (2≤ x ≤4) leads to an upshift in the D peak position to ~1360 cm^{-1} suggesting phosphorus incorporation into the graphitic lattice. At very high phosphorus contents (x≤2) the D peak position decreases back to ~1350 cm^{-1} indicating phase separation of white and red phosphorus allotropes in P/C-1:x-PCl$_3$ and -PBr$_3$ materials. Interestingly, P/C-1:x-PI$_3$ materials do not exhibit a peak maximum at the D peak as a function of increasing P content. P/C-1:x-PI$_3$ materials instead exhibit a narrower FWHM of the D and G peak and a well-defined 2D region compared to -PCl$_3$ and -PBr$_3$ materials (See Table 4.3). It is suspected that the structural ordering of P/C-1:x-PI$_3$ materials is a result of polyiodide species acting as a catalyst during reaction.[175, 176]
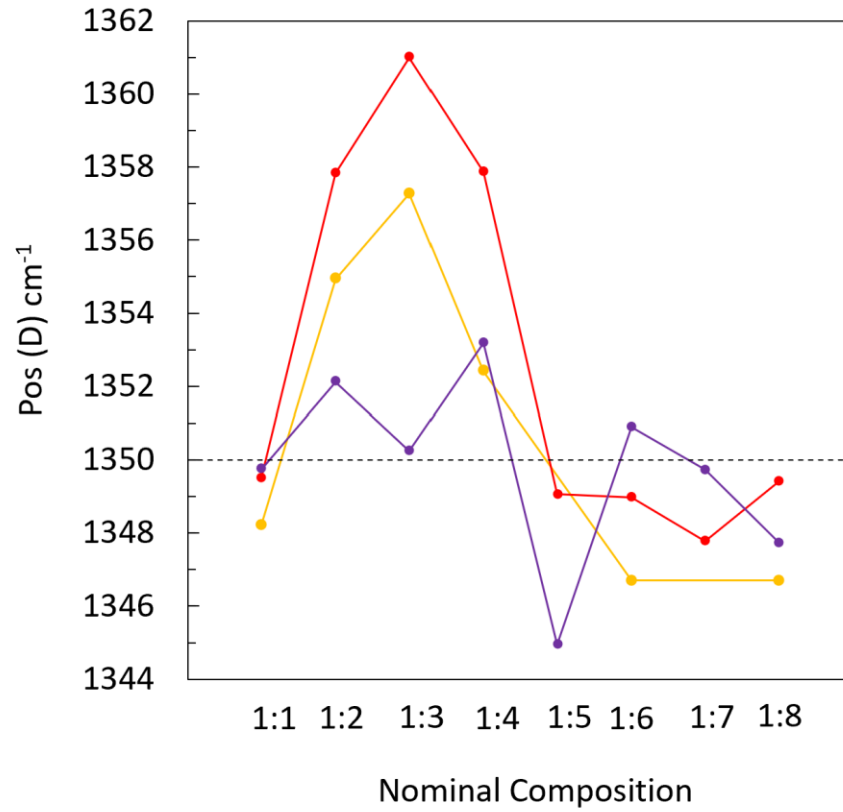
Figure 4.7. D peak position as a function of nominal composition of -PCl$_3$ (yellow trace), -PBr$_3$ (red trace) and -PI$_3$ (purple trace) derived materials. Dashed line at 1350 cm^{-1} shows the standard D peak position for graphite.

Table 4.3. Raman spectroscopic properties of P/C materials.

Precursor	Nominal Composition	D Peak		G Peak		
		D(pos)	FWHM	G(pos)	FWHM	I(D)/I(G)
PCl_3	1:3	1357	98	1587	99	1.02
	1:5	1336	32	1574	62	0.90
	1:8	1344	23	1579	50	1.14
PBr_3	1:3	1361	97	1591	117	0.89
	1:5	1349	43	1582	73	0.87
	1:8	1348	39	1591	68	1.45
PI_3	1:3	1350	49	1584	82	0.94
	1:5	1345	24	1579	49	0.82
	1:8	1348	23	1582	46	0.78

A cluster of peaks, consistent with the intertubular bending and stretching modes of RP, appears in the low frequency range (200-600 cm^{-1}) in both -PBr_3 and -PI_3 materials (Figure 4.6). The RP peaks generally increase in intensity as a function of increasing nominal phosphorus content, but are most clearly observable in the P/C-1:3-PBr_3 material. On average, the intensity of red phosphorus peaks increase as a function of increasing nominal phosphorus content. Select Raman spectra of P/C-1:8-PBr_3 show an absence of red phosphorus vibrational modes, which suggests sample heterogeneity (see Figure 4.8). The Raman spectra of P/C-1:3-PI_3, magnified 5×, also confirms the existence of red phosphorus, however, in much lower quantities compared to P/C-1:3-PBr_3 (Figure 4.9). It is significant that red phosphorus vibrational modes are observable over the resonant enhanced graphitic D and G modes, thereby suggesting that red phosphorus exists largely as a composite material for P/C-1:x-PBr_3. XRD and Raman spectroscopy both reveal that PBr_3 and PI_3 significantly select for the formation of RP in the synthesis products of co-pyrolysis with benzene, as opposed to PCl_3 which does not.
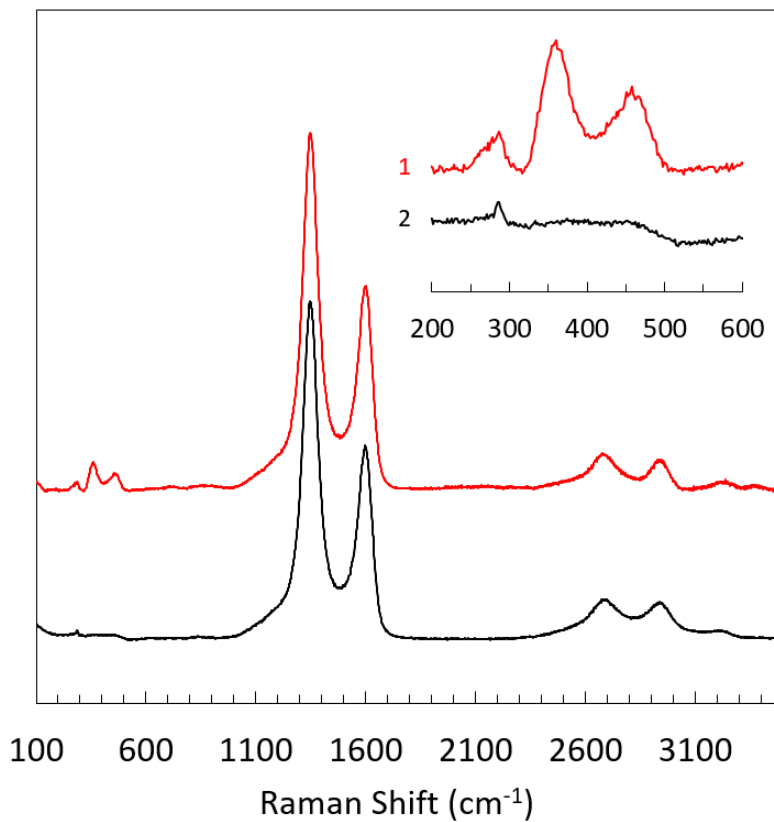
Figure 4.8. Raman spectra collected at two distinct regions of P/C-1:8-PBr$_3$. The inset shows the presence of RP in the low wavenumber region for region 1 (red trace).
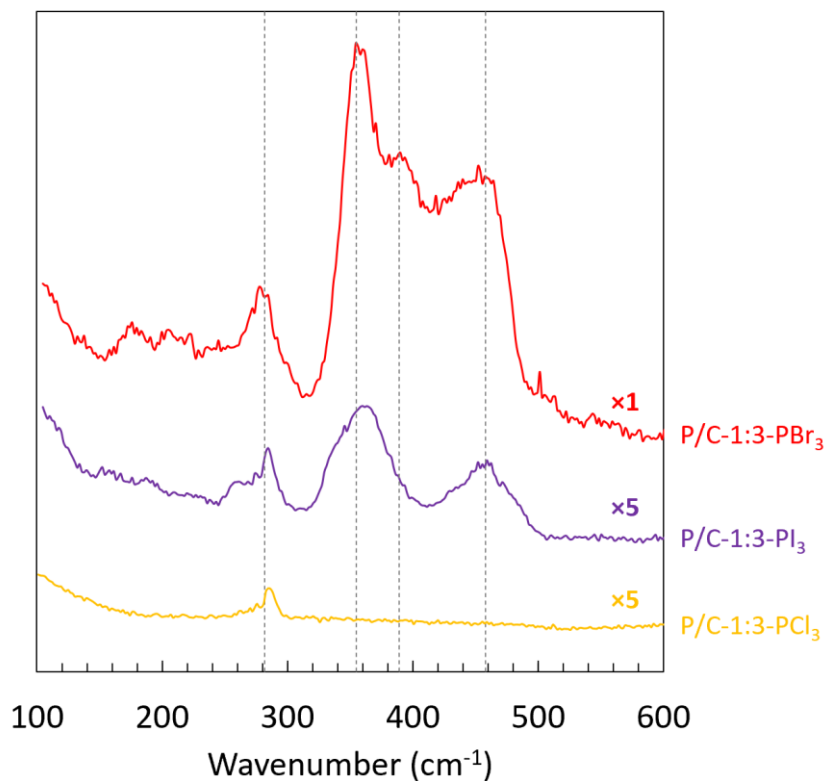
Figure 4.9. Low-frequency Raman spectra of P/C-1:3-PCl$_3$, -PBr$_3$, and -PI$_3$. The dashed lines indicate vibrational modes associated with RP.[177]

Composition

    EDX analysis of P/C-1:x-PCl$_3$, -PBr$_3$ and -PI$_3$ materials is shown in Table 4.4. The total remaining P content after workup greatly depends on the identity of the precursor, and in some cases the nominal composition. The PBr$_3$-derived material of nominal composition x = 3 (P/C-1:3-PBr$_3$) contains the highest P content (~28 at%, ~48 wt%). In specific regions of the graphitic flakes, P/C-1:3-PBr$_3$ materials contain upwards of 45 at% P. This is consistent with the high intensity contributions from bulk RP revealed by XRD and Raman spectroscopy, and the composite nature of this material is further confirmed by SEM (as shown in Figure 4.10). Despite also showing some evidence of bulk RP, the PI$_3$-derived materials contain the lowest amount of phosphorus (~4-5

at%). Residual halide content in PI_3 derived materials is quite high (~2.0 at%) compared to PCl_3 and PBr_3 derived materials. This is likely due to the heavy mass of iodine and trapping of iodide species between graphitic sheets. Evidence and discussion of halide trapping in P/C materials is presented in Appendix D.

Table 4.4. Chemical composition of P/C-1:x-PX$_3$ materials as determined by EDX analysis.

P Precursor	Nominal Composition	P Content (at%)	C Content (at%)	X Content (at%)	O Content (at%)	Si Content (at%)
PCl$_3$	1:3	10.1 ± 4.9	85.4 ± 5.2	0.1 ± 0.0	4.4 ± 4.3	0.1 ± 0.0
	1:5	6.3 ± 2.0	90.1 ± 2.0	0.1 ± 0.0	3.6 ± 2.8	0.0 ± 0.0
PBr$_3$	1:3	28.1 ± 17.5	64.3 ± 17.5	0.5 ± 0.1	6.9 ± 2.5	0.2 ± 0.2
	1:5	6.1 ± 3.7	88.5 ± 3.5	0.2 ± 0.2	5.3 ± 2.0	0.1 ± 0.0
PI$_3$	1:3	4.5 ± 2.0	84.2 ± 3.9	1.6 ± 0.9	9.6 ± 2.6	0.0 ± 0.0
	1:5	4.7 ± 2.7	84.9 ± 5.4	2.3 ± 1.4	7.9 ± 2.1	0.1 ± 0.1
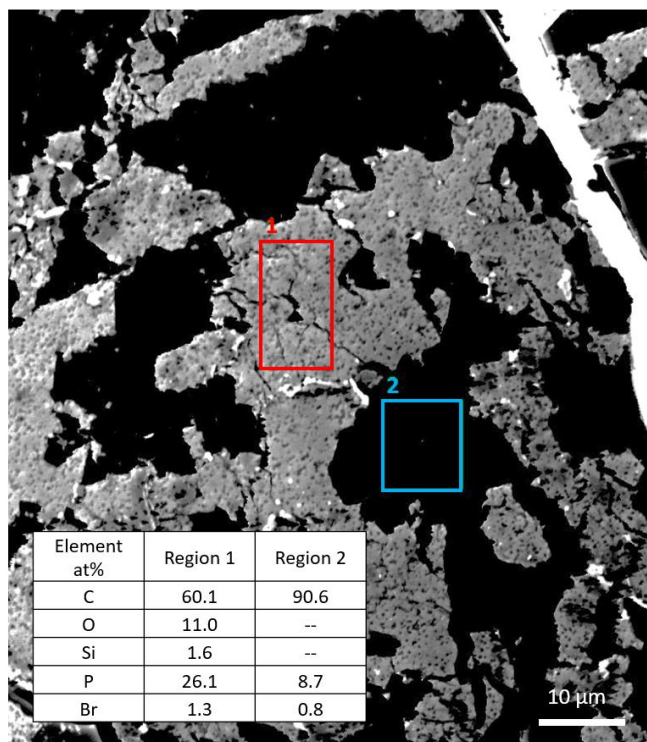
Figure 4.10. SEM/EDX analysis of P/C-1:3-PBr$_3$ synthesized at 1050 °C. Region 1 shows a phosphorus rich region. Region 2 is indicative of a graphitic flake.

Phosphorus Chemical Environment

White phosphorus inclusions within a graphitic scaffold may not be easily detected by XRD owing to their molecular nature; compared to RP, WP is highly likely to exhibit rotational disorder or be amorphous. Likewise, resonance enhancement of the Raman-active modes of graphite when using standard visible irradiation sources can overwhelm any features from WP. Therefore. ^{31}P ssNMR was used to distinguish and quantify WP environments in the P/C composites investigated herein, as shown in Figure 4.11. Experimental conditions were optimized for the analysis of WP and therefore quantification of RP content was not pursued by NMR (a far more difficult endeavor). The presence of a feature at ~-530 ppm is direct evidence of tetrahedral P$_4$ molecules in all PCl$_3$- and PBr$_3$-derived materials. This WP contribution explains the relatively high P content

in P/C-1:x-PCl₃ materials (~6-10 at%, Table 1) which do not show any evidence for RP inclusions. Interestingly, the WP signal in P/C-1:3-PBr₃ is observed at -460 ppm, ~70 ppm downfield from the WP feature seen in the other P/C materials; the cause of this unusual shift remains unknown but could be due to spatial distribution of nearby P atoms.
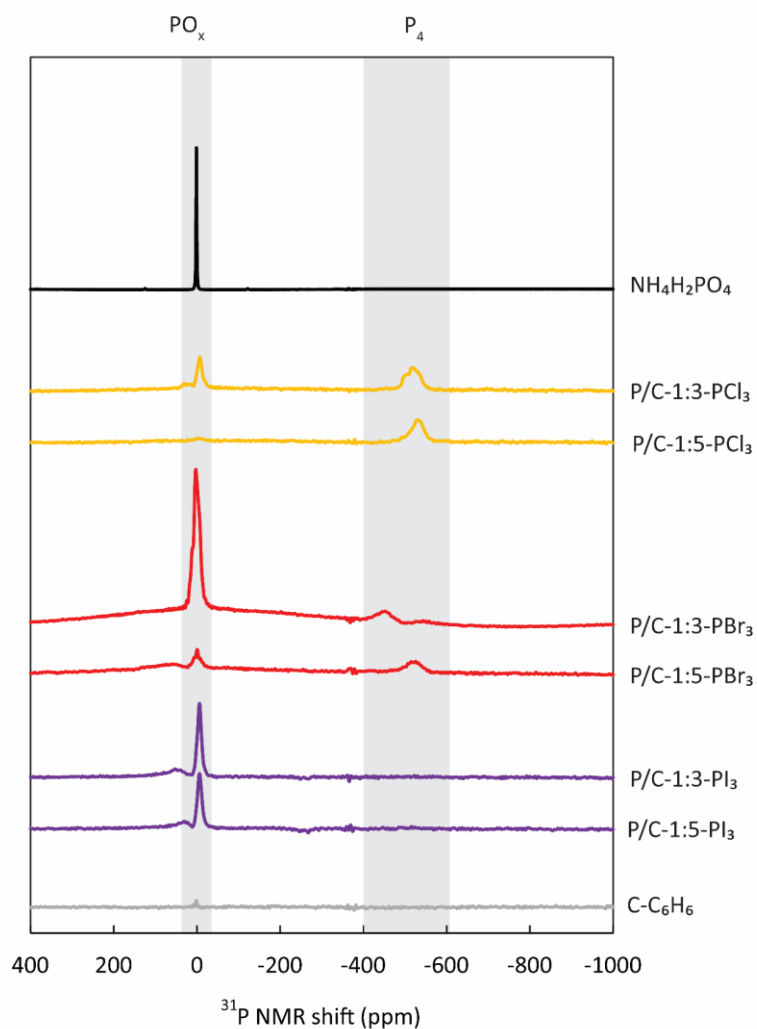
Figure 4.11. ^{31}P NMR spectra of P/C composite materials showing two primary P environments: P$_4$ (WP, between -400- and 600 ppm) and phosphorus (0 ppm). Minor contributions from RP are detectable as a broad feature at ~0 ppm.

<u>Electrochemistry</u>

Two methods were employed to investigate the reversible electrochemical lithiation of the P/C composite materials: CV and GCD cycling. Slow-rate CV profiles of the six materials of highest interest are shown in Figure 4.12. Two broad redox pairs occurring at ~0.3-1.0 and 0-0.1 V are revealed for all materials: in both the first cycle and subsequent cycles. The latter redox couple corresponds to the well-known (de)lithiation of graphitic carbon.[136] The other redox couple centered at ~0.3-0.8 V upon reduction (lithiation), exhibits a large overpotential shifting to ~1.0 V upon oxidation (delithiation). Only in P/C-1:3-PBr$_3$ do additional and well-defined anodic peaks exist (1.04, 1.20, and 1.27 V), representing the stepwise delithiation of phosphorus (Li$_x$P → P where x=1-3). [63, 178] The high content of bulk RP in that composite gives rise to this distinct redox.

To investigate the electrochemical lithiation of solely the P content of each P/C composite (i.e., in the absence of any graphitic contribution), a lower voltage cut-off of 0.25 V was employed. In this range (0.25-2.00 V vs. Li/Li$^+$), only the irreversible formation of SEI and the lithiation/delithiation of the phosphorus network is permitted. Slow-rate CV cycling in this range showed almost identical profiles as observed in the wider voltage window; the lithiable P content could be determined by integrating the second cycle oxidative (delithiation) current (Table 4.5). The total lithitaed phosphorus (14 wt%) in P/C-1:5-PCl$_3$ nearly matches the total measured phosphorus content by EDX (15 wt%). Generally, however, all other materials demonstrate lower total lithiable phosphorus than total measured phosphorus indicating there is inaccessible phosphorus within the active material. This is most noticeable in P/C-1:3-PBr$_3$ which acts the most like a composite. In order to assess error associated with total lithiable phosphorus, a pure graphitic carbon control material was also examined by cyclic voltammetry (0.25-2.00 V vs. Li/Li$^+$, 0.1 mV s^{-1}) to determine the error associated with this method of lithiable P content (see Figure 4.13). The

carbon control material is pyrolozed benzene at 800 ℃ and is representative of the turbostratic

nature and structural ordering of P/C mateirals.
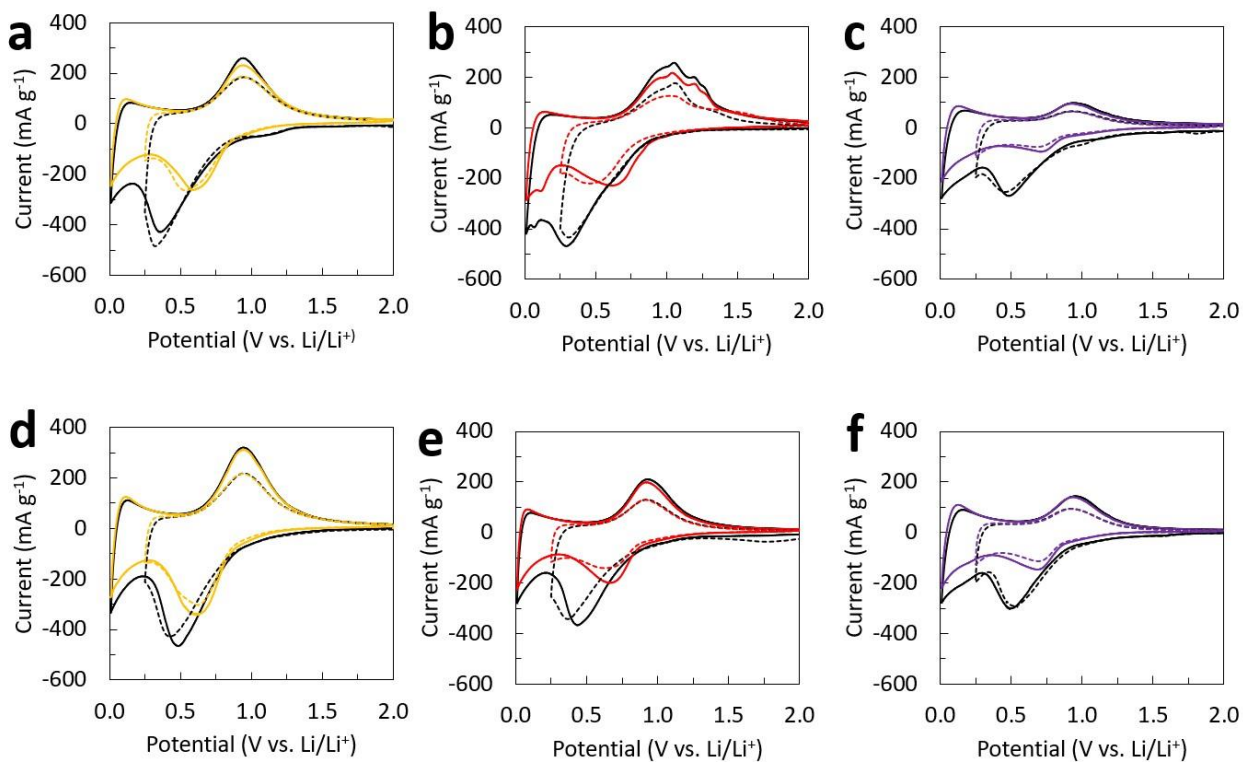
Figure 4.12. Electrochemical lithiation/delithiation of P/C composite materials synthesized using PCl$_3$ (yellow), PBr$_3$ (red), or PI$_3$ (purple) as the P precursor. CV profiles for nominal compositions (a-c) x = 3 and (d-f) x = 5 are shown at 0.1 mV s^{-1}; the first cycles are shown in black and the second cycles are shown in color. Two voltage ranges are shown: 0.01-2.00 V (solid lines) and 0.25-2.00 V (dashed lines) vs. Li/Li$^+$.
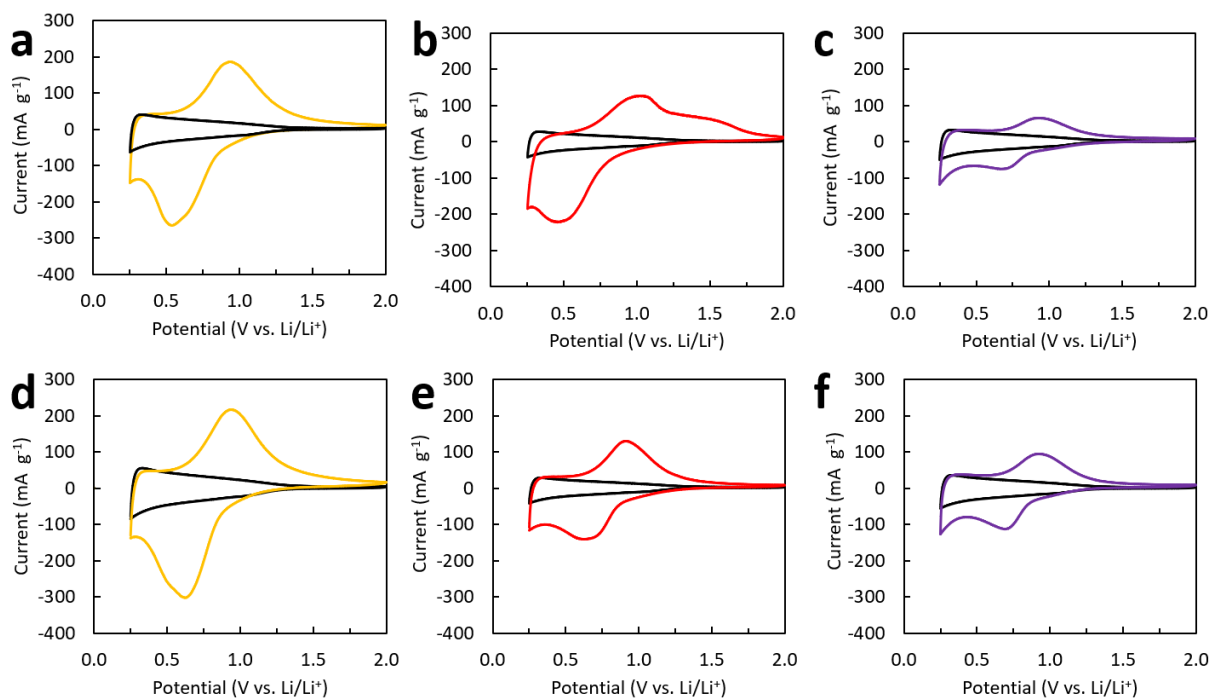
Figure 4.13. Second cycle voltage cutoff (0.25-2.0 V) cyclic voltammetry. (a-c) PC_3 and (d-f) PC_5 materials synthesized with -PCl_3 (yellow), -PBr_3 (red), and -PI_3 (purple) overlayed with pyrolyzed benzene (800 °C) control (black).

Voltage profiles (Figure 4.14 and 4.15) are shown at 1 A g^{-1} and 0.02 A g^{-1} to examine chemistry at different rates. Voltage plateaus remain nearly identicle suggesting these materials are not rate limited. In both sets of voltage plateus there is obvious capacity loss after the first cycle observed for all PC_x materials suggesting irreversible lithiation of phosphorus and formation of SEI. Figure 4.16 shows GCD cycling at 1 A g^{-1} for all P/C materials as compared to the carbon control. Interestingly, the first cycle capacities of P/C materials are fairly representative of the predicted capacities with the expection of -PBr_3 derived materials (Appendix F). For example, the calculated theoertical capacity of P/C-1:x-PCl_3 is ~634 mAh g^{-1} and the measured first cycle capcity is 604 mAh g^{-1}. With regard to performance, P/C-1:5-PCl_3 demonstrates the highest

capacity and stability over 1000 cycles at ~ 300 mAh g^{-1}. The optimal performance of P/C-1:5-PCl$_3$ can likely be attributed to stabilized P$_4$ molecules between graphitic sheets.
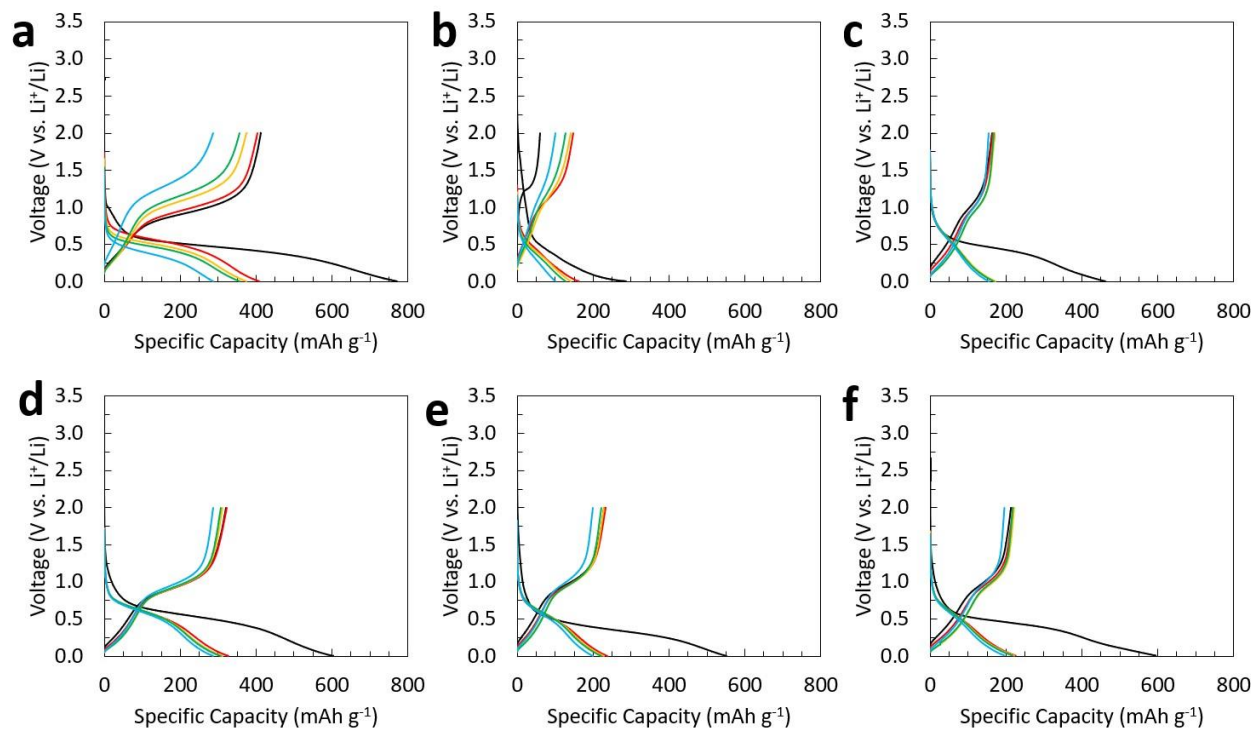
Figure 4.14. Voltage profiles from 0.01-2.00 V vs. Li/Li$^+$ cycled at 1 A g^{-1}. (a) P/C-1:3-PCl$_3$, (b) P/C-1:3-PBr$_3$, (c) P/C-1:3-PI$_3$, (d) P/C-1:5-PCl$_3$, P/C-1:5-PBr$_3$, and (f) P/C-1:5-PI$_3$ at cycles 1 (black), 5 (red), 50 (yellow), 100 (green), and 500 (blue).
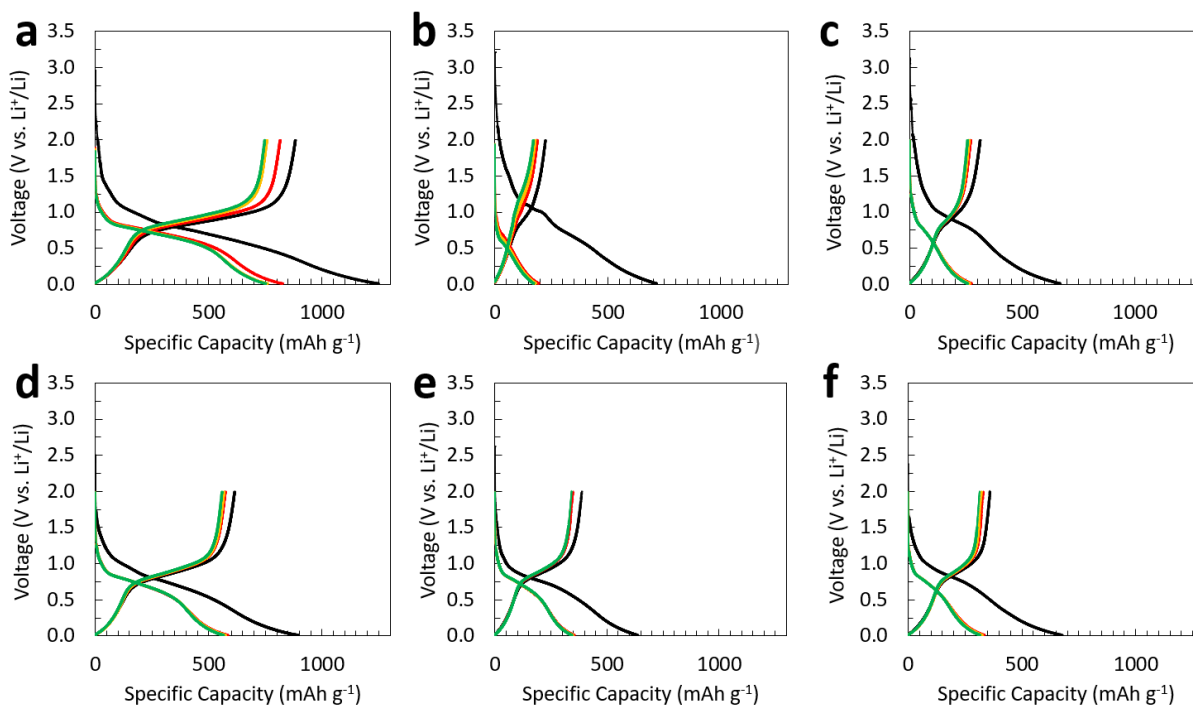
Figure 4.15. Voltage profiles from 0.01-2.00 V vs. Li/Li$^+$ cycled at 0.02 A g^{-1}. (a) P/C-1:3-PCl$_3$, (b) P/C-1:3-PBr$_3$, (c) P/C-1:3-PI$_3$, (d) P/C-1:5-PCl$_3$, P/C-1:5-PBr$_3$, and (f) P/C-1:5-PI$_3$ at cycles 1 (black), 5 (red), 10 (yellow), and 20 (green).
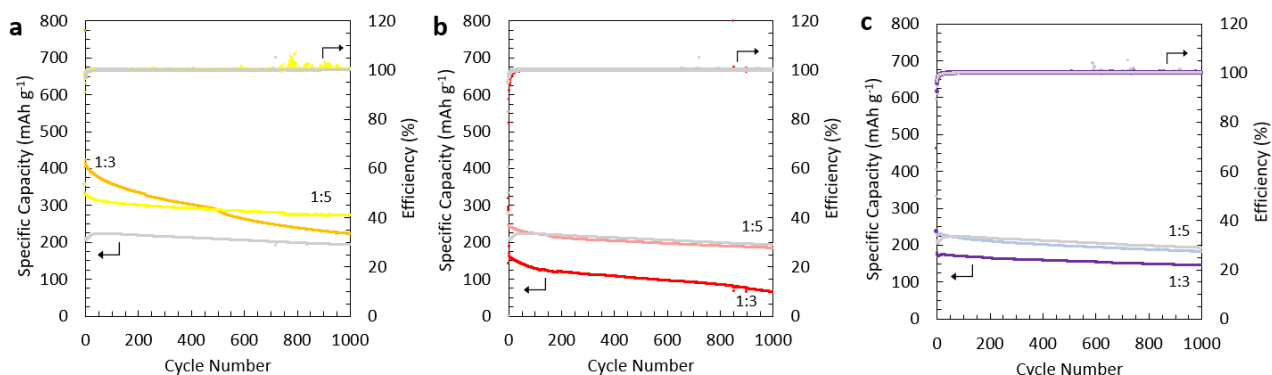
Figure 4.16. Cycling stability and coulombic efficiency from 0.01-2.00 V vs Li/Li$^+$ cycled at 1 A g^{-1} for P/C materials derived from (a) PCl$_3$, (b), PBr$_3$, and (c) PI$_3$. All graphs show 1:3 and 1:5 nominal compositions compared to a carbon control (C$_6$H$_6$ pyrolyzed at 800 °C) (gray trace).

Quantification of Phosphorus Allotropes

An aim of this work was to discern relative contributions of red and white phosphorus allotropes within P/C materials, especially in the P/C-1:x-PBr$_3$ materials which is known to contain both RP and WP evidenced by XRD, Raman spectroscopy, and ^{31}P ssNMR. To tabulate the total relative allotropic contributions in each sample we rely on information from ^{31}P ssNMR to infer how much WP is present. The total integrated area from the P$_4$ signal was normalized to the total amount of phosphorus determined by EDX for P/C-1:5-PCl$_3$, a model material believed to contain solely P$_4$ environments (see prior study [134]). The total RP content can then be determined by taking the difference in total measured P content determined by EDX and the WP content determined by ^{31}P ssNMR. Table 4.5 shows tabulated WP and RP (wt%) content for all P/C materials.

Table 4.5. Weight distribution of phosphorus allotropes in P/C composite materials, as determined by a combination of ^{31}P NMR spectroscopy and EDX analysis (in at%).

P Precursor	Nominal Composition (1:x)	Nominal P Content[a] (wt%)	Actual P Content[b] (wt%)	P_4 Content[c] (wt%)	Red P Content[d] (wt%)	Lithiable P Content[e] (wt%)
PCl$_3$	1:3	46%	22%	15%	7%	9%
	1:5	34%	15%	15%	0%	10%
PBr$_3$	1:3	46%	48%	17%	31%	8%
	1:5	34%	14%	8%	6%	6%
PI$_3$	1:3	46%	9%	-	9%	3%
	1:5	34%	9%	-	9%	4%

[a]Determined by the ratio of benzene to PX$_3$ in the original reaction
[b]Determined by EDX spectroscopy
[c]Determined by ^{31}P NMR spectroscopy
[d]Determined by the difference between EDX[b] and NMR[c] P contents
[e]Determined by CV along the anodic (oxidation) branch between 0.25-2.00 V vs. Li/Li+ at 0.1 mV s^{-1}

Figure 4.17 visually shows total measured phosphorus, lithiable phosphorus within error, and the relative quantities of red and white phosphorus for P/C materials. The samples with almost exclusively WP (P/C-1:x-PCl$_3$) show a strong correlation between the WP content and the (reversible) lithiable P content; this indicates that, whether or not the P content is returned to the WP phase after first delithiation, the stabilized WP in these P/C composites is highly robust toward lithiation/delithiation cycling. Materials containing WP contain 8-17 at% P$_4$ which is likely related to a structural packing limit of WP in graphitic carbon (see Appendix H).
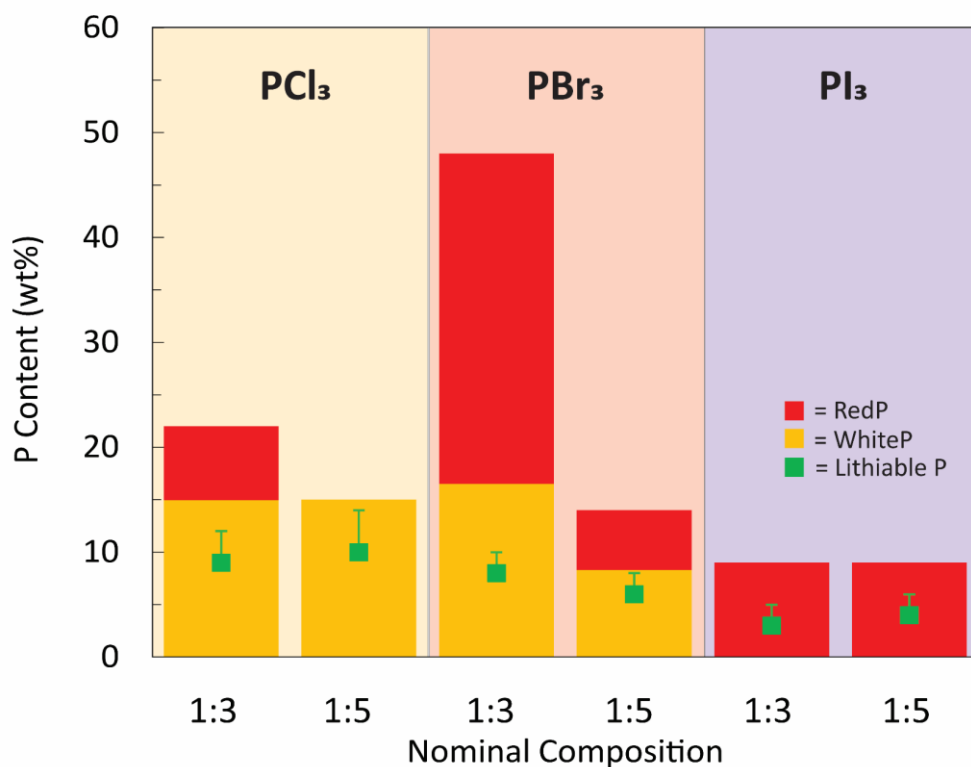
Figure 4.17. Total measured phosphorus and relative quantities of red and white phosphorus shown for P/C-1:3 and P/C-1:5 materials synthesized with PCl$_3$, PBr$_3$, or PI$_3$ as the precursor. Total lithiable phosphorus (determined electrochemically between 0.25-2.00 V vs Li/Li$^+$) is also shown.

Formation of Phosphorus Allotropes

In order to explain the systematically varied phase-segregated components of the novel P/C composite materials, thermochemical calculations were performed to quantify the difference in energy of decomposition of each precursor. The relevant decomposition energies, normalized per P or C atom generated by complete dissociation of the molecule, are shown in table 4.6. The precursors decrease in thermochemical stability from PCl_3 to PI_3, as expected. Importantly, all three PX_3 precursors explored herein exhibit a lower stability than benzene, though PCl_3 is the most similar (8.2 compared to 9.1 eV atom^{-1} for PCl_3 and C_6H_6, respectively). Thus, in the reaction mixture initially containing PCl_3 and benzene, the P–Cl bonds likely break and begin to form a P–P bonded network at the same time as the benzene is undergoing pyrolysis to form graphitic nanocrystals; rapidly formed WP become trapped and well-dispersed within the growing graphitic carbon scaffold. This is in contrast to the case for the less stable PBr_3 and PI_3 mixtures (6.9 and 5.6 eV atom^{-1}, respectively) where the P–X bonds break and begin to form a P–P bonded network significantly prior to benzene decomposition. In these systems, the originally formed WP likely polymerizes to form large RP networks prior to the formation of the first graphitic nanocrystals. Hence, the RP becomes covered in graphitic carbon but the two phases remain well segregated; some WP remains in the case of PBr_3-derived composites owing to the shorter time spent above the decomposition threshold. Finally, in the case of the PI_3 derived composites, extreme phase separation results in poor contact between the RP and the graphitic scaffold, allowing the RP phase to be completely washed away during workup, thus explaining the relatively low total P content and complete absence of WP. Figure 4.18 shows a schematic of model materials for the three different halide precursors and their resulting allotropes according to precursor decomposition energies.

Table 4.6. Estimated decomposition energies of phosphorus and carbon precursors. Calculations carried out using MN15 functional and Def2-QZPP basis.

P Precursor	Reaction	ΔE^{SCF} (eV)	Energy (eV/P)
PF_3	$2PF_3 \rightarrow 2P + 3F_2$	30.8	15.4
PCl_3	$2PCl_3 \rightarrow 2P + 3Cl_2$	16.3	8.2
PBr_3	$2PBr_3 \rightarrow 2P + 3Br_2$	13.9	6.9
PI_3	$2PI_3 \rightarrow 2P + 3I_2$	11.2	5.6
C Precursor	Reaction	ΔE^{SCF} (eV)	Energy (eV/C)
C_6H_6	$C_6H_6 \rightarrow C_6 + 3H_2$	54.5	9.1
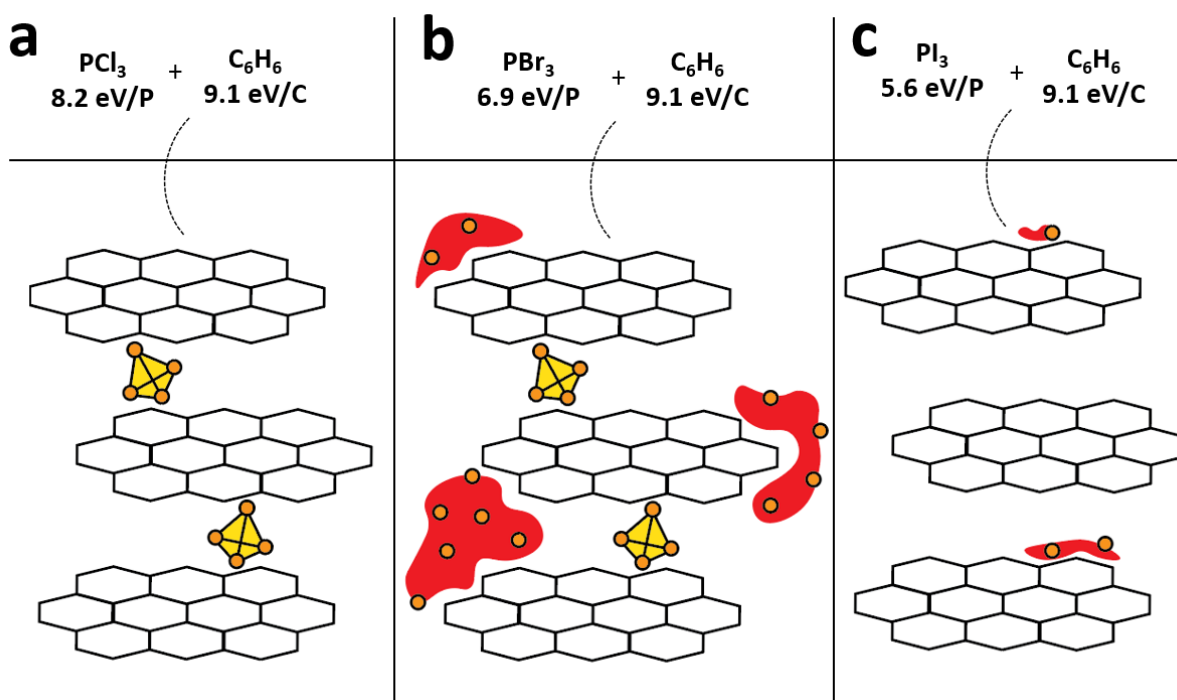
Figure 4.18. Predicted material models based on chemical precursor decomposition energies for (a) P/C-1:x-PCl_3, (b) P/C-1:x-PBr_3, and (c) P/C-1:x-PI_3.

Conclusions and Future Work

Careful control of phosphorus allotropes (e.g., red or white) formed within P/C materials is demonstrated by altering the tri-halide precursor used in a direct and single-step synthesis. The

initial goal of altering the tri-halide precursor was to optimize for the substitutional doping, an extension of past work that methodologically investigated synthesis temperature and nominal composition.[134] We instead discover the formation of WP and RP allotropes in which the type and relative quantity of each allotropes depends on the tri-halide precursor selected. Materials are explored as lithium-ion electrode materials in attempts to leverage the high capacity of phosphorus (e.g., theoretical capacity 2596 mAh g^{-1}, expected for pure phosphorus) and the structural stabilization offered by the graphitic scaffold.

PBr$_3$ derived materials were initially thought to be a strong candidate as a LIB anode material owing to its composite like nature of red phosphorus and graphitic scaffolding whereby red phosphorus would greatly enhance overall capacity and graphitic carbon would act as a scaffold mitigating volume expansion of phosphorus during (de)lithiation. Surprisingly this material did not exhibit enhanced capacity relative to pure graphitic carbon despite containing the most phosphorus. Rather, PCl$_3$-derived materials demonstrate enhanced capacity compared to graphitic carbon, and more so, remarkable stability at 1 A g^{-1} for over 1000 cycles at~300 mAh g^{-1}. The structural positioning and dispersion of P$_4$ molecules within P/C-1:5-PCl$_3$ lends to superior electrochemical performance relative to other P/C composite materials. A question remains as to whether P$_4$ molecules maintain intact during (de)lithiation, suggesting full reversible lithiation of the P$_4$ molecule itself, or undergo a structural polymerization within the graphitic sheets. Future work will focus on determining the stability and reversibility of P$_4$ domains after the first cycle. Broad impacts are expected of stabilized P$_4$ include storage of P$_4$ as well as controlled release of P$_4$ for other applications.

CHAPTER FIVE

SYNTHESIS AND CHARACTERIZATION OF ALUMINUM-DOPED GRAPHITIC CARBON

Introduction

Substitutional heteroatom doping and co-doping of carbon-based (and other group IV) solids by elements such as boron, nitrogen, phosphorous, and sulfur has been extensively explored to tune the structural and chemical/electrochemical properties for a variety of applications.[112, 133, 179] Notable examples of this strategy are boron incorporation into graphite for nuclear shielding applications,[180] modification of the electronic structure of fullerenes and nanotubes by B (p-type) and N (n-type) doping,[181] and nitrogen incorporation into templated carbon to enhance CO_2 uptake for direct air capture applications[182, 183] and methane absorption.[184] In general, this body of research is wide-ranging in its findings, and recently many long-prevailing trends in the results are coming under higher scrutiny.[185, 186] Phosphorous incorporation is relatively common as a strategy to enhance the electron donating character of sp^2-hybridized carbon surfaces [134, 187-190]; on the other hand, few experimental reports exist that describe the successful substitutional incorporation of aluminum into a graphitic lattice.[191] Hence, there is fundamental importance in this endeavor given the complementarity of the electron withdrawing/donating properties of Al and P with respect to carbon.

Aluminum and carbon are typically explored together as metal matrix composite (MMC) materials,[192, 193] or in other composite applications (e.g., aluminium nanoparticles on porous carbon supports).[194, 195] Graphite and aluminium metal face wettability issues when forming composites; the binary phase, aluminum carbide (Al_4C_3) is readily formed at high temperatures.[196-

[198] Few existing studies directly target substitutional doping. A representative such study, perhaps the first to explicitly report substitutional incorporation of aluminum into an sp^2-hybridized carbon system, is focused solely on graphene and not a free-standing, bulk material.[191] On the contrary, numerous computational studies investigate aluminum doping in carbon materials (e.g., CNTs,[199, 200] graphite,[201, 202] and graphene[203-205]) and many predict applications towards hydrogen storage,[201, 205] gas sensing,[200, 204, 206-208] and catalysis[209, 210] that would require free-standing, bulk AlC_x materials. The aluminum-carbon binary phase diagram reported by Gokcen and Oden[211] (Figure 5.1) seems to remain the state of knowledge today as to the equilibrium aluminum solubility in crystalline graphite. The precise solubility limit is unknown but is often reported as negligible (which we assign as <0.01 at%). We hypothesized that further investigation via bottom-up synthesis techniques could lead to a variety of ordered or disordered and stable or metastable bulk graphitic materials with higher aluminum content than 0.01 at%, similar to those prepared for other heteroatoms (e.g., boron[212, 213] and phosphorus[134]).

In this work, we explore a variety of direct (bottom-up from molecular precursors) synthesis approaches targeting high aluminum-content graphitic carbon materials where aluminum is exclusively substituted within the graphitic lattice. Under optimal conditions and after appropriate post-synthesis processing, samples containing up to ≤ 0.5 at% Al could be synthesized and were subsequently characterized. These materials are generally highly disordered, but evidence is presented that the aluminum is likely bound in trigonal planar environments within the graphitic lattice.
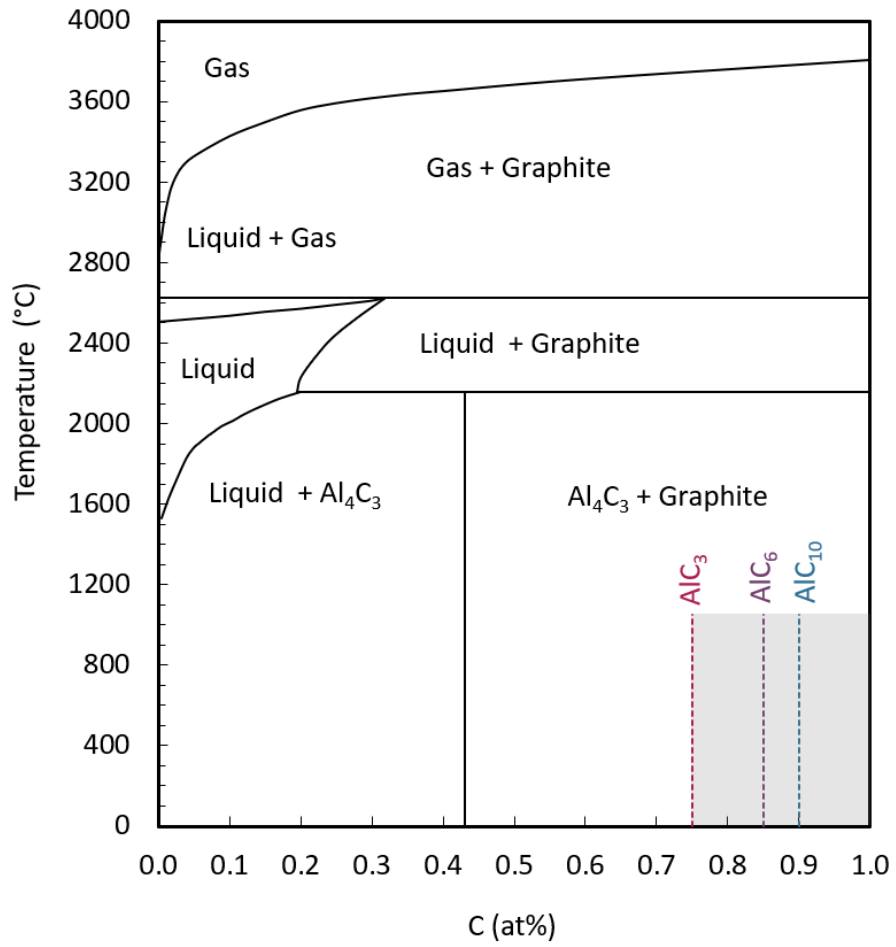
Figure 5.1. Aluminum-Carbon phase diagram adapted from Gokcen and Oden.[211]

Primary Aims

Incorporation of aluminum into free-standing bulk carbon materials is not well reported at this time. This work aims to substitutionally incorporate aluminum in turbostratic graphitic carbon. Fundamental interest lays within understanding how p-type doping alters structural and chemical properties of graphitic carbon. The same bottom-up co-pyrolysis method used for phosphorus doping (chapter 4) is adopted in this work for a best side-by-side comparison of p-type and n-type doping. We find it challenging to achieve substitutional doping without the formation of an undesired byproduct, mullite. Large efforts of this work focus on the prevention and elimination of the aluminosilicate byproduct through systematic control of synthetic parameters and post work-up procedures. Resulting materials are characterized by X-ray absorption spectroscopy (XAS) to identify the presence of Al-C bonding environments. It is our hope that this work lends insight into synthesis routes and conditions that allow for metastable aluminum-doped graphitic carbon.

Synthesis and Characterization of Aluminum-Doped Graphitic Carbon

Materials Synthesis

Aluminum-doped graphitic materials, hereinafter referred to as AlC_x, were synthesized via a direct synthesis route analogous to previous strategies employed for boron [212] and phosphorus [134]. In each case, a quartz ampule (15 cm length, 1.0 cm inner diameter) was charged with either a mixture of benzene (anhydrous 99.8%, Sigma Aldrich) and aluminum trichloride ($AlCl_3$, anhydrous, Acros Organics), a solution of trimethylaluminum in toluene (TMA/toluene, 2.0 M, Sigma Aldrich), or neat trimethylaluminum (TMA, 97.0%, Sigma Aldrich) inside a glovebox under inert argon conditions (≤ 0.5 ppm O_2, ≤ 0.5 ppm H_2O). In certain cases, the ampule was

pretreated by carbon passivation (neat benzene pyrolysis inside a double-necked ampule) or the precursors were wrapped in a molybdenum foil ($\geq$99.9%, 25 μm thick, Sigma) pouch prior to sealing for the final reaction; such efforts were not found to be more successful than direct pyrolysis within a standard quartz ampule. The total amount of precursors sealed was determined by setting the final pressure of the reaction at 20 bar, based on the inner volume of the ampule (~12 mL) and the assumption that pyrolysis would be stoichiometric and all products would be diatomic gases (H_2, HCl, or Cl_2). A Swagelok ultra-torr adaptor was placed over the open end of the ampule; the capped ampule was removed from the glovebox and partially submerged in liquid nitrogen to solidify the precursor solution. The ampule was connected to a Schlenk line, evacuated to 10^{-3} mbar, and then flame sealed under vacuum.

Sealed ampules were placed on an elevated platform at the center of a chamber furnace (Carbolite CWF 12/13) and heated to a final set temperature between 800-1100 °C via a programmable PID controller (Eurotherm 3216). The temperature set point was held for 1 h and then cooled to below 100 °C at which point the furnace was opened and the sealed ampules were removed. Sealed ampules were carefully opened using a diamond blade saw in a fume hood where gaseous byproducts (e.g., HCl) could be safely released. The solid product was collected and rinsed with deionized water and acetone. All samples were air dried at 80 °C for 24 h before further analysis. To dissolve aluminosilicate impurities, some samples were subjected to HF washing as follows: 20% aqueous HF for 48 h, followed by copious DI rinse and collection of material.

<u>Materials Characterization</u>

<u>Structural Characterization</u> XRD measurements were performed using a Bruker D8 Advanced diffractometer using Cu K$\alpha_{1,2}$ radiation (λ = 1.54 Å) in reflection geometry. Samples

were prepared for XRD by ultrasonication in acetone for 5 minutes and then dried at 80 °C for 24 h. Raman spectroscopy was performed using a Horiba LabRAM HR Evolution spectrometer equipped with a confocal microscope and a frequency-doubled Nd:YAG laser (532 nm) with an incident power of 10 mW.

Composition and Morphology SEM and EDX spectroscopy were measured using a Physical Electronics PHI 710 microscope with a field emission source operated at 1 and 10 kV, respectively. Samples were prepared for SEM and EDX by pressing the as-collected material into indium foil which was then secured to an aluminum mount.

X-Ray Absorption Spectroscopy Aluminum and carbon chemical environments were analyzed by XAS, measured at the Spherical Grating Monochromator (SGM) beamline at the Canadian Light Source (CLS). An XAS spectrum is generated by tuning incident photon energy; incident photons are absorbed by electrons occupying the core-shell (K-edge for a 1s orbital) which are then promoted to an unoccupied state above the Fermi level. High energy electrons then fill the core-hole emitting a detectable X-ray at discrete energy. This is reflected in a spectrum by an "edge feature" which is the transition to lowest unoccupied states and corresponds to unique bonding environments and coordination.[214]

As-synthesized flakes were mounted on carbon tape and measured under ultra-high vacuum (10^{-9} mbar). Total fluorescence yield (TFY) was measured for each sample by averaging over four silicon drift detectors (SDDs). Several standard materials were mounted for comparison to AlC_x: aluminum foil (0.25 mm thick, 99.999%, Sigma-Aldrich), aluminum carbide (Al_4C_3, 98%, Goodfellow Corp.), mullite ($3Al_2O_3 \cdot 2SiO_2$, 98%, Alfa Aesar), montmorillonite (K10, Clay Mineral Society), and aluminum phosphate ($AlPO_4$, 99.99%, Sigma Aldrich).

Results

Synthesis

Several synthetic approaches were explored in an effort to achieve phase-pure samples of aluminum-substituted graphitic carbon. The temperature range of interest in this work, informed by previous work in the direct synthesis of boron-[212] and phosphorus-doped [134] graphitic materials, was 800-1100 °C. Hence, while the graphitic ordering of such products was expected to be modest (especially in the stacking direction), the range of heteroatom content was expected to be as high as possible, the major target of this work. Closed-reactor synthesis in this temperature range typically requires the use of quartz ampules when refractory metal ampules are not available (such as in this laboratory). Hence, all experiments described herein involve the selection of precursors followed by charging into a quartz ampule under inert argon atmosphere, and subsequent heating to a set temperature between 800-1100 °C.

At all temperatures explored in this work, an undesired byproduct, the aluminosilicate mineral known as mullite ($3Al_2O_3 \cdot 2SiO_2$), was formed during synthesis. This byproduct is attributable to a reaction between the quartz ampule and the Al-containing precursor (e.g., $AlCl_3$ or TMA). This byproduct could be easily removed by dissolution in aqueous HF. Figure 5.2 shows mullite present in AlC_x before HF and mullite-free AlC_x post EDX.

Numerous attempts were made to prevent the formation of mullite altogether, including passivation of the quartz ampule with pre-synthesis carbon deposition, the use of a molybdenum packet to isolate the precursors from the quartz, and simply the exploration of dilute Al-doping content to prevent leaching; nevertheless, none of these strategies were successful in preventing

the formation of mullite (see appendix I). Therefore, the remainder of this study focuses on the

post-HF treatment of either $AlCl_3$-derived AlC_x or TMA-derived AlC_x.
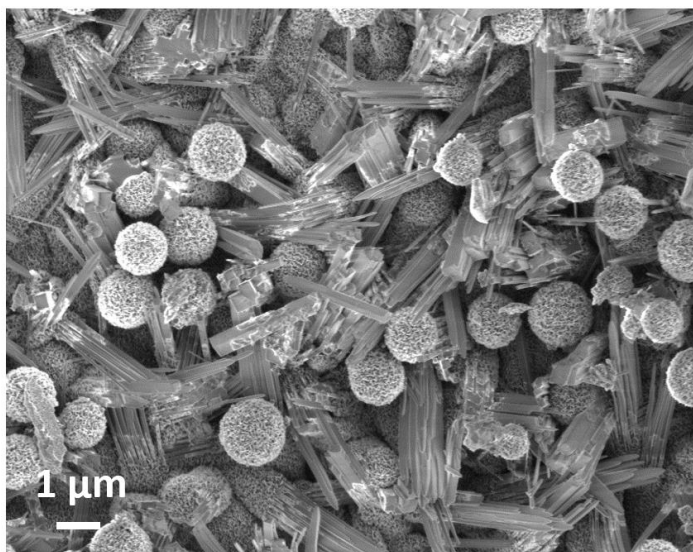
Figure 5.2. Needle-like crystals exist in pre-HF washed AlC_x materials. The morphology and relative composition of rod-like crystal match mullite and are in good agreement with literature.[215][216]

Structure

The crystalline structure of directly synthesized AlC_x was investigated by powder XRD, as

shown in Figure 5.3. All of the XRD patterns for the pre- and post-HF washed AlC_x materials

show a broad reflection centered at $2\theta = 23\text{-}26°$, corresponding to the (002) reflection in graphite.

The broadness of this feature indicates the existence of small crystallites and significant long-range

disorder in the stacking structure (turbostratic ordering). Additional well-defined peaks in the pre-

HF treated samples are indicative of mullite.[215] Under otherwise identical conditions, the mullite

reflections increase in intensity with increasing Al:C ratio (decreasing x) and with increasing

temperature. Mullite formation is likely attributable to side reactions between the aluminum

precursor and the quartz ampule, sequestering a portion of the available aluminum from

incorporation within the graphitic lattice. The mullite reflections completely disappear following HF treatment, indicating that HF dissolution is a viable route to obtain mullite-free AlC_x.
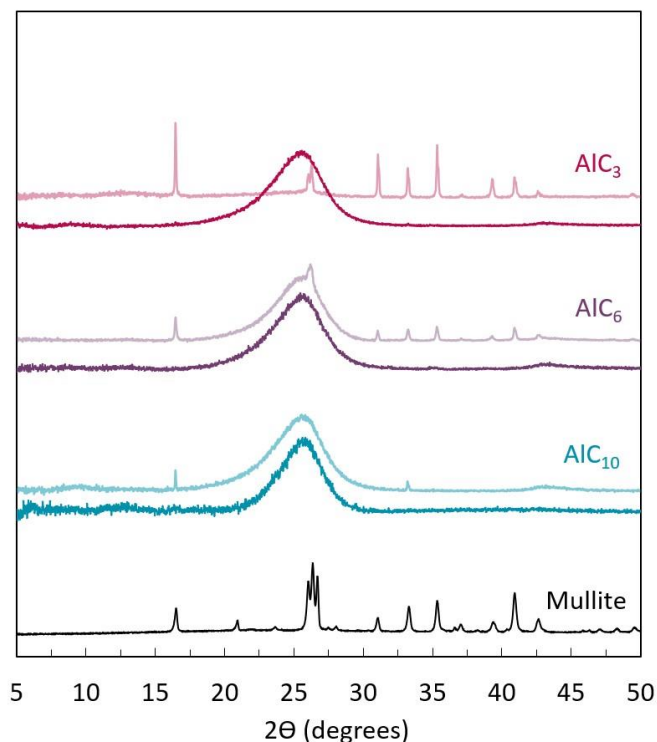
Figure 5.3. XRD patterns of pre- (light trace) and post-HF treated (dark trace) $AlCl_3$-derived AlC_x (of nominal composition x = 3, 6, 10) compared to a crystalline mullite standard.

The in-plane structure of as-synthesized AlC_x was further investigated by Raman spectroscopy (Figure 5.4.). Spatial scanning across the surfaces of the $AlCl_3$-derived AlC_x materials revealed two distinct structural environments: more-ordered and more-disordered graphitic carbon, independent of the nominal composition. In regions where the AlC_x is more ordered, the full-width at half-maximum (FWHM) of the D and G peaks are narrow and the 2D region is defined by four well-resolved peaks. In more disordered regions, the D and G peaks are wider, the 2D region is a broad, modulated hump, and the I(D):I(G) ratio is > 1. These spectral

features are quantitatively tabulated in Table 5.1. The more ordered regions may be a result of carbon pyrolysis in the presence of aluminum as a catalyst. The interlayer spacing as determined by XRD is narrower in all AlC_x materials (e.g., 3.48-3.50 Å at 1100 °C) than in pure carbon materials derived under equivalent conditions (e.g., 3.51-3.54 Å for benzene derived carbon synthesized at 800-1100 °C) (Figure 5.5.). Lower aluminum content (e.g., AlC_{10}) correlates with narrower interlayer spacing; hence, the least amount of aluminum in the initial reaction leads to the strongest catalytic effect, likely owing to the formation of mullite in higher Al content reaction mixtures.
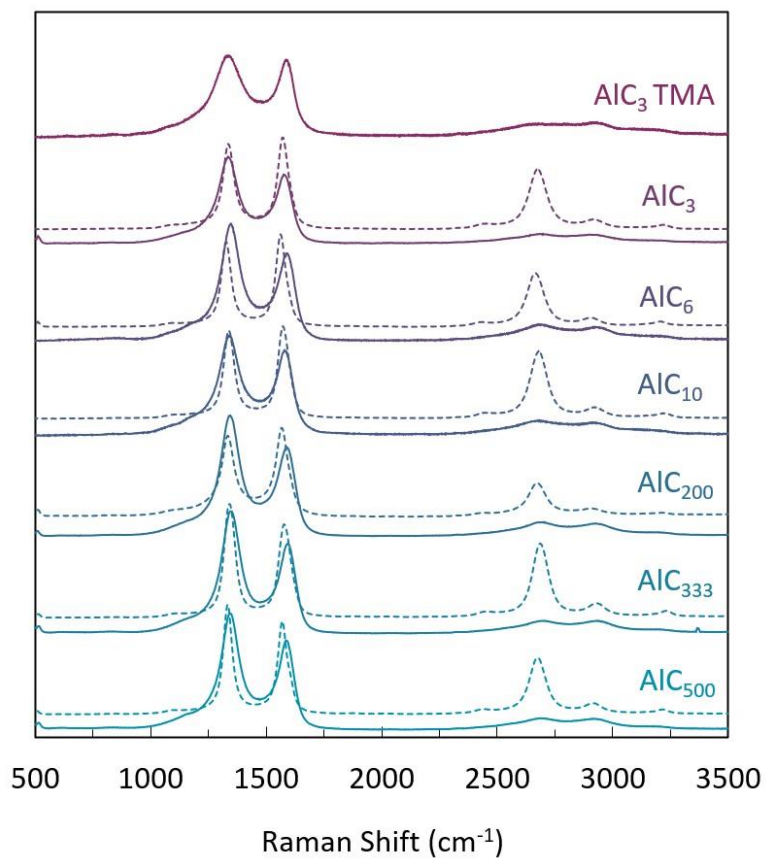
Figure 5.4. Raman spectra of post-HF treated AlCl₃- and TMA-derived AlC$_x$ materials under irradiation at 532 nm, showing two distinct types of regions in each sample: higher and lower ordered nanocrystalline graphite.

Table 5.1. Raman spectral features of AlCl$_3$- and TMA-derived AlC$_x$ samples post-HF wash.

Material	Pos(D) (cm^{-1})	FWHM(D) (cm^{-1})	Pos(G) (cm^{-1})	FWHM(G) (cm^{-1})	I(D)	I(G)	I(D)/I(G)
Ordered							
AlC$_{200}$	1333	22	1571	47	19562	16286	1.20
AlC$_{333}$	1342	25	1580	52	18952	15391	1.23
AlC$_{500}$	1334	38	1567	60	6934	7974	0.87
AlC$_{10}$	1339	27	1575	53	12582	13541	0.93
AlC$_6$	1327	24	1563	47	10446	11416	0.92
AlC$_3$	1337	32	1573	58	10935	12003	0.92
AlC$_3$-TMA	--	--	--	--	--	--	--
Disordered							
AlC$_{200}$	1344	52	1584	71	10075	7780	1.30
AlC$_{333}$	1348	52	1590	73	9962	7284	1.37
AlC$_{500}$	1343	53	1585	79	12513	9237	1.35
AlC$_{10}$	1342	66	1579	86	13367	11619	1.16
AlC$_6$	1345	58	1584	85	8390	6514	1.28
AlC$_3$	1335	57	1575	74	6830	5474	1.25
AlC$_3$ TMA	1338	91	1584	84	3517	3180	1.11
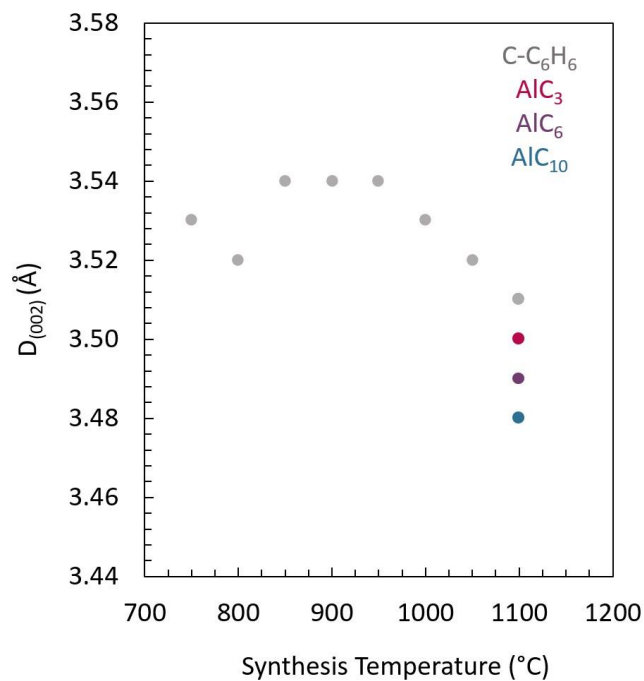
Figure 5.5. d-spacing for AlC$_x$-AlCl$_3$ and C-C$_6$H$_6$ materials

Composition and Morphology

The elemental composition of directly synthesized (post-HF treated) AlC_x was investigated herein by EDX spectroscopy (Figure 5.6). Materials derived from $AlCl_3$ were determined to have Al contents of 0.1-0.5 at% Al, generally increasing with the nominal composition (e.g., the initial concentration of Al in the reaction mixture). On the other hand, materials derived from TMA had almost negligible Al content. These results indicate that there is a larger dependence of the eventual Al content on the identity of the precursor than on the nominal composition of the reaction.

Small traces of chlorine (<1.2 at%) are found to exist within post-HF washed AlC_x; this residual Cl content scales directly with nominal Cl content provided by the $AlCl_3$ precursor. EDX mapping confirms that Cl is not preferentially located within the Al-rich regions (Figure 5.7). Rather, the Cl is likely trapped between graphitic sheets, as an intercalant, or covalently bonded to the graphitic network. We frequently observe this via the direct synthesis of turbostratic graphitic materials using halide containing precursors (Appendix D).[134, 137] No regions of stoichiometric composition consistent with mullite are found to exist within post-HF washed AlC_x materials.
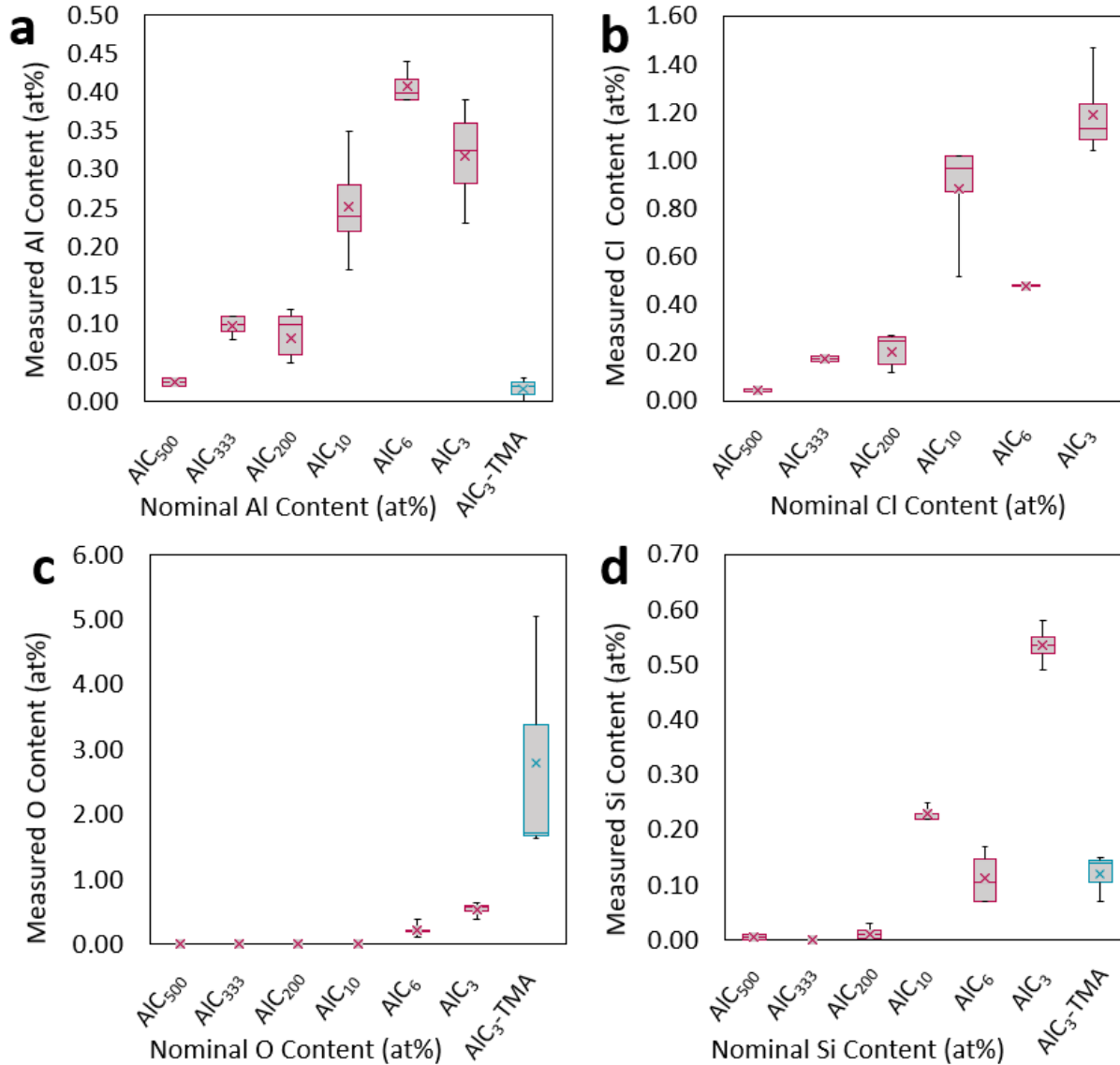
Figure 5.6. a) Aluminum, b) chlorine, c) oxygen and d) silicon content of post-HF treated $AlCl_3$- and TMA- derived AlC_x materials as determined by EDX spectroscopy. $AlCl_3$ (1100 °C) and TMA (800 °C) derived materials are shown in magenta and blue, respectively.
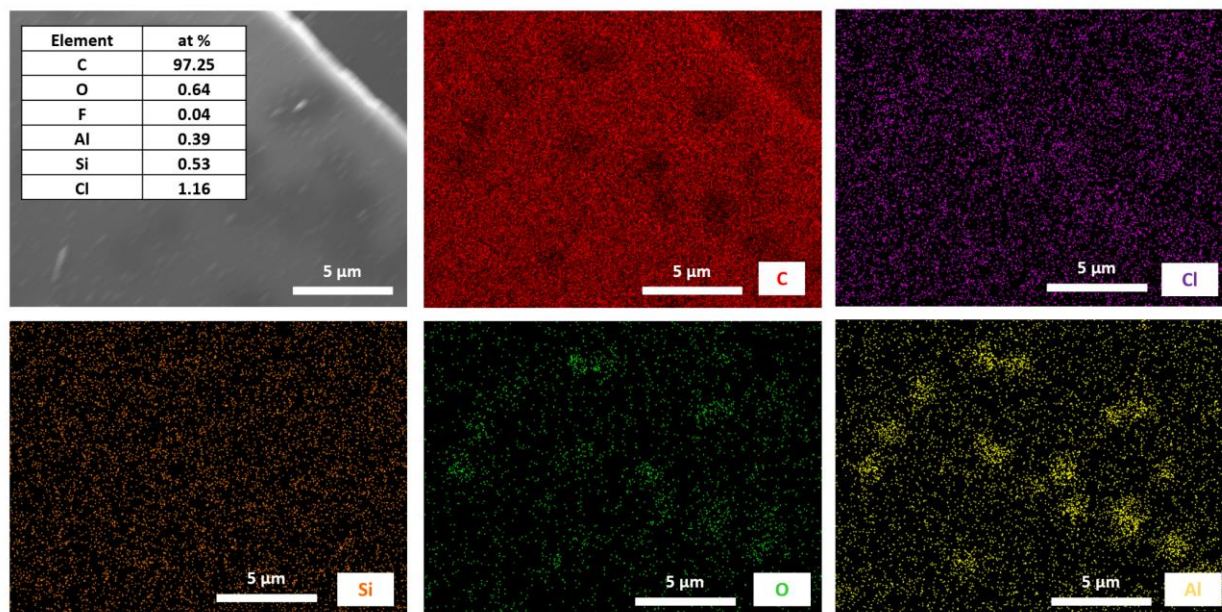
Figure 5.7. EDX mapping of AlC$_3$-AlCl$_3$ synthesized at 1100 °C

Aluminum Bonding Environments

The chemical environment of aluminum within the highest Al content materials was further investigated by XAS. The XAS spectra at the Al K-edge of both pre- and post-HF treated AlCl$_3$-derived AlC$_x$ (of nominal composition x = 3, 6, and 10) are shown in Figure 5.8. The pre-HF treated samples, included herein for control purposes (since they are known to contain predominately mullite-type Al), all exhibit an edge and two post-edge features at 1567.4, 1568.7, and 1572.7 eV, respectively, that are consistent with mullite. [217, 218] After HF treatment, a prominent edge feature at 1566.8 eV and post-edge feature at 1571.7 eV (referred to as E* and E^, respectively) arise in all AlC$_x$ materials with >0.2 at% actual Al content (AlC$_{10}$, AlC$_6$, and AlC$_3$). A slight third feature is evident at 1569.0 eV in AlC$_6$. These primary new environments, E* and E^, are not consistent with tetrahedral (Td) AlO$_4$ or octahedral (Oh) AlO$_6$ environments found in mullite, K10, and AlPO$_4$, nor are they consistent with Td AlC$_4$ environments in Al$_4$C$_3$. The novel

environments are rather lower in energy, suggesting a lower aluminum coordination environments,[219] such as trigonal planar or pyramidal. In general, both E* and E^ increase in intensity at higher synthesis temperatures (Figure 5.8b).
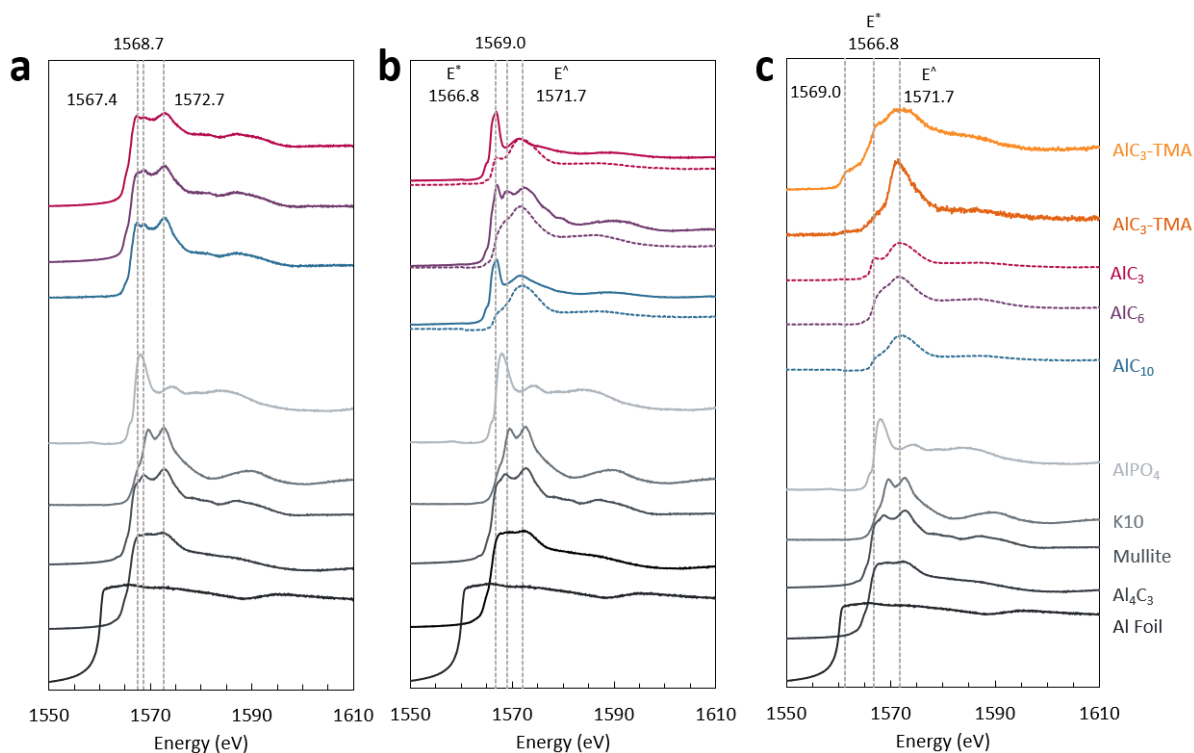
Figure 5.8. XAS spectra near the Al K-edge of (a) pre- and (b) post-HF treated $AlCl_3$-derived AlC_x (where x = 3, 6, and 10) AlC_x materials synthesized at 1100 °C (solid line) are compared to 800 °C (dashed line).(c) XAS Al K-edge spectra of halide- and TMA-derived AlC_x (where x = 3, 6, and 10) synthesized at 800 °C (dark orange) and 1100 °C (light orange). Standards include $AlPO_4$, K10, mullite, Al_4C_3 and Al foil.

The TMA-derived AlC_x plays an important role in this study owing to the inherent presence of Al-C bonds derived from TMA itself, some of which would likely remain intact in the AlC_x product. Indeed, the XAS spectrum of the neat TMA-derived materials pyrolyzed at 800 °C does in fact exhibit the same E* and E^ features present in the AlC_3-derived AlC_x materials (Figure 5.8c), albeit in lower overall concentration of Al. Interestingly, the TMA-derived samples also

contain an Al environment at 1561.3 eV that may be attributed to Al-Al bonding.[220] This would be consistent with TMA decomposition mechanisms where TMA decomposes to monomethyl aluminum (MMA) and bulk Al metal phase segregation occurs.[221, 222] While we are unable to assign an unambiguous Al bonding environment to E* and E^, the existence of these features in AlC$_x$ from both precursors after HF treatment is likely indicative of Al-C bonding in both materials.

Conclusions and Future Work

Two aluminum-bearing precursors and a wide range of synthetic conditions were explored in an effort to synthesize carbon-rich graphitic materials incorporating Al within the sp^2-hybridized lattice via a single-step, direct synthesis approach. The use of a quartz ampule as the closed reaction vessel led to the formation of mullite as an impurity in all reactions studied; this impurity could be effectively removed by post-synthetic dissolution in aqueous HF. The resulting materials were thoroughly characterized, showing that a small content of Al was likely incorporated within the lattice. The presence of Al precursors in the reaction mixture gave rise to a catalytic graphitization resulting in interlayer spacings closer to that in crystalline graphite. Using AlCl$_3$ as the aluminum precursor, up to ~0.5 at% was evidenced across a wide range of initial conditions, indicating that factors such as the temperature and vessel wall chemistry played a larger role than the composition of the initial reaction. Analysis of the XAS spectra obtained for all AlC$_x$ materials with appreciable Al content showed that a pair of new features, referred to as E* and E^, are a unique signature of such materials and are consistent with the presence of trigonal planar AlC$_3$-type environments. Further studies are warranted to examine these features in detail and determine their origin. One desired technique in the future is FTIR to detect the presence of Al-C bonding.[191] Lastly, AlC$_x$

materials were not examined electrochemically but remains an important aspect of future work to

fully elucidate effects of p-type doping on graphitic carbon and to draw further conclusions about

the differences between phosphorus (chapter 4) and aluminum incorporation.

CHAPTER SIX

STABILIZED SILICON ANODES VIA PHOSPHORUS DOPING

Introduction

Chemically Doped Silicon

Proposed strategies to stabilize silicon anodes upon (de)lithiation include nanosizing[71, 73, 223] employing unique morphologies (e.g., Si needles[72, 224]) as well as embedding the silicon phase within a buffering matrix (e.g., Si-C composites)[65, 225] In all cases, however, the reactivity of pure silicon with carbonate-based electrolytes commonly used in LIBs remains an important safety issue. Many attempts have been made to tailor the electrolyte for increased stability during cycling (e.g., solid-state electrolytes).[226-228] An alternative strategy towards stabilizing the silicon electrode interface is chemical doping by p-block elements such as boron[66, 229, 230], nitrogen[231], phosphorus[65, 113, 232-235], and sulfur[236] or by metals such as magnesium, aluminum, calcium, and zinc.[76, 77] Presently, it remains unclear whether elemental doping is the primary cause of any electrochemical or thermal stabilization effects. Herein we attempt to determine the role of substitutional doping on the materials and electrochemical properties of silicon.

Elements with high equilibrium solubility in silicon are arsenic (up to ~3.6 at%), phosphorus (up to ~3.0 at%), and boron (up to ~1.2 at%).[237] Phosphorus and boron are well-known dopants of silicon in the semiconductor industry owing to their electron donating and withdrawing (n- and p-type doping) character, respectively, and both significantly increase its electrical conductivity.[238, 239] Arsenic is not a likely candidate for technological applications; hence, to achieve the widest range of substitutional doping possible, phosphorus is the most suitable

candidate for determining the role of substitutional doping on the materials and electrochemical properties of silicon.

Many past investigations of phosphorus-doped silicon electrodes have focused on doping by imprecise ball-milling techniques[65, 240] or by as-deposited films[232]. Use of composite structures combined with heteroatom doping have been used to combat many of the issues associated with silicon during electrochemical cycling which include volume expansion, pulverization of the anode, and loss of electrical contact.[65, 233, 234] For example, ball-milling of phosphorus-doped silicon and graphite resulting in a composite material with low charge transfer resistance and long cyclability and stability was explored.[65] Similarly, the ball-milling of silicon, black phosphorus, and MWCNTs shows high reversible capacity (>2000 mAh g^{-1}) and reduced volume expansion during cycling.[240] Synergistic effects of heteroatom doping and the composite-like material make it hard to decouple the effects due exclusively to chemical doping.

Domi et al., investigated the role of phosphorus doping in pure silicon electrodes prepared via gas-deposition.[232] Thick-film electrodes were prepared in the absence of binder to fully understand the effects of phosphorus alone. Findings from this work show that trace amounts of phosphorus (124 ppm) significantly enhance electrochemical performance compared to pure silicon electrodes. Our work is modeled after Domi's systematic approach in determining the role of phosphorus doping on electrochemical stability. We utilize a facile synthesis method via solid-state diffusion making our work industrially scalable. The work presented in Chapter 6 attempts to investigate the sole effect of phosphorus doping without use of Si-P/C composites towards the stabilization of silicon anodes.

Silicon-Phosphorus Binary Phase Diagram

The silicon-phosphorus binary phase diagram was constructed in the late 1950's by Giessen and Vogel through microstructural and thermal analysis of silicon/phosphorus melts and is shown in Figure 6.1.[241] Two primary phases are observed in this phase diagram: the SiP compound and the solid solution of P in Si. Solubility of P in Si occurs at the eutectic temperature 1131 ± 2 °C.[115, 241] The maximum reported solubility limit of P in Si is reported to be ~3.0 at%, however, this value has been extensively challenging to identify amongst several groups due to the presence of oxygen and other impurities. Solubility limits of P in Si have been determined several ways; one of the most reliable studies, performed by E. Kooi, examined the diffusion of phosphorus into silicon and a silicon dioxide film using neutron activation analysis.[242] Utilizing a two-zone furnace, the phosphorus source, P_2O_5, and silicon source resided in low (200-300 °C) and hot (920-1310 °C) temperature zones. The maximum solubility of phosphorus in silicon was reported when SiP was found to form between the SiO_2 film and silicon substrate. These results match those of Mackintosh et al. which were measured using resistivity measurements.[243, 244]
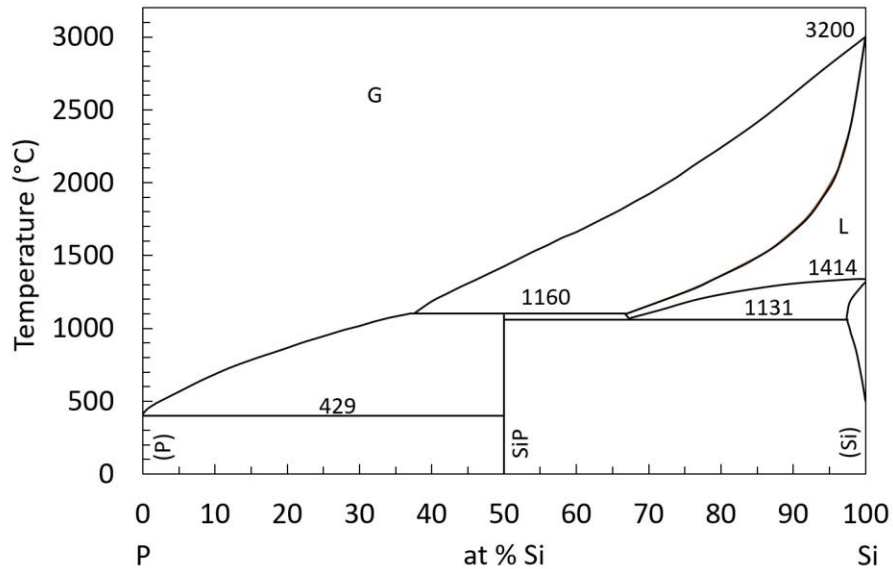
Figure 6.1. Silicon-Phosphorus binary phase diagram adapted by reference [115].

Solid-State Diffusion

Prior to accelerating voltage technology and the subsequent advent of ion implantation technology in 1954, solid-state diffusion reigned as the primary doping method and importantly today still remains an important pillar.[97] Solid-state diffusion is the movement of atoms in a solid whereby a concentration gradient between chemical specials exists and the use of temperature can be employed to accelerate the rate of diffusion. It is traditionally assumed that phosphorus diffusion in silicon obeys a vacancy-mediated mechanism[120], however, conflating studies suggest interstitial-mediated mechanism to dominate.[118, 121] The aforementioned mechanisms are detailed in Chapter 2. In this work we rely on solid-state diffusion of phosphorus into silicon powder at low to medium temperatures (800-1200 °C).

Figure 6.2a shows diffusivity of phosphorus at three different phosphorus concentrations (0.1, 1.0 and 10 at%) as a function of temperature. The diffusion depth of phosphorus into silicon at specific temperatures and times can be calculated using equation 6.1 to ensure homogenous doping

and is shown in Figure 6.2b. Work presented herein largely targets phosphorus concentrations 10^{19} and 10^{20} respectively, 0.1 and 1.0 at% at 1131 °C. Temperature selection (1131 °C) is based upon the silicon-phosphorus eutectic temperature. Expected diffusion depths for the above conditions are ~97 and 234 nm.

$$(6.1) \qquad x = \sqrt{D \cdot t}$$
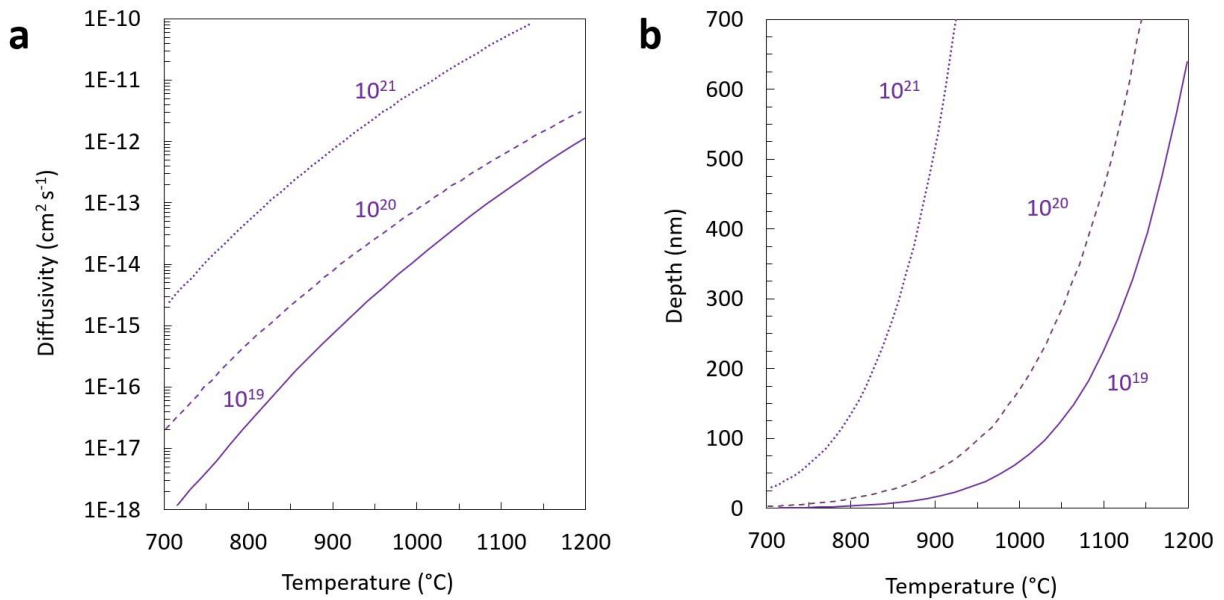
Figure 6.2. a) Diffusivity coefficients (D) of silicon adapted from reference [119] and b) diffusion depth versus phosphorus concentration as a function of temperature. Diffusion depth (x) is tabulated based on equation 6.1 where t = 3600 seconds.

Determining Successful Phosphorus Doping in the Silicon
Lattice

Successful substitutional doping is best determined by XRD where a shift of reflection to larger or smaller 2θ respectively corresponds to the contraction or expansion of the lattice. Typically, changes in lattice parameter can be determined by differences in ionic radii between the dopant and host material. Phosphorus-doped silicon leads to a contraction of the lattice on the order

of 0.0001 nm per 0.5 at% P as reported by Olensinski and others.[115, 245, 246] This contraction is linearly observed until ~3.0 at% solubility is achieved at which point SiP phase forms. Figure 6.3 shows the silicon lattice parameter as a function of phosphorus concentration.
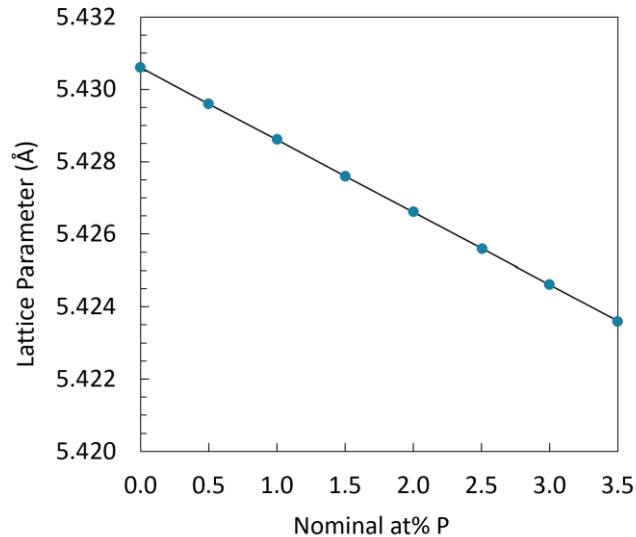
Figure 6.3. Silicon lattice parameter as a function of nominal phosphorus.[115]

Primary Aims

The primary goal of this work is to assess the role of phosphorus doping on the materials and electrochemical properties of silicon. This work first examines phosphorus as a dopant to establish a baseline understanding of doping in a silicon system and later explores alternative dopants including aluminum, boron, magnesium and zinc (Appendix L) in hopes of establishing selection rules based on dopant size, electronegativity and valence. A top-down solid-state synthesis method is adopted whereby solid precursors (silicon and phosphorus powders) are heated to their eutectic temperature to achieve the maximum solubility of phosphorus in silicon. The first goal of this work is to confirm successful doping in the silicon lattice; this is best accomplished by examining shifts of the Si(111) reflection by XRD. Phosphorus is selected as the primary dopant

of investigation owing to its large solubility in silicon at 1131 °C (~3.0 at%) and therefore detectable shift of the Si(111) reflection as a function of dopant concentration. A wide range of synthetic parameters including nominal composition, synthesis temperature (°C), dwell time (h) and ramp rate (°C min^{-1}) are explored to achieve homogenously and heterogeneously P-doped silicon nanoparticles. Homogenous and heterogenous doping models are guided by calculated diffusion depths based on synthetic parameters and are further supported by electrochemical characterization. Importantly, this work aims to decouple the effects of phosphorus doping and particle size on electrochemical behavior of silicon anodes.

Synthesis and Characterization of Phosphorus-Doped Silicon

Preparation of Solid-Solutions (SiP$_x$)

The solid precursors, silicon powder and stabilized red phosphorus powder (8.07270, Sigma Aldrich), were mixed together by mortar and pestle under Ar atmosphere inside a glove box (< 0.5 ppm H$_2$O/O$_2$). Three silicon powders were explored in this work as the silicon precursor: 100 nm Si NPs (98%, 633097, lot# MKCM0616, Sigma Aldrich), 500 nm Si NPs (99.995%, US5011, U.S. Research Nanomaterials Inc.), and 44 μm Si microparticles (MPs, 99%, 215619, lot# MKCK6629, Sigma Aldrich). Multiple dilutions were performed at no higher than 10:1 in any given step to ensure homogeneity of mixing; mixing was performed for 5 min per step. The powder mixture was then transferred into a custom-made quartz ampule (0.8 cm inner diameter, 20 cm length) and a Swagelok ultra-torr adaptor was placed over the opening. The ampule was flame sealed at the pre-formed neck under rough vacuum. The ampule was then placed on an elevated rack at the center of a chamber furnace (CWF12/13, Carbolite-Gero) and heated to a final hold temperature via a PID controller (Eurotherm 3216) for a specified hold time via a specified ramp

rate. Temperature set point (800 or 1131 °C, L or H, respectively), hold time (0, 1, 6, 12 h), and ramp rate (5, 10, 20, 30, 50 °C min^{-1}) were varied accordingly. Finally, the samples were cooled by natural convection to below 100 °C and then opened using a diamond-bladed rotary saw under air. The so-obtained materials were analyzed or further used as collected (without washing). They are referred to herein by their nominal concentration (e.g., 0.1 at% SiP_x = 0.1P), temperature set point (e.g., 1131°C = H), hold time (e.g., 1 h = 1h), and ramp rate (e.g., 10 °C min^{-1} = 10R), as shown in Table 6.1.

Table 6.1. Naming convention for SiP_x materials based on synthesis protocol employed.

Synthetic Parameter Varied	Nominal P Content (at%)	Ramp Rate (°C min^{-1})	Temperature Setpoint (°C)	Hold Time (h)	Material
Control Si	0	(none)	(none)	(none)	Si (100 nm)
	0	(none)	(none)	(none)	Si (500 nm)
	0	(none)	(none)	(none)	Si (44 µm)
	0	5	1131	1	**0.0P**-5R-H-1h
P Content	0.05	5	1131	1	**0.05P**-5R-H-1h
	0.1	5	1131	1	**0.1P**-5R-H-1h
	0.2	5	1131	1	**0.2P**-5R-H-1h
	1.0	5	1131	1	**1.0P**-5R-H-1h
	3.0	5	1131	1	**3.0P**-5R-H-1h
Ramp Rate	0.1	5	1131	0	0.1P-**5R**-H-0h
	0.1	10	1131	0	0.1P-**10R**-H-0h
	0.1	20	1131	0	0.1P-**20R**-H-0h
	0.1	30	1131	0	0.1P-**30R**-H-0h
	0.1	50	1131	0	0.1P-**50R**-H-0h
Temperature	0.1	5	1131	1	0.1P-5R-**H**-1h
	0.1	5	800	1	0.1P-5R-**L**-1h
	0.1	5	800	0	0.1P-5R-**L**-0h
Hold Time	0.1	5	1131	0	0.1P-5R-H-**0h**
	0.1	5	1131	1	0.1P-5R-H-**1h**
	0.1	5	1131	6	0.1P-5R-H-**6h**
	0.1	5	1131	12	0.1P-5R-H-**12h**

Materials Characterization

XRD measurements were performed using a Bruker D8 Advance diffractometer with Cu Kα$_{1,2}$ radiation (λ=1.54 Å) in Bragg-Brentano geometry. Samples were prepared by physically mixing with a corundum (Al_2O_3) internal standard and mounted on an oriented silicon crystal (low background) holder.

Raman spectroscopy was performed using a HR Evolution spectrometer (Horiba Scientific Ltd.) equipped with a confocal microscope using a 532 nm (2.33 eV) frequency doubled Nd:YAG laser with an incident power of 45 mW. Two types of Raman measurements, referred to as

"surface" and "bulk," were collected by adjusting the focal point to ±10 μm from the plane of focus with maximum intensity.

SEM was performed using a Zeiss Supra 55VP microscope, operated at 1 kV. Samples were prepared for SEM by spreading a small quantity of powder onto conductive carbon tape. Electrical conductivity was measured under compression within a custom guard electrode setup using a Keithley 2450 sourcemeter as described elsewhere.[247]

<u>Electrode Materials</u>

The following materials were used in the preparation of electrochemical cells: lithium hexafluorophosphate ($LiPF_6$, battery grade, Gotion Inc.), ethylene carbonate (EC, battery grade, Gotion Inc.), dimethyl carbonate (DMC, battery grade, Gotion Inc.), fluoroethylene carbonate (FEC, battery grade, Gotion Inc.), lithium metal (chips, 99.9%, MTI Corp.), glass microfiber discs (0.67 × 257 mm, GF/D grade, catalogue number 1823–257, Whatman), carbon black (Super P, Timcal Ltd), carboxymethyl cellulose (CMC, batch #0011912, MTI), and copper foil (thickness: 9 μm, MTI Corp.).

<u>Electrode Fabrication</u>

Slurries were prepared by mixing SiP_x active material (80 wt%), conductive additive (Super P, 10 wt%) and binder (CMC, 10 wt%) in deionized water using an automatic mixer (Thinky AR-100). The slurry was cast onto Cu foil using a doctor blade and then subjected to a three-stage drying protocol: under air at room temperature for 8 h, under air at 80 °C for a further 8 h, and then lastly under rough vacuum (Welch Chemstar Dry 2071B) at 100 °C for a further 10 h. Electrodes were punched into disks with a diameter of 10 mm, and then stored under argon in a

glove box (<0.1 ppm H_2O/O_2) until further use. Homogenous loadings of 0.75-1.00 mg cm^{-2} were achieved across all electrodes reported herein.

Electrochemical Cell Fabrication

Half-cells were assembled under argon atmosphere in a glovebox (<0.1 ppm H_2O/O_2) in coin-cell format (316 stainless steel, size 2032, Xiamen AOT Electronics Technology Co.). An above described SiP$_x$ electrode served as the working electrode, a glass microfiber disk as the separator (16 mm diameter), and a Li chip as the counter electrode; the cell was flooded with 125 µL of 1.0 M LiPF$_6$ in EC/DMC (1:1 by weight) with 2 wt% FEC as the electrolyte and then closed.

Electrochemical Measurements

Galvanostatic charge/discharge cycling was performed in a temperature-controlled incubator (KB 53, Binder GmbH) at 25.0 °C using a battery cycler (CT30001A, Landt Instruments). Charge and discharge were performed using a constant current (CC) protocol at 1 A g^{-1} within the voltage range of 0.05-1.5 V vs. Li/Li$^+$.

Results

Homogenously Doped Silicon Nanoparticles

Homogeneously doped solid solutions of phosphorus in silicon (SiP$_x$ between 0.05-3.0 at% P) were first prepared via solid-state chemical reaction between large silicon NPs (of nominal size 500 nm) and red phosphorus in a closed ampule under vacuum. The hold temperature of dissolution (1131 °C) was initially held constant between all samples, and chosen based on the eutectic temperature between the Si solid solution and binary SiP, the equilibrium point of maximum solubility in Si. [115] A ramp rate of 5 °C min^{-1} and a hold time of 1 h were found to be sufficient

(the latter originally estimated based on diffusion rates[119, 248] of P in Si). Upon opening the ampule in air, no further reaction of the product occurred, indicating that the formation of white phosphorus was prevented. The initial dark-brown color of the precursor changed to dark gray as doping content increased (Figure 6.4), as consistent with previous reports for nanowires.[249, 250]
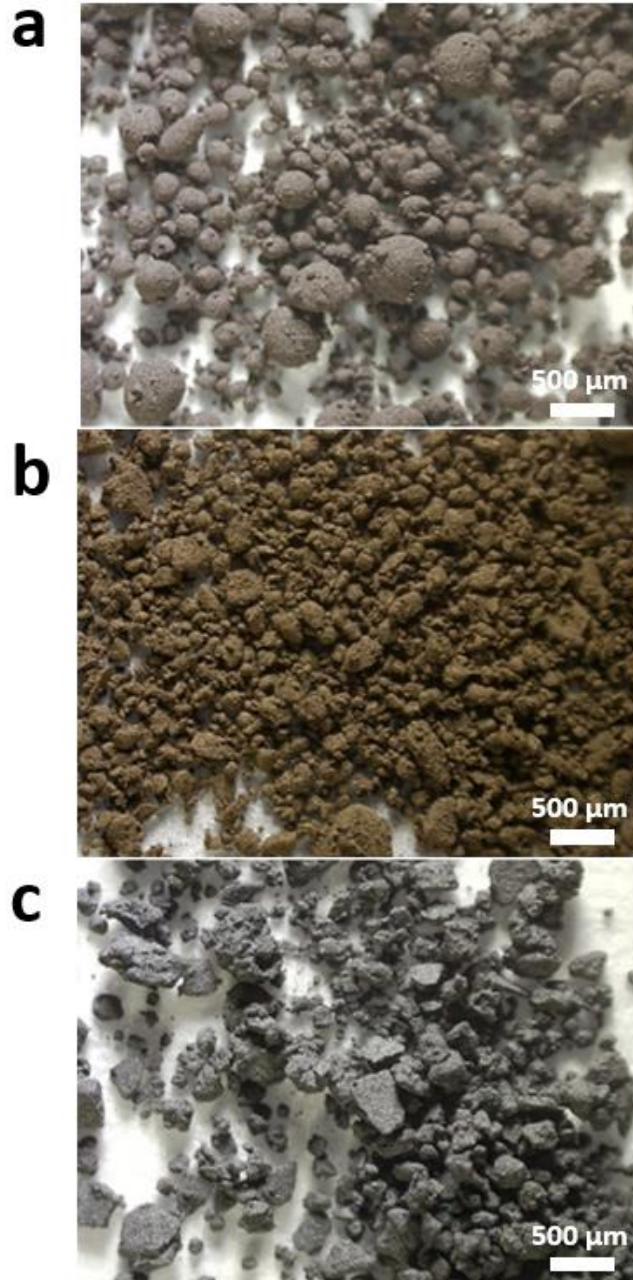
Figure 6.4. Photographs of (a) as-received pure Si, (b) 0.1 at% SiP_x, and (c) 3.0 at% SiP_x, all obtained from the same precursor: 500 nm Si NPs.

The systematic contraction of the Si lattice upon phosphorus substitution was verified by XRD measurements using an internal corundum standard (Figure 6.5); the change in lattice constant closely followed the previously reported trend by Olesinski which states that for 0.5 at%

P a 0.0001 nm contraction of the Si lattice can be expected .[115, 245, 246] Together, this is strong evidence of complete or near-complete incorporation of the phosphorus precursor within the silicon phase. Further analysis of the XRD patterns of the homogeneously doped SiP_x materials reveal larger average crystallite size (as calculated by the Scherrer equation) with increasing P content, compared to that of pure 500 nm Si NPs (even when subjected to the same heat-treatment at 1131 °C). This effect is corroborated by SEM analysis, showing obvious signs of grain coarsening and faceting of the SiP_x products, especially at high P-content (Figure 6.6).

The increase in phosphorus content is further confirmed by measuring the electrical conductivity using a two-probe technique. The properties of SiP_x materials based on 500 nm Si NPs are summarized in Table 6.2. Electrical conductivity of pure 500 nm Si NPs increases several orders of magnitude upon the addition of 0.1 at% P under homogenous doping conditions from 8.99×10^{-7} to 2.06×10^{-2} S cm^{-1}, a strong indication of successful P incorporation.
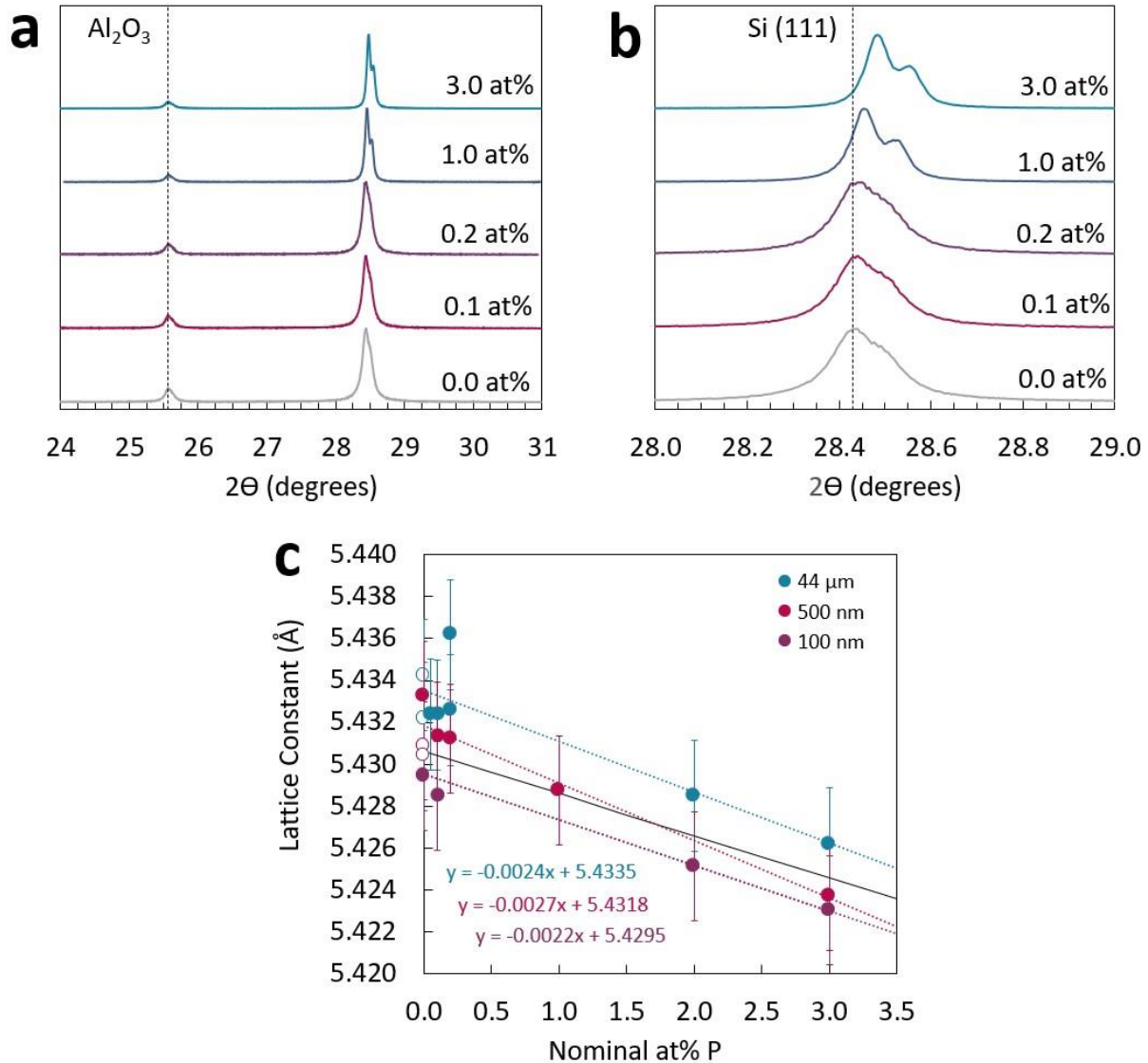
Figure 6.5. (a) XRD patterns of SiP$_x$ (from 500 nm Si NPs precursor) with nominal P content between 0.1-3.0 at% physically mixed with an internal corundum standard. (b) Detail of the Si(111) XRD peak. (c) Lattice parameter as a function of nominal P content across all three Si precursors investigated: 100 nm NPs, 500 nm NPs, and 44 μm MPs. The experimental line for crystalline P-doped Si obtained in previous studies[245, 246] is shown in black. All materials in (a-c) were obtained under heating at 5 °C min^{-1}, holding at 1131 °C, and holding for 1 h, except open symbols which represent as-received pure Si precursors.
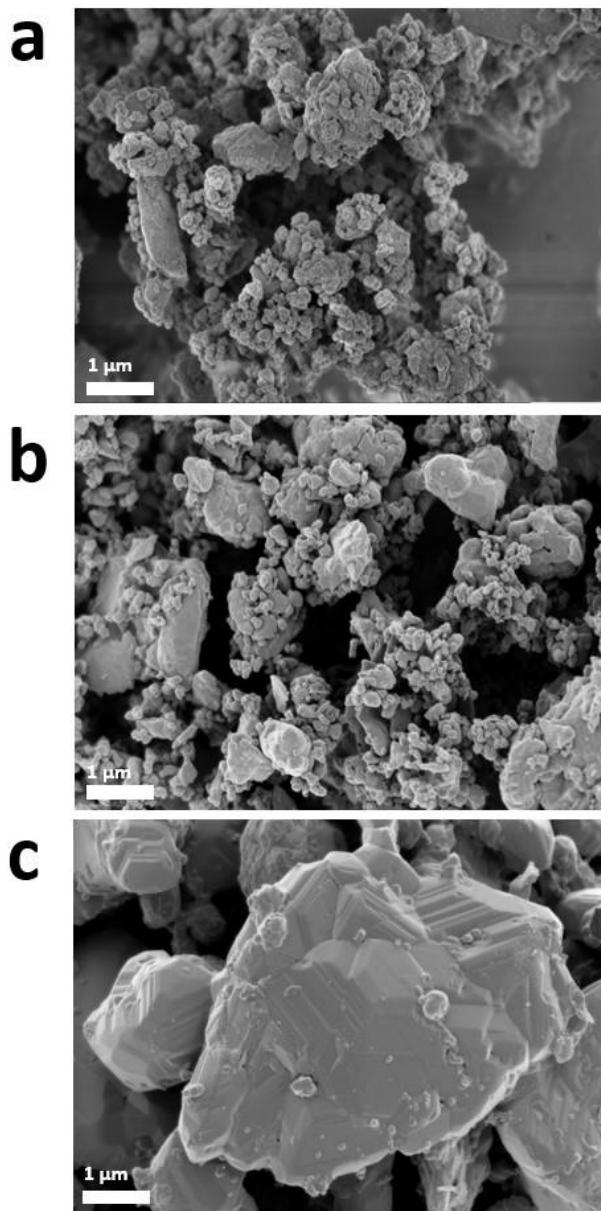
Figure 6.6. SEM micrographs of (a) as-received pure Si, (b) 0.1 at% SiP_x, and (c) 3.0 at% SiP_x, all obtained from the same precursor: 500 nm Si NPs. Materials in (b-c) were obtained under heating at 5 °C min^{-1}, and holding at 1131 °C for 1 h.

Table 6.2. Materials properties of SiP_x derived from 500 nm Si NPs, grouped by the synthetic parameter varied.

Synthetic Parameter Varied	Material	Si(111) 2θ (degree)	Si(111) FWHM (degree)	Lattice Parameter (Å)	Crystallite Size, L_a (nm)	Electrical Conductivity (S cm^{-1})
Control Si	**Si (500 nm)**	28.443	0.184	5.4309	8	8.99×10^{-7}
	0.0P-5R-H-1h	28.430	0.112	5.4332	13	4.33×10^{-4}
P Content	**0.05P**-5R-H-1h	28.430	0.110	5.4333	14	NM
	0.1P-5R-H-1h	28.440	0.105	5.4313	14	2.06×10^{-2}
	0.2P-5R-H-1h	28.441	0.107	5.4312	14	1.33×10^{-3}
	1.0P-5R-H-1h	28.454	0.064	5.4288	23	1.38×10^{-2}
	3.0P-5R-H-1h	28.481	0.060	5.4237	25	3.85×10^{1}
Ramp Rate	0.1P-**5R**-H-0h	28.437	0.124	5.4319	12	3.87×10^{-4}
	0.1P-**10R**-H-0h	28.436	0.139	5.4321	11	2.19×10^{-4}
	0.1P-**20R**-H-0h	28.435	0.137	5.4324	11	1.03×10^{0}
	0.1P-**30R**-H-0h	28.435	0.164	5.4323	9	4.99×10^{-2}
	0.1P-**50R**-H-0h	28.440	0.152	5.4314	10	2.21×10^{-1}
Temperature	0.1P-5R-**H**-1h	28.440	0.105	5.4313	14	NM
	0.1P-5R-**L**-1h	28.440	0.190	5.4314	8	NM
	0.1P-5R-**L**-0h	28.431	0.198	5.4330	8	3.30×10^{-7}
Hold Time	0.1P-5R-H-**0h**	28.437	0.120	5.4319	12	3.87×10^{-4}
	0.1P-5R-H-**1h**	28.440	0.105	5.4313	14	3.42×10^{0}
	0.1P-5R-H-**6h**	28.444	0.110	5.4307	14	1.03×10^{1}
	0.1P-5R-H-**12h**	28.434	0.110	5.4326	14	7.51×10^{1}
Optimal	0.1P-50R-L-0h	28.436	0.182	5.4319	8	2.80×10^{-7}

Raman spectroscopy of the homogeneously doped SiP_x materials reveals a slight decrease in frequency of the Raman-active mode for Si NPs centered at ~510 cm^{-1} (down to ~507 cm^{-1}) indicating that the introduction of phosphorus into silicon causes slight amorphization of the crystal structure in the dilute P regime (Figure 6.7a).[232, 251] With increasing P content, however, the peak center shifts back to higher frequency (516 cm^{-1}) indicating higher crystallinity of the resulting materials, as consistent with the XRD analysis. It is important to note that the Raman spectrum varies significantly depending on whether the focus is placed at or below the powder surface; measurements made at the surface (+10 μm from focus of highest intensity) show a

monotonic increase in position from 512 to 516 cm^{-1} with increasing P content, as shown in Figure

6.7b. This surface/bulk variability decreases significantly in SiP$_x$ samples doped beyond 1.0 at%,

indicative of a more homogenously crystalline structure. Lastly, a significant increase in

conductivity was observed in SiP$_x$ NPs as a function of P content (e.g., in the series xxP-5R-H-1h,

Table 6.2) as expected for homogeneously P-doped silicon.
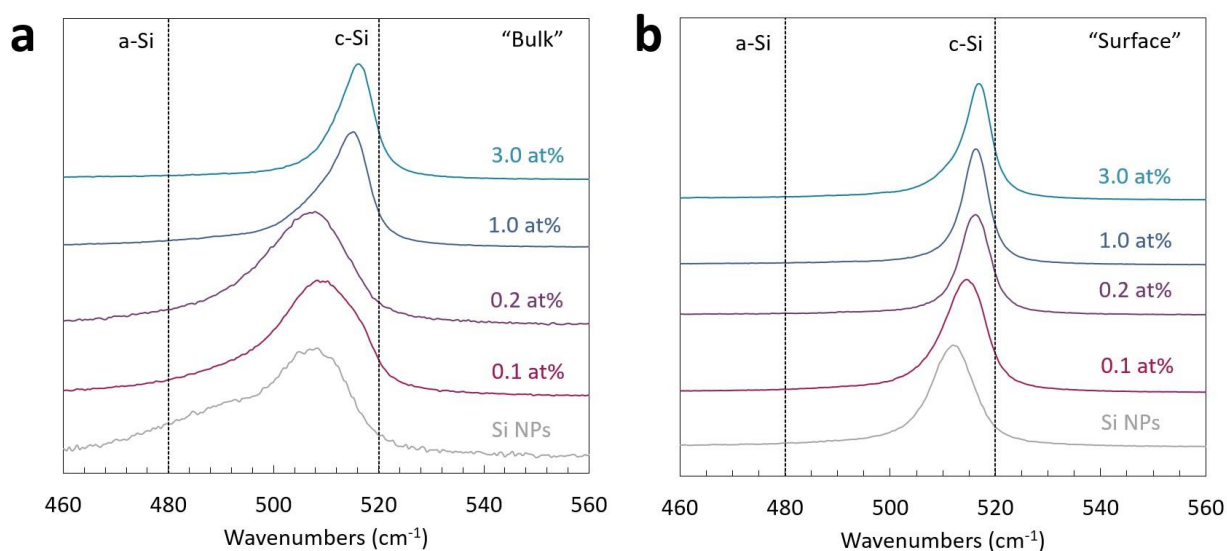
Figure 6.7. Raman spectroscopy of SiP$_x$ NPs measured (a) within the powder bulk and (b) directly at the powder surface, using 532 nm incident radiation. All materials were obtained from the same precursor (500 nm Si NPs) under heating at 5 °C min^{-1}, holding at 1131 °C for 1 h.

While homogeneous solid solutions of SiP$_x$ across the entire solubility range could be

achieved by facile solid-state reaction between Si NPs and red phosphorus, P content and

crystallite/particle size were found to be convoluted within this series. To control for these effects

separately, two additional Si precursors of different nominal particle sizes (100 nm and 44 μm)

were also investigated. Similar changes in lattice constant, color, and Raman spectral features were

observed, as summarized in Table 6.3 and Figure 6.8. Hence, these materials were subsequently

used to decouple the effects of particle size and P content on the electrochemical behavior of

anodes based on silicon NPs and MPs. Additionally, pure 500 nm Si NPs were heat-treated under inert atmosphere (in identical conditions as for P-doping, except without any phosphorus) to attempt to control for the role of the heat treatment itself on crystallinity and grain size. Indeed, a slight increase in crystallite size (from 8 to 13 nm) was observed for heat-treated Si NPs (0.0P-5R-H-1h). However, this effect is much smaller than that observed for heat treatment in the presence of the phosphorus (see Figure 6.8), indicating that the red phosphorus itself catalyzed the growth of crystallites and associated particle size and morphology changes.

Table 6.3. Materials properties of SiP_x derived from 100 nm Si NPs (-n) and 44 μm Si MPs (-μ), grouped by the synthetic parameter varied.

Synthetic Parameter Varied	Material	Si(111) 2θ (degree)	Si(111) FWHM (degree)	Lattice Parameter (Å)	Crystallite Size, L_a (nm)
P Content (100 nm)	Si (100 nm)	28.445	0.290	5.4303	5
	0.0P-5R-H-1h-n	28.450	0.154	5.4294	10
	0.1P-5R-H-1h-n	28.455	0.163	5.4284	9
	2.0P-5R-H-1h-n	28.473	0.060	5.4251	24
	3.0P-5R-H-1h-n	28.484	0.070	5.4230	21
P Content (44 μm)	Si (44 μm)	28.425	0.065	5.4343	23
	0.0P-5R-H-1h-μ	28.428	0.062	5.4336	24
	0.05P-5R-H-1h-μ	28.435	0.074	5.4324	20
	0.1P-5R-H-1h-μ	28.435	0.062	5.4323	24
	0.2P-5R-H-1h-μ	28.433	0.081	5.4326	18
	2.0P-5R-H-1h-μ	28.456	0.068	5.4285	22
	3.0P-5R-H-1h-μ	28.468	0.067	5.4262	22
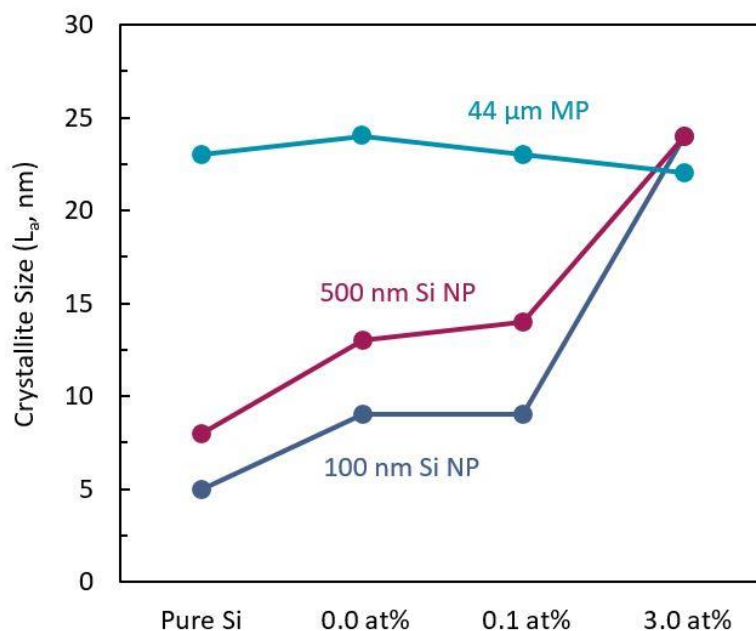
Figure 6.8. Crystallite size as a function of phosphorus doping shown for three different sized Si precursors (100 nm, 500 nm, and 44 μm). Si and SiP$_x$ materials were treated under the following conditions: xxP-5R-H-1h.

Heterogeneously Doped Silicon Nanoparticles

A second series of experiments was carried out to obtain a wider variety of SiP$_x$ materials for electrochemical analysis. Three strategies were employed to obtain materials with a heterogeneous distribution of dopant within the silicon lattice: increasing the ramp rate (5-50 °C min^{-1}), decreasing the hold temperature (1131-800 °C), and decreasing the hold time during solid-solution preparation (1-0 h). The properties of the so-obtained materials are summarized in Table 6.2. This work focuses on dilutely P-doped SiP$_x$ materials (0.1 at%) which are of highest interest to the subsequent electrochemical analyses. Generally, the results reveal that at a fast ramp rate (> 30 °C min^{-1}), low temperature (800 °C heat), and a short time spent at highest temperature (0 h hold time), the crystallite size of the resulting material is close to that of pure 500 nm Si NPs.

Raman spectroscopy and SEM analysis further confirm that the silicon crystallinity and morphology are minimally affected under rapid, short hold, and low temperature dissolution conditions. The diffusion of phosphorus within silicon increases from $\sim 2\times10^{-18}$ to 1×10^{-15} m^2 s^{-1} as its concentration increases from 0.1 to 10 at% at 1131 °C.[119, 248] An approximate estimate of diffusion depth as a function of time reveals that the homogeneous dissolution of 0.1 at% phosphorus in 500 nm Si NPs requires 5 h to complete. Hence, by using ramp rates up to 50 °C min^{-1} and no hold time, a heterogeneously distributed SiP_x solution is expected to result. Importantly, all rapidly doped SiP_x materials exhibit a similar structure to the original Si NPs (Figure 6.9). There is no enhancement of conductivity when phosphorus is heterogeneously doped at low temperatures (e.g., for 0.1P-50R-L-0h); rather, a significant decrease in conductivity is observed (Table 6.2). At high temperatures, however, an increase in conductivity can be observed with increasing ramp rate (e.g., for 0.1P-xxR-H-0h) and is likely attributed to a surface mechanism of these heterogeneous structures. The electrochemical properties of such heterogeneously doped (e.g., surface modified) SiP_x variants are explored and compared to homogeneously doped samples in the following section.
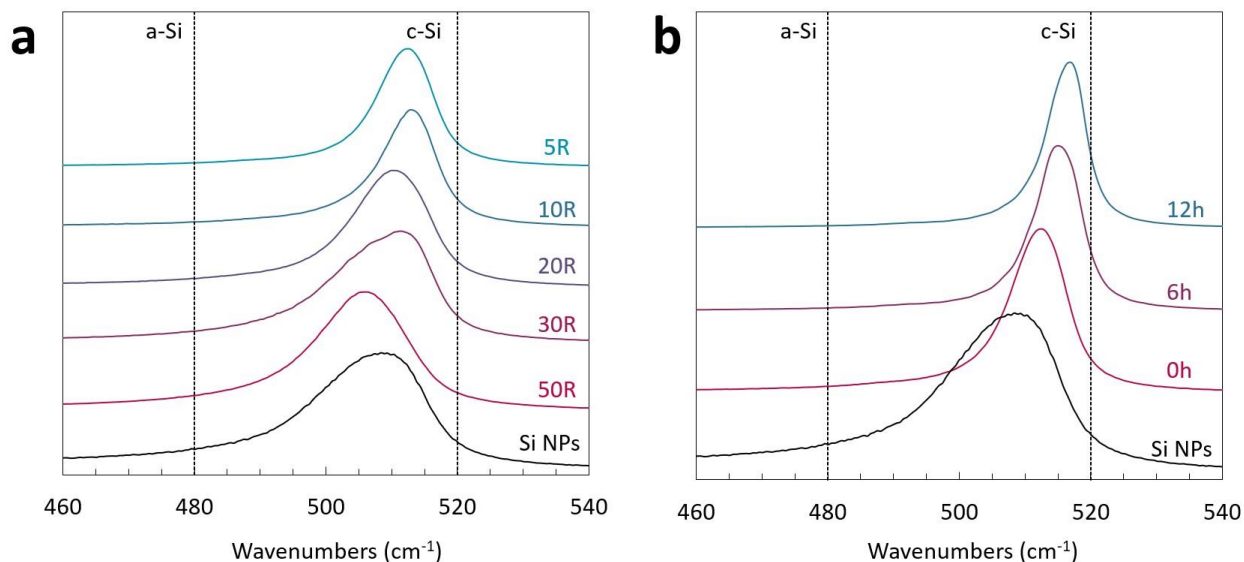
Figure 6.9. Raman spectroscopy of SiP$_x$ NPs synthesized under (a) different ramp rates (0.1PxxR-H-0h) and (b) different hold times (0.1P-5R-H-xxh), using 532 nm incident radiation. All materials were obtained from the same precursor (500 nm Si NPs).

Electrochemical Studies

Galvanostatic charge discharge (GCD) cycling was used as the primary means of assessing electrochemical effects related to P-doping (and other concomitant changes to the materials properties such as increased crystallite or particle size) of Si NPs. The samples of highest interest were obtained from 500 nm Si NPs; when not otherwise indicated, all subsequent results relate to SiP$_x$ obtained from this precursor. Electrodes for each sample were prepared using a standard drop-casting method to control for effects such as adhesion and in an effort to make the results widely generalizable to other electrode fabrication techniques (e.g., to ensure as much as possible that the results relate to materials properties and not to electrode properties). An aqueous binder (CMC) was used and the electrodes were fabricated under air. Half-cells were assembled under inert argon against Li metal as the counter electrode and in flooded electrolyte, in an effort to ensure reproducibility of the results. A standard liquid electrolyte was chosen (1 M LiPF$_6$ in EC/DMC)

with a modest amount of FEC (2 wt%) to inhibit excessive SEI (re)formation. Lastly, GCD cycling at a constant current rate of 1 A g^{-1} (~C/3) was employed, between 0.05-1.5 V vs. Li/Li$^+$ to prevent the formation of crystalline Li$_{15}$Si$_4$.

In all cases, a steep loss of capacity of the SiP$_x$ NPs was observed in the first cycles; this was followed by a less severe decline in most cases until zero capacity remained (at or before the 200th cycle in all cases herein). In general, cells based on 500 nm NPs were observed to show more significant capacity fading than those based on 100 nm NPs, an expectable effect due to particle size (See Appendix J).[73, 252] Despite that electrochemical performance was not optimized in this work, this electrode and half-cell formulation allowed for a facile intercomparison between all of the materials investigated and only the *relative* outcome of each experiment is the focus of discussion herein. The decline in capacity during initial GCD cycling (1-25 cycles) is attributable to volume expansion and contraction and subsequent loss of electrical contact with a portion of the active SiP$_x$ material. In most cases, this initial capacity loss diminishes for some cycles (showing a seeming approach to a non-zero plateau) and then capacity fade again intensifies until zero capacity is reached. The latter effect is attributable to the formation and non-uniform dissolution of "mossy lithium"[253] which was a well-known failure mechanism in lithium metal batteries.[254] The use of a stable intercalation compound as the counter electrode instead of Li metal (e.g., LiFePO$_4$) would likely resolve the latter issue and will be a focus of future investigations.

Electrochemical Effects of Homogeneous P-Doping

The GCD voltage profiles of dilutely-doped SiP$_x$ materials obtained under conditions that lead to homogenous doping (i.e., high temperature, long hold time, and slow ramp rate) with P content varying between 0.05-0.2 at% are shown in Figures 6.10a-c. The corresponding capacity

retention and Coulombic efficiency within the first 200 cycles at up to 1.0 at% is shown in Figure 6.10d. Higher P content samples (>1.0 at%) did not cycle with any capacity at the benchmark 1 A g^{-1} current employed in this study. All lower concentration SiP_x NPs show comparable second cycle discharge capacities of 2.5-2.9 Ah g^{-1}; materials doped with 1.0 at% P show grievous capacity loss upon cycling, reaching effectively zero capacity within the first 10 cycles. This cycling instability can likely be attributed to larger crystallite size than the pure Si NPs. This explanation is supported by comparison to the cycling instability of pure Si MPs (Appendix J). On the other hand, SiP_x NPs in the most dilute doping regime (≤ 0.1 at% P) exhibited higher cycling stability than the pure Si NPs. It is important to note that this difference in stability cannot be attributed to significant lattice contraction or to smaller crystallite size (see Table 6.2) and therefore *must be owed to the presence of P in the lattice*. Slower ramp rates and longer hold times during phosphorus dissolution in general give rise to larger crystallites and grain coarsening, and therefore to poorer cycling stability. It remains unknown whether, if higher concentration SiP_x NPs could be prepared at the same particle size as the native Si NPs, they would show longer cycling stability yet than the low P content SiP_x NPs that exhibit the longest cycling stability in this study.
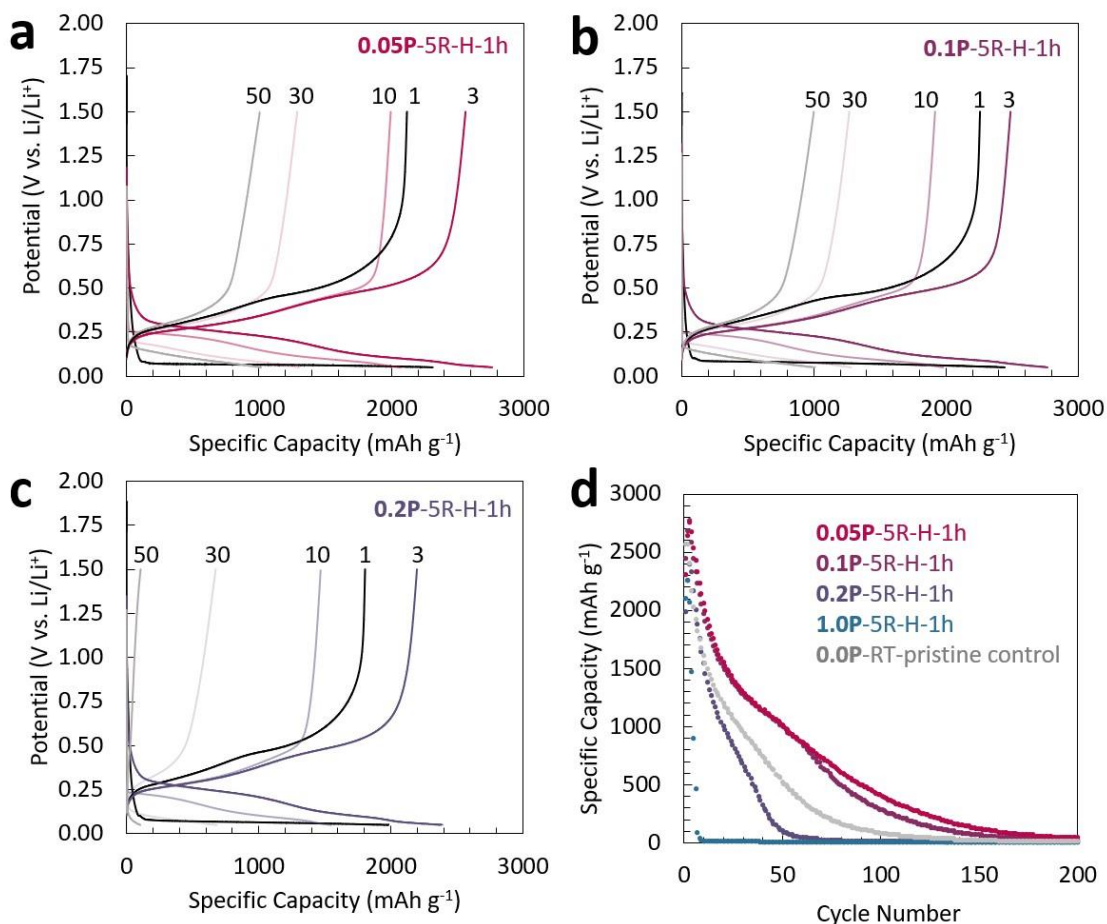
Figure 6.10. (a–c) GCD lithiation voltage profiles and capacity retention of SiP$_x$ NPs synthesized under homogeneous doping conditions compared to pure Si NPs. Three compositions of highest interest are highlighted: (a) 0.05 at%, (b) 0.1 at%, and (c) 0.2 at% P. The cycle number of each profile is indicated. (d) GCD lithiation capacity retention and Coulombic efficiency of homogeneously doped SiP$_x$ NPs.

Electrochemical Effects of Heterogeneous P-Doping

SiP$_x$ NPs prepared using fast ramp rates, short hold times, and low dissolution temperatures generally exhibit improved capacity compared to pristine 500 nm Si NPs. The effect of ramp rate (at 5, 10, 20, and 50 ℃ min^{-1}) on cycling retention is shown in Figure 6.11a. SiP$_x$ NPs obtained at fast ramp rates (≥ 20 ℃ min^{-1}) maintain crystallite sizes (L$_a$ = 9-11 nm) comparable to pure Si NPs (L$_a$ = 8 nm) (see Table 6.2) and also exhibit the highest capacity retention. The effect of hold time

(for 0, 1, 6, and 12 h) on capacity retention is shown in Figure 6.11b (also shown in Figure 6.12a). SiP_x NPs with the least amount of hold time (0 and 1 h) exhibit high capacity and stability compared to pure Si NPs, whereas longer hold times (6 and 12 h) result in earlier capacity fading, worse than that exhibited by pure Si NPs. Interestingly, pure Si NPs held at 0, 1, 6, or 12 h hold times (e.g., annealed at 1131 °C) exhibit no difference in electrochemical behavior (Figure 6.12b) nor in crystallite size (Figure 6.13) than pristine Si NPs. This is strong evidence that the addition of phosphorus to the Si NPs is the primary cause for grain coarsening via a catalytic (crystallization) effect, leading to poor capacity retention when present at high concentrations. Lastly, the effect of dissolution temperature (at 800 or 1000 °C) on capacity retention is shown in Figure 6.11c. Based on the equilibrium binary Si-P phase diagram, a temperature of 800 °C is in principle sufficient to achieve a doping of 0.3 at% P.[115] Based on GCD cycling analysis, SiP_x NPs synthesized at lower temperature (800 °C) with no hold time (0 h) exhibit the highest capacity and cycling stability compared to SiP_x materials synthesized at higher temperatures and also retain extremely small crystallite size (L_a = 8 nm) equivalent to pure Si NPs. Interestingly, such heterogeneously doped SiP_x materials in general do not exhibit improved electrical conductivity compared to pure Si (Table 6.2). Hence, the role of improved electrical conductivity as the sole reason for improved capacity retention can be ruled out by these results.
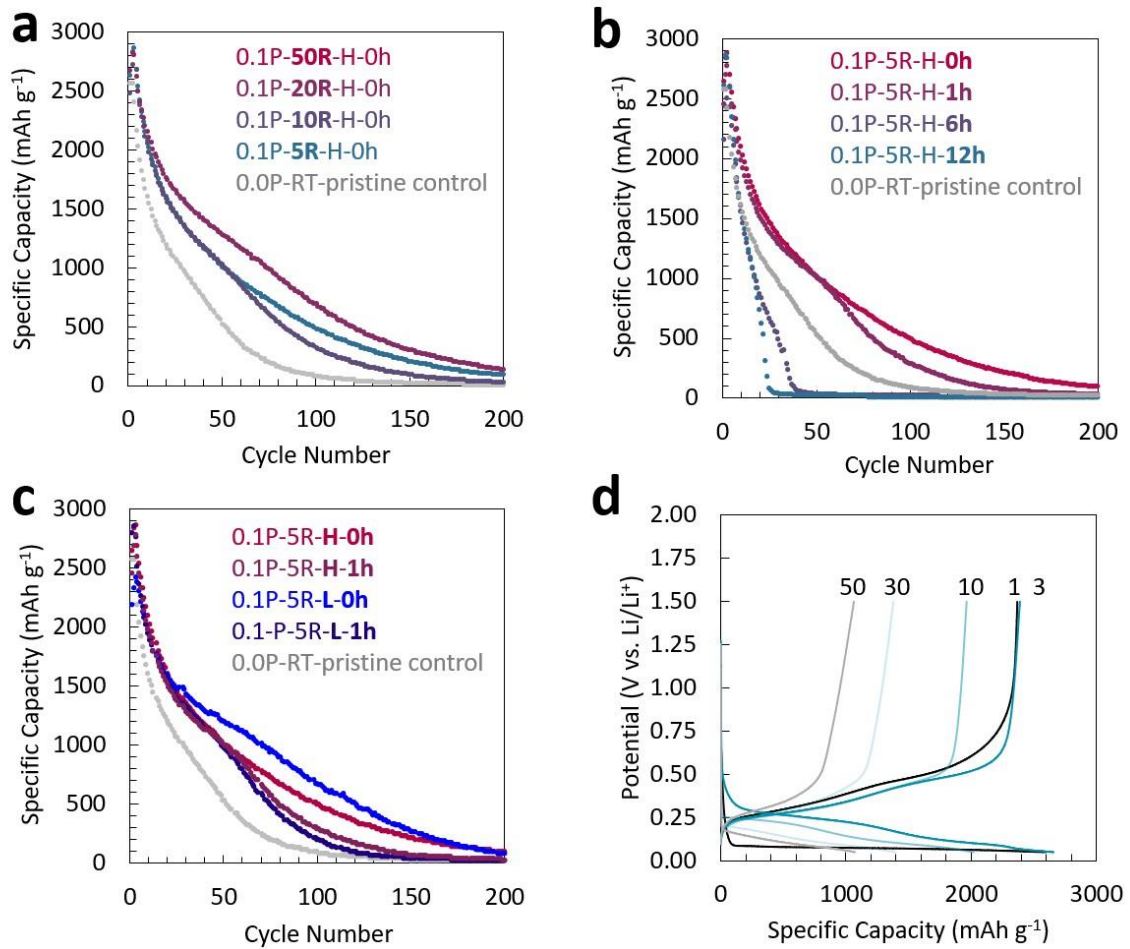
Figure 6.11. (a–c) GCD lithiation capacity retention of SiP$_x$ NPs synthesized under heterogeneous doping conditions. The effects of (a) ramp rate, (b) hold time, and (c) high temperature are shown for comparison to pure Si NPs. (d) GCD lithiation voltage profiles of SiP$_x$ NPs synthesized under optimal heterogeneous conditions. The cycle number of each profile is indicated.
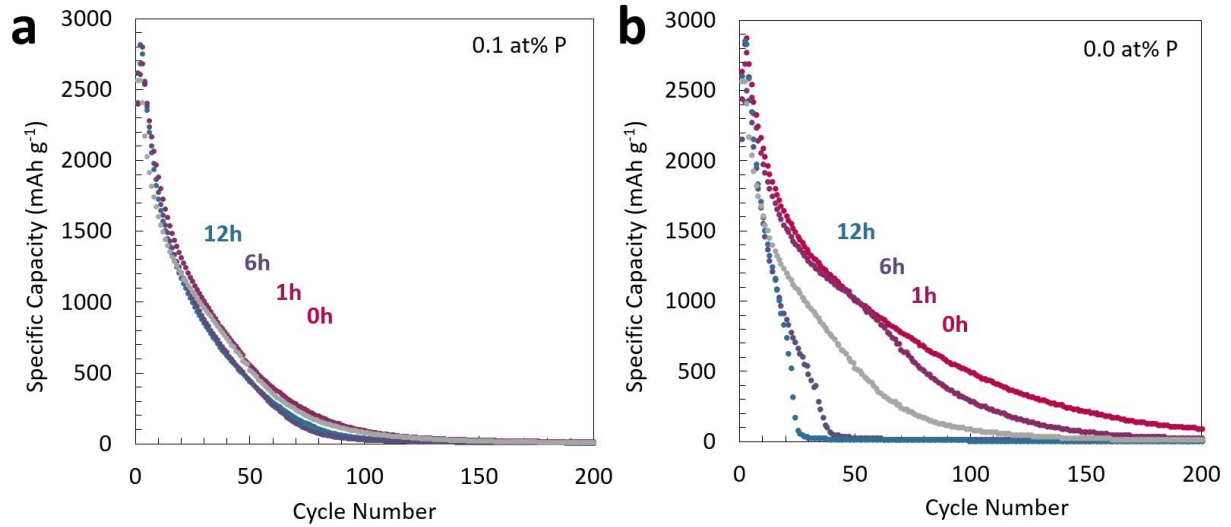
Figure 6.12. Capacity retention of a) 0.1 at% doped and b) undoped Si NPs at different hold times. All materials in (a-b) were obtained under heating at 5 °C min^{-1} and holding at 1131 °C.
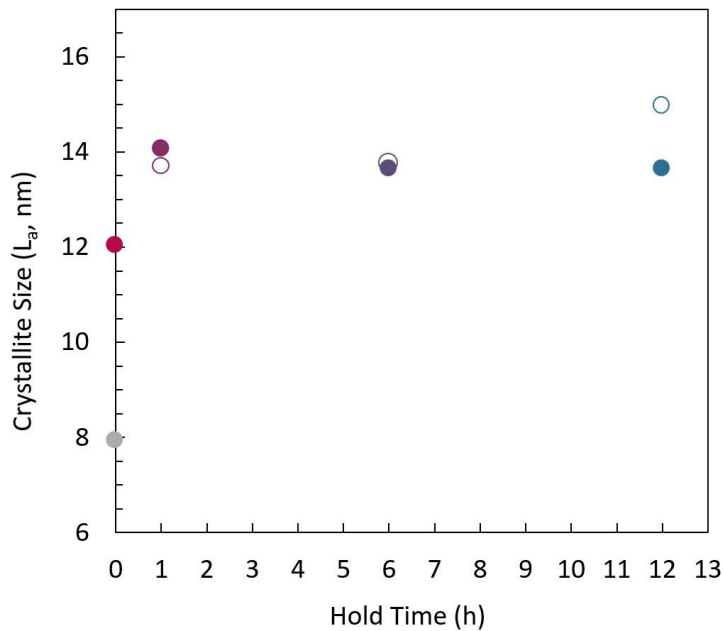
Figure 6.13. Crystallite size as a function of hold time (0, 1, 6, and 12 h) for undoped Si NPs (open circles) and 0.1 at% P doped Si NPs (closed circles) synthesized under the following conditions (0.1P-5R-H-xxh). The closed grey circle is pure Si NP as received.

The consequences of P-doping toward thermal stability were preliminarily explored by TGA and electrochemical experiments (see Appendix K). In general, P-doping was observed to increase the thermal decomposition temperature, though the effects were difficult to decouple from grain coarsening (e.g., reduction in surface area) effects. Further analysis of the thermal stabilizing effects of P-doping on SiP_x anodes will be carried out in future work to further understand the role of phosphorus in the silicon lattice.

Discussion

This work investigates the sole effects of P-doping on the electrochemical stability of Si, independent of the effects due to altering particle morphology/size, in a standard liquid-electrolyte cell configuration. Standard electrode fabrication methods using powder active material and liquid slurry casting were favored requiring the P-doping of existing Si powder. This is distinct from previous investigations of P-doped silicon electrodes prepared by a gas deposition (GD) method.[232] Correspondingly, there is a significant difference in the results. While Domi et al. reported monotonically increasing electrochemical stability as a function of P-content, this work reveals a trade-off between P-content and silicon particle size/crystallinity that results in a maximum electrochemical stability at an intermediate P-content. Remarkably, both studies favor an optimal P-content around 0.1 at% (though in the GD-prepared electrodes, this was the highest P-content investigated). Further differences are revealed in the effects of P-doping on lithiation capacity. In this work, initial capacities within the first several cycles did not vary significantly as a function of P-doping; the effects of P-doping (and likewise of crystallite and particle size) were only revealed in terms of capacity retention. In other words, P-doping did not restrict the ultimate lithiation capacity of silicon. In the results reported by Domi and coworkers, P-doping seemed to

decrease the ultimate lithiation capacity of the GD-prepared electrodes, though cycling retention was improved. These differences persist despite both studies using the same current rate of 1 A g^{-1}. Other past studies (theoretical and experimental) of P-doping silicon anodes for LIBs place a high emphasis on the effects due to enhanced electrical conductivity over that of pure silicon.[255, 256] Interestingly, while an increase in conductivity as a function of P-doping was measured and might help explain electrochemical differences within the homogeneously doped (e.g., xxP-5R-H-1h) series in this work, only very low conductivities were measured in the heterogeneously doped samples which had the highest overall electrochemical stability (e.g., 0.1P-50R-L-0h). Hence, we cannot attribute improved electrochemical stability to increased conductivity within the range of conditions explored herein, and future work is needed to decouple these properties.

Within the synthetic conditions explored in this study, low P content (≤ 0.1 at% P), fast ramp rate (e.g., 50 °C min^{-1}), short hold time (0 h), and low synthesis temperature (800 °C) together give rise to the highest capacity retention of SiP$_x$ NPs within the electrochemical conditions of interest in this study: ~C/3 cycling between 0.05-1.5 V vs. Li/Li$^+$ in a standard carbonate electrolyte. It is very challenging to confirm the homogeneity of doping in Si NPs owing to the low phosphorus concentration inherent to the top-performing materials (typically 0.1 at% P). Two methods were attempted to be used herein: time-of-flight secondary ion mass spectrometry (TOF-SIMS) and X-ray photoelectron spectroscopy (XPS). Unfortunately, neither method was reliably successful at determining the P content homogeneity as a function of depth below the Si NP surface. Nevertheless, there is strong evidence in the overall body of work reported herein that a heterogeneous distribution of dilute phosphorus within SiP$_x$ NPs (e.g., a core-shell structure) enhances the overall capacity retention in LIB anode applications.

Conclusions and Future Work

Homogeneous and heterogeneous doping of phosphorus within silicon NPs was achieved by varying a wide range of synthetic parameters. A top-down solid-state synthesis route was employed allowing for facile fine tuning of the final SiP_x product. An important goal of this work was to determine the role for phosphorus doping in silicon towards electrochemical stability. To that end, the addition of phosphorus in dilute quantities (0.1-0.5 at%) does in fact improve electrochemical performance of LIBs in standard carbonate electrolyte. Further, materials prepared under heterogenous doping conditions (low temperature set point (800 °C), no hold time (0 h), and fast ramp rate (50 °C min^{-1})) give rise to even better electrochemical stability compared to homogenous SiP_x. The exact origin of these effects is not understood at this time; future work should explore how P doping influences SEI formation and thermal stability of silicon particles. Lastly, a natural extension of this work should investigate alternative dopants (Al, B, Ca, Mg, and Zn) to establish doping selection guidelines for future stabilization of silicon anodes.

CHAPTER SEVEN

CONCLUSIONS

Doping Outlooks

This body of work investigates three different material systems which are interconnected by the common theme of substitutional doping; phosphorus-doped graphitic carbon, aluminum-doped graphitic carbon, and phosphorus-doped silicon. Initial goals were to explore how substitutional doping alters structural and chemical properties of graphitic carbon and silicon materials prepared by bottom-up and top-down strategies. Doping success can be evaluated by synthesis strategy employed (e.g., bottom-up versus top-down), and importantly dopant selection within a given material system. We find that while co-pyrolysis of phosphorus- and aluminum-doped graphitic carbon materials offers immense control over synthetic parameters and self-assembly on the atomic/molecular level a limitation exists in that precursors tend towards their most thermodynamically favorable phase. Top-down synthesis of phosphorus-doped silicon, on the other hand, was incredibly successful which can be attributed to diffusion controlled and vacancy mediated doping. This work sheds light on the challenging nature of doping without formation of byproducts, phase segregation, or changes to materials crystallinity and morphology.

Application Outlooks

Phosphorus-doped graphitic carbon and silicon materials are studied electrochemically. In the latter system we are able to successfully incorporate phosphorus into the silicon lattice and show that the addition of phosphorus significantly improves electrochemical performance and

stability compared to pure silicon nanoparticles. This is an important contribution to the battery community as the use of silicon anodes is becoming widespread. At present pure silicon anodes are not commercially viable without the use of carbon composites. This work offers insight towards the stabilization of silicon anodes in the absence of composites to leverage silicon's full capacity. Additionally, we introduce a scalable solution for the synthesis of phosphorus-doped silicon through a facile solid-state synthesis method. In summary, our work establishes a fundamental understanding of the role of phosphorus dopants in silicon anodes.

In an unsuccessful attempt to dope graphitic carbon with phosphorus, we discover the formation and control of phosphorus allotropes by altering the trihalide precursor. Resulting phosphorus-carbon composite materials are promising anode materials owing to phosphorus's high theoretical capacity and enhanced electrical conductivity provided by the carbon scaffold. Moreso, we identify the reversible lithiation of white phosphorus, stabilized between graphitic sheets, representing a novel and previously unreported electrochemical process. Findings from this work lend insight towards the development of next-generation phosphorus-based anode materials beyond silicon.

Future Work

Future work should continue to explore novel synthetic routes towards obtaining metastable heteroatom-doped graphitic carbon. A wide range of control over synthesis parameters is allowed by the current bottom-up co-pyrolysis technique. Synthesis temperatures and reaction pressures beyond 1200 °C and 20 bar need exploring. Reaction mixtures of more than one heteroatom containing precursor may lead to an interesting new class of material especially in the case of phosphorus/carbon composites. In the case of aluminum doping, side reactions of

aluminum precursors with the quartz reactor wall necessitate the need for oxygen-free reactor vessels such as tantalum to prevent formation of byproducts.

We learn that for phosphorus doping in graphitic carbon, precursor selection matters; the resulting phosphorus allotropes can be related to decomposition energies of the phosphorus and carbon containing precursor. All future selections of precursors for heteroatom-doped graphitic carbon should undergo a screening process to down select precursors of similar decomposition energies and temperatures.

Phosphorus/carbon composites reveal that carbon-stabilized white phosphorus is a viable high-density and rapid-charging lithium storage material despite its reputation for reactivity in the bulk. Future work is warranted to determine the ultimate density and dispersion of stabilized white phosphorus in phosphorus/carbon composite materials. At present phosphorus/carbon composite materials exhibit remarkably similar chemistry at 0.02 A g^{-1} and 1 A g^{-1}. Further, rate capability testing is needed to determine kinetic limitation of these materials.

Homogenous and heterogeneously doped silicon both show improved electrochemical performance compared to pure silicon anodes. From a materials perspective, we successfully decouple the effects of phosphorus from crystallite size and silicon particle size. Future work is needed to understand how phosphorus influences SEI formation, a potential contributing factor to the stabilization of silicon anodes. Lastly, exploration of alternative dopants in silicon to include aluminum, boron, calcium, magnesium, and zinc is needed to establish dopant selection guidelines for the stabilization of silicon anodes.

REFERENCES CITED

(1) Alanazi, F. Electric Vehicles: Benefits, Challenges, and Potential Solutions for Widespread Adaptation. *Appl. Sci.* **2023**, *13* (10).

(2) Ban, M.; Yu, J.; Li, Z.; Guo, D.; Ge, J. Battery Swapping: An aggressive approach to transportation electrification. *IEEE Electrification Magazine* **2019**, *7* (3), 44-54.

(3) Form, A.; Hultberg, A.; Berry, C. *Polestar and Rivian pathway report*; 2023.

(4) Mills, M. P. *Electric Vehicles for Everyone? The Impossible Dream*; Manhattan Institute 2023.

(5) FACT SHEET: Biden - Harris Administration Announces New Standards and Major Progress for a Made-in-America National Network of Electric Vehicle Chargers. 2023.

(6) Xie, J.; Lu, Y. C. A retrospective on lithium-ion batteries. *Nat. Commun* **2020**, *11* (1), 2499, From NLM PubMed-not-MEDLINE.

(7) Suarez, C.; Martinez, W. Fast and Ultra-Fast Charging for Battery Electric Vehicles - A Review. In *IEEE Energy Conversion Congress and Exposition (ECCE)*, Baltimore, MD, USA, 2019; IEEE: pp 569-575.

(8) Goodenough, J. B. How we made the Li-ion rechargeable battery. *Nat. Electron.* **2018**, *1* (3), 204-204.

(9) Whittingham, M. S. Electrical Energy Storage and Intercalation Chemistry. *Science* **1976**, *192*, 1126-1127.

(10) Yoshino, A. Breif-History and Future of the Lithium-Ion Battery. *The Nobel Prizes 2019* **2022**, 207-218.

(11) Asenbauer, J.; Eisenmann, T.; Kuenzel, M.; Kazzazi, A.; Chen, Z.; Bresser, D. The success story of graphite as a lithium-ion anode material – fundamentals, remaining challenges, and recent developments including silicon (oxide) composites. *Sustain. Energy Fuels* **2020**, *4* (11), 5387-5416.

(12) Wang, C.; Yang, C.; Zheng, Z. Toward Practical High-Energy and High-Power Lithium Battery Anodes: Present and Future. *Adv. Sci. (Weinh.)* **2022**, *9* (9), e2105213.

(13) Wang, R.; Cui, W.; Chu, F.; Wu, F. Lithium metal anodes: Present and future. *J. Energy Chem.* **2020**, *48*, 145-159.

(14) Scrosati, B. Lithium Rocking Chair Batteries: An Old Concept? *J. Electrochem. Soc* **1992**, *139*, 2776-2781.

(15) Xu, B.; Qian, D.; Wang, Z.; Meng, Y. S. Recent progress in cathode materials research for advanced lithium ion batteries. *Mater. Sci. Eng. R Rep.* **2012**, *73* (5-6), 51-65.

(16) Noel, M.; Santhanam, R. Electrochemistry of graphite intercalation compounds. *J. Power Sources* **1998**, *72* (1), 53-65.

(17) Legrand, A. P.; Flandrois, A. *Chemical Physics of Intercalation*; Springer Science and Media, 2013.

(18) McDowell, M. T.; Lee, S. W.; Nix, W. D.; Cui, Y. 25th anniversary article: Understanding the lithiation of silicon and other alloying anodes for lithium-ion batteries. *Adv. Mater.* **2013**, *25* (36), 4966-4985, From NLM Medline.

(19) Park, C. M.; Kim, J. H.; Kim, H.; Sohn, H. J. Li-alloy based anode materials for Li secondary batteries. *Chem. Soc. Rev.* **2010**, *39* (8), 3115-3141.

(20) Franco Gonzalez, A.; Yang, N.-H.; Liu, R.-S. Silicon Anode Design for Lithium-Ion Batteries: Progress and Perspectives. *J. Phys. Chem. C* **2017**, *121* (50), 27775-27787.

(21) Li, J.; Hwang, S.; Guo, F.; Li, S.; Chen, Z.; Kou, R.; Sun, K.; Sun, C. J.; Gan, H.; Yu, A.; et al. Phase evolution of conversion-type electrode for lithium ion batteries. *Nat. Commun* **2019**, *10* (1), 2224.

(22) Bhatt, M. D.; Lee, J. Y. High capacity conversion anodes in Li-ion batteries: A review. *Int. J. Hydrogen Energy* **2019**, *44* (21), 10852-10905.

(23) Wang, F.; Robert, R.; Chernova, N. A.; Pereira, N.; Omenya, F.; Badway, F.; Hua, X.; Ruotolo, M.; Zhang, R.; Wu, L.; et al. Conversion reaction mechanisms in lithium ion batteries: study of the binary metal fluoride electrodes. *J. Am. Chem. Soc.* **2011**, *133* (46), 18828-18836.

(24) Bard, A. J.; Faulkner, L. R. *Electrochemical Methods: Fundamentals and Applications, 2nd Edition*; 2000.

(25) Herold, A.; Guerard, D. Intercalation of lithium into graphite and other carbons. *Carbon* **1975**, *13* (4), 337-345.

(26) Basu, S.; Zellar, C.; Flanders, P. J.; Fuerst, C. D.; Johnson, W. D.; Fischer, J. E. Synthesis and properties of lithium-graphite intercalation compounds. *Mater. Sci. Eng.* **1979**, *38* (3), 275-283.

(27) Fong, R.; Sacken, U. v.; Dahn, J. R. Studies of Lithium Intercalation into Carbons Using Nonaqueous Electrochemical Cells. *J. Electrochem. Soc.* **1990**, *137*, 2009-2013.

(28) Hofmann, U.; Rüdorff, W. The formation of salts from graphite by strong acids. *Trans. Faraday Soc.* **1938**, *34*, 1017.

(29) Daumas, N.; Herold, A. Relations between phase concept and reaction mechanics in graphite insertion compounds. *C. r. hebd. séances Acad. sci.* **1969**, *268* (5), 373-&.

(30) Persson, K.; Sethuraman, V. A.; Hardwick, L. J.; Hinuma, Y.; Meng, Y. S.; van der Ven, A.; Srinivasan, V.; Kostecki, R.; Ceder, G. Lithium Diffusion in Graphitic Carbon. *J. Phys. Chem. Lett.* **2010**, *1* (8), 1176-1180.

(31) Morita, M.; Asai, Y.; Yoshimoto, N.; Ishikawa, M. A Raman spectroscopic study of organic electrolyte solutions based on binary solvent systems of ethylene carbonate with low viscosity solvents which dissolve different lithium salts. *J. Chem. Soc., Faraday Trans.* **1998**, *94*, 3451-3456.

(32) Borodin, O.; Smith, G. D. LiTFSI Structure and Transport in Ethylene Carbonate from Molecular Dynamic Simulations. *J. Phys. Chem. B* **2006**, *110* (10), 4971-4977.

(33) Xu, K. Nonaqueous Liquid Electrolytes for Lithium-Based Rechargeable Batteries. *Chem. Rev.* **2004**, *104* (10), 4303-4418.

(34) Di Lecce, D.; Marangon, V.; Jung, H.-G.; Tominaga, Y.; Greenbaum, S.; Hassoun, J. Glyme-based electrolytes: suitable solutions for next-generation lithium batteries. *Green Chem.* **2022**, *24* (3), 1021-1048.

(35) Peled, E.; Menachem, C.; Bar-Tow, D.; Melman, A. Improved Graphite Anode for Lithium-Ion Batteries Chemically: Bonded Solid Electrolyte Interface and Nanochannel Formation. *J. Electrochem. Soc.* **1996**, *143* (1), L4-L7.

(36) Ein-Eli, Y.; Koch, V. R. Chemical oxidation: a route to enhanced capacity in Li-ion graphite anodes. *J. Electrochem. Soc* **1997**, *144* (9), 2968-2973.

(37) Mogi, R.; Inaba, M.; Jeong, S.-K.; Iriyama, Y.; Abe, T.; Ogumi, Z. Effects of Some Organic Additives on Lithium Deposition in Propylene Carbonate. *J. Electrochem. Soc.* **2002**, *149*.

(38) Profatilova, I. A.; Kim, S.-S.; Choi, N.-S. Enhanced thermal properties of the solid electrolyte interphase formed on graphite in an electrolyte with fluoroethylene carbonate. *Electrochim. Acta* **2009**, *54* (19), 4445-4450.

(39) Xiao, Q.; Gu, M.; Yang, H.; Li, B.; Zhang, C.; Liu, Y.; Liu, F.; Dai, F.; Yang, L.; Liu, Z.; et al. Inward lithium-ion breathing of hierarchically porous silicon anodes. *Nat. Commun* **2015**, *6*, 8844, From NLM PubMed-not-MEDLINE.

(40) Xiao, Z.; Wang, C.; Song, L.; Zheng, Y.; Long, T. Research progress of nano-silicon-based materials and silicon-carbon composite anode materials for lithium-ion batteries. *J Solid State Electrochem.* **2022**, *26* (5), 1125-1136.

(41) *Batteries - Vehicles Technologies Office*. https://www.energy.gov/eere/vehicles/batteries (accessed 2023.

(42) *Battery500: Progress Update*. 2020. https://www.energy.gov/eere/articles/battery500-progress-update (accessed.

(43) Xue, W.; Miao, L.; Qie, L.; Wang, C.; Li, S.; Wang, J.; Li, J. Gravimetric and volumetric energy densities of lithium-sulfur batteries. *Curr. Opin. Electrochem.* **2017**, *6* (1), 92-99.

(44) Cao, W.; Zhang, J.; Li, H. Batteries with high theoretical energy densities. *Energy Storage Mater.* **2020**, *26*, 46-55.

(45) Nitta, N.; Yushin, G. High-Capacity Anode Materials for Lithium-Ion Batteries: Choice of Elements and Structures for Active Particles. *Part Part Syst Charact.* **2014**, *31* (3), 317-336.

(46) Wu, F.; Yuan, Y.-X.; Cheng, X.-B.; Bai, Y.; Li, Y.; Wu, C.; Zhang, Q. Perspectives for restraining harsh lithium dendrite growth: Towards robust lithium metal anodes. *Energy Stor.Mater.* **2018**, *15*, 148-170.

(47) Zheng, G.; Lee, S. W.; Liang, Z.; Lee, H. W.; Yan, K.; Yao, H.; Wang, H.; Li, W.; Chu, S.; Cui, Y. Interconnected hollow carbon nanospheres for stable lithium metal anodes. *Nat Nanotechnol* **2014**, *9* (8), 618-623.

(48) Kozen, A. C.; Lin, C.-F.; Pearse, A. J.; Schroder, M. A.; Han, X.; Hu, L.; Lee, S.-B.; Rubloff, G. W.; Moked, M. Next-Generation Lithium Metal Anode Engineering *via* Atomic Layer Deposition. *ACS Nano* **2015**, *9* (6), 5884-5892.

(49) Zhu, B.; Jin, Y.; Hu, X.; Zheng, Q.; Zhang, S.; Wang, Q.; Zhu, J. Poly(dimethylsiloxane) Thin Film as a Stable Interfacial Layer for High-Performance Lithium-Metal Battery Anodes. *J. Adv. Mater.* **2017**, *29* (2), From NLM PubMed-not-MEDLINE.

(50) Suo, L.; Hu, Y. S.; Li, H.; Armand, M.; Chen, L. A new class of Solvent-in-Salt electrolyte for high-energy rechargeable metallic lithium batteries. *Nat. Commun* **2013**, *4*, 1481, From NLM PubMed-not-MEDLINE.

(51) Lu, Y.; Tu, Z.; Archer, L. A. Stable lithium electrodeposition in liquid and nanoporous solid electrolytes. *Nat. Mater* **2014**, *13* (10), 961-969, From NLM Medline.

(52) Xia, S.; Wu, X.; Zhang, Z.; Cui, Y.; Liu, W. Practical Challenges and Future Perspectives of All-Solid-State Lithium-Metal Batteries. *Chem.* **2019**, *5* (4), 753-785.

(53) Marbella, L. E.; Evans, M. L.; Groh, M. F.; Nelson, J.; Griffith, K. J.; Morris, A. J.; Grey, C. P. Sodiation and Desodiation via Helical Phosphorus Intermediates in High-Capacity Anodes for Sodium-Ion Batteries. *J. Am. Chem. Soc.* **2018**, *140* (25), 7994-8004.

(54) Greenwood, N. N.; Earnshaw, A. *Chemistry of the Elements*; Elsevier Limited, Oxford, 2016.

(55) Kim, S.; Cui, J.; Dravid, V. P.; He, K. Orientation-Dependent Intercalation Channels for Lithium and Sodium in Black Phosphorus. *Adv. Mater.* **2019**, *31* (46), e1904623, From NLM PubMed-not-MEDLINE.

(56) Zaug, J. M.; Soper, A. K.; Clark, S. M. Pressure-dependent structures of amorphous red phosphorus and the origin of the first sharp diffraction peaks. *Nat. Mater.* **2008**, *7* (11), 890-899.

(57) Wang, R.; Mo, H.; Li, S.; Gong, Y.; He, B.; Wang, H. Influence of Conductive additives on the stability of red phosphorus-carbon anodes for sodium-ion batteries. *Sci. Rep.* **2019**, *9* (1), 946, From NLM PubMed-not-MEDLINE.

(58) Park, C. M.; Sohn, H. J. Black Phosphorus and its Composite for Lithium Rechargeable Batteries. *Adv. Mater.* **2007**, *19* (18), 2465-2468.

(59) Yue, Z.; Gupta, T.; Wang, F.; Chao, L.; Rajesh, K.; Yang, Z.; Koratkar, N. Utilizing a graphene matrix to overcome the intrinsic limitations of red phosphorus as an anode material in lithium-ion batteries. *Carbon* **2018**, *127*, 588-595.

(60) Mal, P.; Breiner, B.; Rissanen, K.; Nitschke, J., R. White phosphorus is air-stable within a self-assembeled tetrahedral capsule. *Science* **2009**, *324*, 1697-1699.

(61) Xia, W.; Zhang, Q.; Xu, F.; Ma, H.; Chen, J.; Qasim, K.; Ge, B.; Zhu, C.; Sun, L. Visualizing the Electrochemical Lithiation/Delithiation Behaviors of Black Phosphorus by in Situ Transmission Electron Microscopy. *J. Phys. Chem . C.* **2016**, *120* (11), 5861-5868.

(62) Jung, S. C.; Han, Y.-K. Thermodynamic and Kinetic Origins of Lithiation-Induced Amorphous-to-Crystalline Phase Transition of Phosphorus. *J. Phys. Chem . C.* **2015**, *119* (22), 12130-12137.

(63) Qian, J.; Qiao, D.; Ai, X.; Cao, Y.; Yang, H. Reversible 3-Li storage reactions of amorphous phosphorus as high capacity and cycling-stable anodes for Li-ion batteries. *Chem Commun (Camb)* **2012**, *48* (71), 8931-8933.

(64) Sun, J.; Zheng, G.; Lee, H. W.; Liu, N.; Wang, H.; Yao, H.; Yang, W.; Cui, Y. Formation of stable phosphorus-carbon bond for enhanced performance in black phosphorus nanoparticle-graphite composite battery anodes. *Nano Lett.* **2014**, *14* (8), 4573-4580.

(65) Huang, S.; Cheong, L. Z.; Wang, D.; Shen, C. Nanostructured Phosphorus Doped Silicon/Graphite Composite as Anode for High-Performance Lithium-Ion Batteries. *ACS Appl. Mater. Interfaces* **2017**, *9* (28), 23672-23678.

(66) Li, P.; Hwang, J. Y.; Sun, Y. K. Nano/Microstructured Silicon-Graphite Composite Anode for High-Energy-Density Li-Ion Battery. *ACS Nano* **2019**, *13* (2), 2624-2633.

(67) Wen, J. C.; Huggins, R. A. Chemical diffusion in intermediate phases in the lithium-silicon system. *J. Solid State Chem.* **1981**, *37* (3), 271-278.

(68) Profatilova, I. A.; Langer, T.; Badillo, J. P.; Schmitz, A.; Orthner, H.; Wiggers, H.; Passerini, S.; Winter, M. Thermally Induced Reactions between Lithiated Nano-Silicon

Electrode and Electrolyte for Lithium-Ion Batteries. *J. Electrochem. Soc.* **2012**, *159* (5), A657-A663.

(69) Liu, X. H.; Zhong, L.; Huang, S.; Mao, S. X.; Huang, J. Y. Size-Dependent Fracture of Silicon Nanoparticles During Lithiation. *ACS Nano* **2012**, *6* (2), 1522-1531.

(70) McDowell, M. T.; Lee, S. W.; Harris, J. T.; Korgel, B. A.; Wang, C.; Nix, W. D.; Cui, Y. In situ TEM of two-phase lithiation of amorphous silicon nanospheres. *Nano Lett* **2013**, *13* (2), 758-764, From NLM PubMed-not-MEDLINE.

(71) Liu, X. H.; Zhong, L.; Huang, S.; Mao, S. X.; Zhu, T.; Huang, J. Y. Size-Dependent Fracture of Silicon Nanoparticles During Lithiation. *ACS Nano* **2012**, *6* (2), 1522-1531.

(72) Chan, C. K.; Peng, H.; Liu, G.; McIlwrath, K.; Zhang, X. F.; Huggins, R. A.; Cui, Y. High-performance lithium battery anodes using silicon nanowires. *Nat. Nanotechnol* **2008**, *3* (1), 31-35, From NLM Medline.

(73) Domi, Y.; Usui, H.; Sugimoto, K.; Sakaguchi, H. Effect of Silicon Crystallite Size on Its Electrochemical Performance for Lithium‐Ion Batteries. *Energy Technol.* **2019**, *7* (5).

(74) Jantke, D.; Bernhard, R.; Hanelt, E.; Buhrmester, T.; Pfeiffer, J.; Haufe, S. Silicon-Dominant Anodes Based on Microscale Silicon Particles under Partial Lithiation with High Capacity and Cycle Stability. *J. Electrochem. Soc* **2019**, *166* (16), A3881-A3885.

(75) Wang, B.; Hu, P.; Aifantis, K. E. Selecting the Degree of Partial Lithiation for Preventing Fracture in Si Micoparticles. *Batteries* **2023**, *9* (6).

(76) Baran, V.; van Wullen, L.; Fassler, T. F. Substitution of Lithium for Magnesium, Zinc, and Aluminum in Li15 Si4 : Crystal Structures, Thermodynamic Properties, as well as (6) Li and (7) Li NMR Spectroscopy of Li15 Si4 and Li15-x Mx Si4 (M=Mg, Zn, and Al). *J. Chem.* **2016**, *22* (19), 6598-6609.

(77) Han, B.; Liao, C.; Dogan, F.; Trask, S. E.; Lapidus, S. H.; Vaughey, J. T.; Key, B. Using Mixed Salt Electrolytes to Stabilize Silicon Anodes for Lithium-Ion Batteries via in Situ Formation of Li-M-Si Ternaries (M = Mg, Zn, Al, Ca). *ACS Appl. Mater. Interfaces* **2019**, *11* (33), 29780-29790.

(78) Vilan, A.; Cahen, D. Chemical Modification of Semiconductor Surfaces for Molecular Electronics. *Chem. Rev.* **2017**, *117* (5), 4624-4666, From NLM PubMed-not-MEDLINE.

(79) Karousis, N.; Tagmatarchis, N.; Tasis, D. Current Progress on the Chemical Modification of Carbon Nanotubes. *Chem. Rev.* **2010**, *110* (9), 5366-5397.

(80) Nierengarten, J.-F. Chemical modification of C60 for materials science applications. *New J Chem* **2004**, *28* (10).

(81) Chakrabarti, M. H.; Low, C. T. J.; Brandon, N. P.; Yufit, V.; Hashim, M. A.; Irfan, M. F.; Akhtar, J.; Ruiz-Trejo, E.; Hussain, M. A. Progress in the electrochemical modification of graphene-based materials and their applications. *Electrochim. Acta* **2013**, *107*, 425-440.

(82) Kooi, S. E.; Schlecht, U.; Burghard, M.; Kern, K. Electrochemical modification of single carbon nanotubes. *Angew. Chem. Int. Ed. Engl.* **2002**, *41* (8), 1353-1355, From NLM PubMed-not-MEDLINE.

(83) Knez, M.; Sumser, M.; Bittner, A. M.; Wege, C.; Jeske, H.; Kooi, S.; Burghard, M.; Kern, K. Electrochemical modification of individual nano-objects. *J. Electroanal. Chem.* **2002**, *522* (1), 70-74.

(84) Mozetic, M. Surface Modification to Improve Properties of Materials. *Materials (Basel)* **2019**, *12* (3), From NLM PubMed-not-MEDLINE.

(85) Kim, S. C.; Huang, W.; Zhang, Z.; Wang, J.; Kim, Y.; Jeong, Y. K.; Oyakhire, S. T.; Yang, Y.; Cui, Y. Graphene coating on silicon anodes enabled by thermal surface modification for high-energy lithium-ion batteries. *MRS Bull.* **2022**, *47* (2), 127-133.

(86) Sun, B.; Skyllas-Kazacos, M. Modification of graphite electrode materials for vanadium redox flow battery application—I. Thermal treatment. *Electrochim.Acta* **1992**, *37* (7), 1253-1260.

(87) Astrova, E. V.; Parfeneva, A. V.; Rumyantsev, A. M.; Ulin, V. P.; Baidakova, M. V.; Nevedomskiy, V. N.; Nashchekin, A. V. The Effect of Thermal Treatment on Properties of Composite Silicon–Carbon Anodes for Lithium-Ion Batteries. *Tech. Phys. Lett.* **2020**, *46* (2), 114-117.

(88) Cheng, J.; Wang, C.; Zou, X.; Liao, L. Recent Advances in Optoelectronic Devices Based on 2D Materials and Their Heterostructures. *Adv. Opt. Mater.* **2018**, *7* (1).

(89) Ostroverkhova, O. Organic Optoelectronic Materials: Mechanisms and Applications. *Chem. Rev.* **2016**, *116* (22), 13279-13412, From NLM PubMed-not-MEDLINE.

(90) Meddeb, H.; Götz‐Köhler, M.; Neugebohrn, N.; Banik, U.; Osterthun, N.; Sergeev, O.; Berends, D.; Lattyak, C.; Gehrke, K.; Vehse, M. Tunable Photovoltaics: Adapting Solar Cell Technologies to Versatile Applications. *Adv. Energy Mater.* **2022**, *12* (28).

(91) Liu, X.; Chen, H.; Tan, S. Overview of high-efficiency organic photovoltaic materials and devices. *Renewable Sustainable Energy Rev.* **2015**, *52*, 1527-1538.

(92) Pei, K. Recent Advances in Molecular Doping of Organic Semiconductors. *Surf. Interfaces* **2022**, *30*, 101887.

(93) Kittel, C. *Introduction to Solid State Physics*; 2005.

(94) Chen, T.; Foo, C.; Edman Tsang, S. C. Interstitial and substitutional light elements in transition metals for heterogeneous catalysis. *Chem. Sci.* **2020**, *12* (2), 517-532, From NLM PubMed-not-MEDLINE.

(95) *1985, University of California: In Memoriam.* https://oac.cdlib.org/view?docId=hb4d5nb20m&brand=oac&chunk.id=meta (accessed.

(96) Woodyard, J. R. Nonlinear Circuit Device Utilizing Germanium. 1950.

(97) Rubin, L.; Poate, J. Ion implantation in silicon technology. *Industrial Physicist* **2003**, *9* (3), 12-15.

(98) Kim, T. H.; Kim, J. H.; Kang, K. Molecular doping principles in organic electronics: fundamentals and recent progress. *Jpn. J. Appl. Phys.* **2023**, *62* (SE).

(99) Lee, H.; Paeng, K.; Kim, I. S. A review of doping modulation in graphene. *Synth. Met.* **2018**, *244*, 36-47.

(100) Kou, X.; Jiang, S.; Park, S. J.; Meng, L. Y. A review: recent advances in preparations and applications of heteroatom-doped carbon quantum dots. *Dalton Trans* **2020**, *49* (21), 6915-6938, From NLM PubMed-not-MEDLINE.

(101) Shenoy, R. U. K.; Rama, A.; Govindan, I.; Naha, A. The purview of doped nanoparticles: Insights into their biomedical applications. *Opennano* **2022**, *8*.

(102) Liu, H.; Liu, Y.; Zhu, D. Chemical doping of graphene. *J. Mater. Chem.* **2011**, *21* (10), 3335-3345.

(103) Zhang, X.; Shao, Z.; Zhang, X.; He, Y.; Jie, J. Surface Charge Transfer Doping of Low-Dimensional Nanostructures toward High-Performance Nanodevices. *Adv Mater* **2016**, *28* (47), 10409-10442, From NLM PubMed-not-MEDLINE.

(104) Shi, X.; Dong, G.; Fang, M.; Wang, F.; Lin, H.; Yen, W.-C.; Chan, K. S.; Chueh, Y.-L.; Ho, J. C. Selective n-type doping in graphene via the aluminum nanoparticle decoration. *J. Mater. Chem. C* **2014**, *2*, 5417-5421.

(105) Parambhath, V. B.; Nagar, R.; Ramaprabhu, S. Effect of nitrogen doping on hydrogen storage capacity of palladium decorated graphene. *Langmuir* **2012**, *28* (20), 7826-7833, From NLM PubMed-not-MEDLINE.

(106) Ortiz-Medina, J.; Wang, Z.; Cruz-Silva, R.; Morelos-Gomez, A.; Wang, F.; Yao, X.; Terrones, M.; Endo, M. Defect Engineering and Surface Functionalization of Nanocarbons for Metal-Free Catalysis. *Adv. Mater.* **2019**, *31* (13), e1805717, From NLM Medline.

(107) Park, Y.; Yoo, J.; Lim, B.; Kwon, W.; Rhee, S. W. Improving the functionality of carbon nanodots: doping and surface functionalization. *J. Mater. Chem A* **2016**, *4* (30), 11582-11603.

(108) Choi, H. C.; Shim, M.; Bangsaruntip, S.; Dai, H. Spontaneous reduction of metal ions on the sidewalls of carbon nanotubes. *J. Am. Chem. Soc.* **2002**, *124* (31), 9058-9059, From NLM.

(109) Kong, L.; Enders, A.; Rahman, T. S.; Dowben, P. A. Molecular adsorption on graphene. *J. Condens. Matter Phys.* **2014**, *26* (44), 443001, From NLM Medline.

(110) Stadie, N. P.; Purewal, J. J.; Ahn, C. C.; Fultz, B. Measurements of hydrogen spillover in platinum doped superactivated carbon. *Langmuir* **2010**, *26* (19), 15481-15485, From NLM PubMed-not-MEDLINE.

(111) Banerjee, S.; Dasgupta, K.; Kumar, A.; Ruz, P.; Vishwanadh, B.; Joshi, J. B.; Sudarsan, V. Comparative evaluation of hydrogen storage behavior of Pd doped carbon nanotubes prepared by wet impregnation and polyol methods. *Int. J. Hydrogen Energy* **2015**, *40* (8), 3268-3276.

(112) Wang, J.; Han, W. Q. A Review of Heteroatom Doped Materials for Advanced Lithium–Sulfur Batteries. *Adv. Funct. Mater.* **2021**, *32* (2).

(113) Long, B.; Zou, Y.; Li, Z.; Ma, Z.; Jiang, W.; Zou, H.; Chen, H. Effect of Phosphorus Doping on Conductivity, Diffusion, and High Rate Capability in Silicon Anode for Lithium-Ion Batteries. *ACS Appl. Energy Mater.* **2020**, *3* (6), 5572-5580.

(114) Ewels, C. P.; Glerup, M. Nitrogen doping in carbon nanotubes. *J. Nanosci. Nanotechnol.* **2005**, *5* (9), 1345-1363, From NLM Medline.

(115) Olesinski, R. W.; Kanani, N.; Abbascian, G. J. The P-Si (Phosphorus-Silicon) System. *Bull. alloy phase diagr.* **1985**, *6*, 130-133.

(116) Olesinski, R. W.; Abbaschian, G. J. The Ge-Si (Germanium-Silicon) system. *Bull. alloy phase diagr.* **1984**, *5*, 180-183.

(117) Trolier-McKinstry, S.; Newnham, R. E. *Materials Engineering: Bonding, Structure, and Structure-Property Relationships*; Cambridge University Press, 2017.

(118) Fahey, P. M.; Griffin, P. B.; Plummer, J. D. Point defects and dopant diffusion in silicon. *Rev. Mod. Phys.* **1989**, *61* (2), 289-384.

(119) Jones, S. W. *Diffusion in Silicon*; 2008.

(120) Fair, R. B.; Tsai, J. C. C. A Quantitative Model for the Diffusion of Phosphorus in Silicon and the Emitter Dip Effect. *J. Electrochem. Soc* **1977**, *124*, 1107-1118.

(121) Gösele, U.; Strunk, H. High-temperature diffusion of phosphorus and boron in silicon via vacancies or via self-interstitials? *Appl. Phys.* **1979**, *20*, 265-273.

(122) Gösele, U. M. Fast Diffusion in Semicondutcors. *Ann. Rev. Mater. Sci* **1988**, *18*, 257-282.

(123) Liu, X.-Y.; Windl, W.; Beardmore, K., M.; Masquelier, M. P. First-principles study of phosphorus diffusion in silicon interstitial- and vaccancy-mediated diffusion mechanisms. *Appl. Phys. Lett.* **2003**, *82*, 1839-1841.

(124) Sze, S. M.; Li, Y.; Ng, K. K. *Physics of Semiconductor Devices*; Wiley, 2021.

(125) Abid, N.; Khan, A. M.; Shujait, S.; Chaudhary, K.; Ikram, M.; Imran, M.; Haider, J.; Khan, M.; Khan, Q.; Maqbool, M. Synthesis of nanomaterials using various top-down and bottom-up approaches, influencing factors, advantages, and disadvantages: A review. *Adv. Colloid Interface Sci.* **2022**, *300*, 102597.

(126) Olatomiwa, A. L.; Adam, T.; Gopinath, S. C. B.; Kolawole, S. Y.; Olayinka, O. H.; Hashim, U. Graphene synthesis, fabrication, characterization based on bottom-up and top-down approaches: An overview. *J. Semicond.* **2022**, *43* (6).

(127) Jia, X.; Khan, W.; Wu, Z.; Choi, J.; Yip, A. C. K. Modern synthesis strategies for hierarchical zeolites: Bottom-up versus top-down strategies. *Advanced Powder Technol.* **2019**, *30* (3), 467-484.

(128) Baig, N.; Kammakakam, I.; Falath, W. Nanomaterials: a review of synthesis methods, properties, recent progress, and challenges. *Mater. Adv.* **2021**, *2* (6), 1821-1871.

(129) Yuda, A. P.; Koraag, P. Y. E.; Ferry, I.; Wasito, H. S.; Sumboja, A. Advances of the top-down synthesis approach for high-performance silicon anodes in Li-ion batteries. *.J . Mater. Chem A* **2021**, *9*, 18906-18926.

(130) Zhang, W.; Yin, J.; Sun, M.; Wang, W.; Chen, C.; Altunkaya, M.; Emwas, A. H.; Han, Y.; Schwingenschlogl, U.; Alshareef, H. N. Direct Pyrolysis of Supermolecules: An Ultrahigh Edge-Nitrogen Doping Strategy of Carbon Anodes for Potassium-Ion Batteries. *Adv Mater* **2020**, *32* (25), e2000732, From NLM PubMed-not-MEDLINE.

(131) Deokar, G.; Jin, J.; Schwingenschlögl, U.; Costa, P. M. F. J. Chemical vapor deposition-grown nitrogen-doped graphene's synthesis, characterization and applications. *NPJ 2D Mater. Appl.* **2022**, *6* (1).

(132) Liu, F.; Li, P.; An, H.; Peng, P.; McLean, B.; Ding, F. Achievements and Challenges of Graphene Chemical Vapor Deposition Growth. *Adv. Funct. Mater.* **2022**, *32* (42).

(133) Yuan, Y.; Chen, Z.; Yu, H.; Zhang, X.; Liu, T.; Xia, M.; Zheng, R.; Shui, M.; Shu, J. Heteroatom-doped carbon-based materials for lithium and sodium ion batteries. *Energy Storage Mater.* **2020**, *32*, 65-90.

(134) Billeter, E.; McGlamery, D.; Aebli, M.; Piveteau, L.; Kovalenko, M. V.; Stadie, N. P. Bulk Phosphorus-Doped Graphitic Carbon. *Chem. Mater.* **2018**, *30* (14), 4580-4589.

(135) McGlamery, D.; McDaniel, C.; Ladd, D. M.; Ha, Y.; Mosquera, M. A.; Mock, M. T.; Stadie, N. P. Precursor Decomposition Compatability as the Key to Halide-Free Synthesis of Metastable BC$_3$. *Submitted* **2023**.

(136) McGlamery, D.; McDaniel, C.; Xu, W.; Stadie, N. P. Hydrogen-Type Binding Sites in Carbonaceous Electrodes for Rapid Lithium Insertion. *ACS Appl Mater Interfaces* **2023**, *15* (33), 39211-39217, From NLM PubMed-not-MEDLINE.

(137) McGlamery, D.; Baker, A. A.; Liu, Y.-S.; Mosquera, M. A.; Stadie, N. P. Phonon Dispersion Relation of Bulk Boron-Doped Graphitic Carbon. *J. Phys. Chem. C* **2020**, *124* (42), 23027-23037.

(138) Terranova, M. L.; Sessa, V.; Rossi, M. The World of Carbon Nanotubes: An Overview of CVD Growth Methodologies. *Chem. Vap. Deposition* **2006**, *12* (6), 315-325.

(139) Cassell, A. M.; Raymakers, J. A.; Kong, J.; Dai, H. Large Scale CVD Synthesis of Single-Walled Carbon Nanotubes. *J. Phys. Chem. B* **1999**, *103* (31), 6484-6492.

(140) Nishihara, H.; Kyotani, T. Zeolite-templated carbons - three-dimensional microporous graphene frameworks. *Chem Commun (Camb)* **2018**, *54* (45), 5648-5673, From NLM PubMed-not-MEDLINE.

(141) Lakshmi, B. B.; CPatrissi, C. J.; Martin, C. R. Sol-gel Template Synthesis of Semiconductor Oxide Micro- and Nanostructures. *Chem. Mater.* **1997**, *9* (11), 2544-2550.

(142) Deng, D.; Pan, X.; Yu, L.; Cui, Y.; Jiang, Y.; Qi, J.; Li, W.-X.; Fu, Q.; Ma, X.; Xue, Q.; et al. Toward N-Doped Graphene via Solvothermal Synthesis. *Chem. Mater.* **2011**, *23* (5), 1188-1193.

(143) Quan, B.; Yu, S. H.; Chung, D. Y.; Jin, A.; Park, J. H.; Sung, Y. E.; Piao, Y. Single source precursor-based solvothermal synthesis of heteroatom-doped graphene and its energy storage and conversion applications. *Sci. Rep.* **2014**, *4*, 5639, From NLM PubMed-not-MEDLINE.

(144) Stolle, A.; Ranu, B. *Ball milling towards green synthesis: applications, projects, challenges*; Royal Society of Chemistry, 2014.

(145) Sigmund, H. Solubilities of Magnesium and Calcium in Silicon. *J. Electrochem. Soc* **1982**, *129* (12), 2809-2812.

(146) Ferrari, A. C.; Robertson, J. Interpretation of Raman Spectra of Disordered and Amorphous Carbon. *Phys. Rev. B* **2000**, *61* (20), 14095-14107.

(147) Vladár, A. E.; Postek, M. T.; Ming, B. On the Sub-Nanometer Resolution of Scanning Electron and Helium Ion Microscopes. *Microscopy Today* **2009**, *17* (2), 6-13, From Cambridge University Press Cambridge Core.

(148) Dahn, J. R. Phase diagram of LixC6. *Phys. Rev. B Condens. Matter* **1991**, *44* (17), 9170-9177.

(149) Elgrishi, N.; Rountree, K. J.; McCarthy, B. D.; Rountree, E. S.; Eisenhart, T. T.; Dempsey, J. L. A Practical Beginner's Guide to Cyclic Voltammetry. *J. Chem. Edu.* **2017**, *95* (2), 197-206.

(150) Bairi, P.; Sardar, K.; Samanta, M.; Chanda, K.; Chattopadhyay, K. K. Nanoporous nitrogen-doped graphitic carbon hollow spheres with enhanced electrochemical properties. *Mater. Chem. Front.* **2021**, *5* (20), 7645-7653.

(151) Kim, Y.; Park, Y.; Choi, A.; Choi, N. S.; Kim, J.; Lee, J.; Ryu, J. H.; Oh, S. M.; Lee, K. T. An amorphous red phosphorus/carbon composite as a promising anode material for sodium ion batteries. *Adv. Mater.* **2013**, *25* (22), 3045-3049.

(152) Wang, Y.; Tian, L.; Yao, Z.; Li, F.; Li, S.; Ye, S. Enhanced reversibility of red phosphorus/active carbon composite as anode for lithium ion batteries. *Electrochim. Acta* **2015**, *163*, 71-76.

(153) Zhu, Y.; Wen, Y.; Fan, X.; Gao, T.; Han, F.; Luo, C.; Liou, S.-C.; Chunsheng, W. Red Phosphorus - Single-Walled Carbon Nanotube Composite as a Superior Anode for Sodium Ion Batteries. *ACS Nano* **2015**, *9*, 3254-3264.

(154) Adams, W. J.; Bartell, L. S. Structure and vibrational assignments for PCl5: An electron diffraction study. *J. Mol. Struct.* **1971**, *8* (1), 23-30.

(155) Singh, N. K.; Oerlemans, S. Chemical Beam Etching Reactions of PCl$_3$ on GaAs(100). *Langmuir* **1999**, *15* (8), 2779-2787.

(156) Shevlyuga, V. M.; Vorontsova, Y. A.; Pavlova, T. V. PBr3 Adsorption and Dissociation on the Si(100) Surface. *J. Phys. Chem . C.* **2023**, *127* (19), 8978-8983.

(157) Kennedy, T. The thermal decomposition of phosphorus iodides. *J. Therm. Anal. Calorim.* **1970**, *2*, 370-386.

(158) Abraham, P.; Bekkaoui, A.; Souliére, V.; Bouix, J.; Monteil, Y. Thermal decomposition studies of group V hydrides. *J. Cryst. Growth* **1991**, *107* (1-4), 26-31.

(159) Goodman, N. B.; Ley, L.; Bullett, D. W. Valence-band structures of phosphorus allotropes. *Phys. Rev. B* **1983**, *27* (12), 7440-7450.

(160) Wu, S.; Hui, K. S.; Hui, K. N. 2D Black Phosphorus: from Preparation to Applications for Electrochemical Energy Storage. *Adv. Sci. (Weinh.)* **2018**, *5* (5), 1700491, From NLM PubMed-not-MEDLINE.

(161) Bridgman, P. W. Further Note on Black Phosphorus. *J. Am. Chem. Soc.* **1915**, *38*, 609-612.

(162) Lange, S.; Schmidt, P.; Nigles, T. Au_3SnP_7@Black Phosphorus: An Easy Access to Black Phosphorus. *Inorg. Chem.* **2007**, *46*, 4028-4035.

(163) Extance, P.; Elliott, S. R. Pressure dependence of the electrical conductivity of amorphous red phosphorus. *Philos. mag., B* **2006**, *43* (3), 469-483.

(164) Song, J.; Yu, Z.; Gordin, M. L.; Hu, S.; Yi, R.; Tang, D.; Walter, T.; Regula, M.; Choi, D.; Li, X.; et al. Chemically bonded phosphorus/graphene hybrid as a high performance anode for sodium-ion batteries. *Nano Lett.* **2014**, *14* (11), 6329-6335.

(165) Yuan, D.; Cheng, J.; Qu, G.; Li, X.; Ni, W.; Wang, B.; Liu, H. Amorphous red phosphorous embedded in carbon nanotubes scaffold as promising anode materials for lithium-ion batteries. *J. Power Sources* **2016**, *301*, 131-137.

(166) Zhang, S.; Liu, C.; Wang, H.; Wang, H.; Sun, J.; Zhang, Y.; Han, X.; Cao, Y.; Liu, S.; Sun, J. A Covalent P-C Bond Stabilizes Red Phosphorus in an Engineered Carbon Host for High-Performance Lithium-Ion Battery Anodes. *ACS Nano* **2021**, *15* (2), 3365-3375.

(167) Sun, L.; Zhang, Y.; Zhang, D.; Zhang, Y. Amorphous red phosphorus nanosheets anchored on graphene layers as high performance anodes for lithium ion batteries. *Nanoscale* **2017**, *9* (46), 18552-18560.

(168) Liu, H.; Zhang, S.; Zhu, Q.; Cao, B.; Zhang, P.; Sun, N.; Xu, B.; Wu, F.; Chen, R. Fluffy carbon-coated red phosphorus as a highly stable and high-rate anode for lithium-ion batteries. *Mater. Chem.* **2019**, *7* (18), 11205-11213.

(169) Sun, L.; Zhang, Y.; Zhang, D.; Liu, J.; Zhang, Y. Amorphous red phosphorus anchored on carbon nanotubes as high performance electrodes for lithium ion batteries. *Nano Res.* **2018**, *11* (5), 2733-2745.

(170) Simon, A.; Borrmann, H.; Horakh, J. On the Polyorphism of White Phosphorus. *Chem. Ber.* **1997**, *130*, 1235-1240.

(171) Hart, M.; White, E. R.; Chen, J.; McGilvery, C. M.; Pickard, C. J.; Michaelides, A.; Sella, A.; Shaffer, M. S. P.; Salzmann, C. G. Encapsulation and Polymerization of White Phosphorus Inside Single-Wall Carbon Nanotubes. *Angew. Chem. Int. Ed. Engl.* **2017**, *56* (28), 8144-8148, From NLM PubMed-not-MEDLINE.

(172) Massiot, D.; Fayon, F.; Capron, M.; King, I.; Le Calvé, S.; Alonso, B.; Durand, J.-O.; Bujoli, B.; Gan, Z.; Hoatson, G. Modelling one- and two-dimensional solid-state NMR spectra. *Magn. Reson. Chem.* **2002**, *40* (1), 70-76.

(173) Yu, H. S.; He, X.; Li, S. L.; Truhlar, D. G. MN15: A Kohn-Sham global-hybrid exchange-correlation density functional with broad accuracy for multi-reference and single-reference systems and noncovalent interactions. *Chem. Sci.* **2016**, *7* (8), 5032-5051.

(174) Weigend, F. Accurate Coulomb-fitting basis sets for H to Rn. *Phys. Chem. Chem. Phys.* **2006**, *8* (9), 1057-1065.

(175) Hyatt, I. F. D.; Dave, L.; David, N.; Kaur, K.; Medard, M.; Mowdawalla, C. Hypervalent iodine reactions utilized in carbon-carbon bond formations. *Org. Biomol. Chem.* **2019**, *17* (34), 7822-7848, From NLM PubMed-not-MEDLINE.

(176) Nagamine, S.; Tanaka, A.; Ishimaru, S.; Ohshima, M. Fabrication of carbon‐core/TiO2‐sheath nanofibers from poly (vinyl alcohol)/TiO2 nanofibers by iodine‐vapor treatment and carbonization: effect of carbonization temperature. *Asia-Pac. J. Chem. Eng.* **2012**, *8* (2), 278-282.

(177) Olego, D. J.; Baumann, J. A.; Kuck, M. A.; Schachter, R.; Michel, C. G.; Raccah, P. M. The Microscopic Structure of Bulk Amorphous Red Phosphorus - a Raman-Scattering Investigation. *Solid State Commun.* **1984**, *52* (3), 311-314.

(178) Yu, Z.; Song, J.; Gordin, M. L.; Yi, R.; Tang, D.; Wang, D. Phosphorus-Graphene Nanosheet Hybrids as Lithium-Ion Anode with Exceptional High-Temperature Cycling Stability. *Adv. Sci. (Weinh.)* **2015**, *2* (1-2), 1400020.

(179) Zhang, Y.; Zhang, J.; Su, D. S. Substitutional doping of carbon nanotubes with heteroatoms and their chemical applications. *ChemSusChem* **2014**, *7* (5), 1240-1250, From NLM Medline.

(180) Davidson, J. M.; Gates, L. O.; Nightingale, R. E. Radiation-Damage Effects in Borated Graphite. *Nucl Sci Eng.* **2018**, *26* (1), 90-98.

(181) Yi, J. Y.; Bernholc, J. Atomic structure and doping of microtubules. *Phys. Rev. B Condens.* **1993**, *47* (3), 1708-1711.

(182) Xia, Y.; Mokaya, R.; Walker, G. S.; Zhu, Y. Superior CO2 Adsorption Capacity on N-doped, High-Surface-Area, Microporous Carbons Templated from Zeolite. *Advanced Energy Materials* **2011**, *1* (4), 678-683.

(183) Chen, J.; Yang, J.; Hu, G.; Hu, X.; Li, Z.; Shen, S.; Radosz, M.; Fan, M. Enhanced CO2 Capture Capacity of Nitrogen-Doped Biomass-Derived Porous Carbons. *ACS Sustain.Chem. Eng.* **2016**, *4* (3), 1439-1445.

(184) Denis, P. A. Methane adsorption inside and outside pristine and N-doped single wall carbon nanotubes. *Chem. Phys.* **2008**, *353* (1-3), 79-86.

(185) Adeniran, B.; Mokaya, R. Is N-Doping in Porous Carbons Beneficial for CO2 Storage? Experimental Demonstration of the Relative Effects of Pore Size and N-Doping. *Chem. Mater* **2016**, *28* (3), 994-1001.

(186) Wang, L.; Sofer, Z.; Pumera, M. Will Any Crap We Put into Graphene Increase Its Electrocatalytic Effect? *ACS Nano* **2020**, *14* (1), 21-25, From NLM PubMed-not-MEDLINE.

(187) Matthews, P. D.; King, T. C.; Glass, H.; Magusin, P. C. M. M.; Tustin, G. J.; Brown, P. A. C.; Cormack, J. A.; García-Rodríguez, R.; Leskes, M.; Dutton, S. E.; et al. Synthesis and extensive characterisation of phosphorus doped graphite. *RSC Advances* **2016**, *6* (67), 62140-62145.

(188) Lo, R.; Manna, D.; Hobza, P. P-Doped graphene-C60 nanocomposite: a donor-acceptor complex with a P-C dative bond. *Chem Commun (Camb)* **2022**, *58* (7), 1045-1048.

(189) Liu, Z. W.; Peng, F.; Wang, H. J.; Yu, H.; Zheng, W. X.; Yang, J. Phosphorus-doped graphite layers with high electrocatalytic activity for the O2 reduction in an alkaline medium. *Angew Chem Int Ed Engl* **2011**, *50* (14), 3257-3261, From NLM Medline.

(190) Shimoyama, I.; Hakoda, T.; Shimada, A.; Baba, Y. Influence of configuration at dopant sites on catalytic activity of phosphorus-doped graphite. *Carbon* **2015**, *81*, 260-271.

(191) Ullah, S.; Liu, Y.; Hasan, M.; Zeng, W.; Shi, Q.; Yang, X.; Fu, L.; Ta, H. Q.; Lian, X.; Sun, J.; et al. Direct synthesis of large-area Al-doped graphene by chemical vapor deposition: Advancing the substitutionally doped graphene family. *Nano Res.* **2021**, *15* (2), 1310-1318.

(192) Huang, Y.; Ouyang, Q.; Zhang, D.; Zhu, J.; Li, R.; Yu, H. Carbon Materials Reinforced Aluminum Composites: A Review. *ACTA METALL SIN-ENGL* **2014**, *27* (5), 775-786.

(193) Li, S.-H.; Chao, C.-G. Effects of carbon fiber/Al interface on mechanical properties of carbon-fiber-reinforced aluminum-matrix composites. *Metall Mater. Trans. A* **2004**, *35* (7), 2153-2160.

(194) Bakshi, S. R.; Lahiri, D.; Agarwal, A. Carbon nanotube reinforced metal matrix composites - a review. *Int. Mater. Rev.* **2013**, *55* (1), 41-64.

(195) Leyva Ramos, R.; Ovalle-Turrubiartes, J.; Sanchez-Castillo, M. A. Adsorption of fluoride from aqueous solution on aluminum-impregnated carbon. *Carbon* **1999**, *37* (4), 609-617.

(196) Landry, K.; Kalogeropoulou, S.; Eustathopoulos, N. Wettability of carbon by aluminum and aluminum alloys. *Mater. Sci. Eng. A* **1998**, *254* (1), 99-111.

(197) Etter, T.; Schulz, P.; Weber, M.; Metz, J.; Wimmler, M.; Löffler, J. F.; Uggowitzer, P. J. Aluminium carbide formation in interpenetrating graphite/aluminium composites. *Mater. Sci. Eng. A* **2007**, *448* (1), 1-6.

(198) Vidal-Sétif, M. H.; Lancin, M.; Marhic, C.; Valle, R.; Raviart, J. L.; Daux, J. C.; Rabinovitch, M. On the role of brittle interfacial phases on the mechanical properties of carbon fibre reinforced Al-based matrix composites. *Mater. Sci. Eng. A* **1999**, *272* (2), 321-333.

(199) Nairat, M.; Talla, J. A. Electronic Properties of Aluminum Doped Carbon Nanotubes with Stone Wales Defects: Density Functional Theory. *Solid State Phys.* **2019**, *61* (10), 1896-1903.

(200) Wang, R.; Zhang, D.; Sun, W.; Han, Z.; Liu, C. A novel aluminum-doped carbon nanotubes sensor for carbon monoxide. *J. Mol. Struct.* **2007**, *806* (1), 93-97.

(201) Ao, Z. M.; Tan, T. T.; Li, S.; Jiang, Q. Molecular hydrogen storage in Al-doped bulk graphite with wider layer distances. *Solid State Commun.* **2009**, *149* (33), 1363-1367.

(202) Jeon, T.; Lee, S.; Jung, S. C. Boron-, nitrogen-, aluminum-, and phosphorus-doped graphite electrodes for non-lithium ion batteries. *Curr. Appl. Phys.* **2020**, *20* (8), 988-993.

(203) Shokuhi Rad, A.; Jouibary, Y. M.; Foukolaei, V. P.; Binaeian, E. Study on the structure and electronic property of adsorbed guanine on aluminum doped graphene: First principles calculations. *Curr. Appl. Phys.* **2016**, *16* (5), 527-533.

(204) Ao, Z. M.; Yang, J.; Li, S.; Jiang, Q. Enhancement of CO detection in Al doped graphene. *Chem. Phys. Lett.* **2008**, *461* (4), 276-279.

(205) Ao, Z. M.; Jiang, Q.; Zhang, R. Q.; Tan, T. T.; Li, S. Al doped graphene: A promising material for hydrogen storage at room temperature. *J. Appl. Phys.* **2009**, *105* (7).

(206) Zhao, W.; Meng, Q. Y. Adsorption of Methane on Pristine and Al-Doped Graphene: A Comparative Study via First-Principles Calculation. *Adv Mat Res* **2012**, *602-604*, 870-873.

(207) Shokuhi Rad, A.; Pouralijan Foukolaei, V. Density functional study of Al-doped graphene nanostructure towards adsorption of CO, CO2 and H2O. *Synth. Met.* **2015**, *210*, 171-178.

(208) Varghese, S. S.; Swaminathan, S.; Singh, K. K.; Mittal, V. Ab initio study on gas sensing properties of group III (B, Al and Ga) doped graphene. *Comput. Condens. Matter* **2016**, *9*, 40-55.

(209) Tian, Y. H.; Hu, S.; Sheng, X.; Duan, Y.; Jakowski, J.; Sumpter, B. G.; Huang, J. Non-Transition-Metal Catalytic System for N(2) Reduction to NH(3): A Density Functional Theory Study of Al-Doped Graphene. *J. Phys. Chem. Lett.* **2018**, *9* (3), 570-576, From NLM PubMed-not-MEDLINE.

(210) Shahabi, D.; Tavakol, H. A DFT study on the catalytic ability of aluminum doped graphene for the initial steps of the conversion of methanol to gasoline. *Comput Theor Chem.* **2018**, *1127*, 8-15.

(211) Gokcen, N. A.; Oden, L. L. Phase equilibria in aluminum-carbon system at high temperatures. *Ber. Bunsenges. Phys. Chem.* **2010**, *102* (9), 1178-1180.

(212) Stadie, N. P.; Billeter, E.; Piveteau, L.; Kravchyk, K. V.; Döbeli, M.; Kovalenko, M. V. Direct Synthesis of Bulk Boron-Doped Graphitic Carbon. *Chem. Mater.* **2017**, *29* (7), 3211-3218.

(213) McGlamery, D.; McDaniel, C.; Ladd, D. M.; Mosquera, M. A.; Mock, M. T.; Stadie, N. P. Precursor Decomposition Compatability as the Key to the Halide-Free Synthesis of Metastable BC_3. *(submitted)* **2023**.

(214) Penner-Hahn, J. E. X-ray absorption spectroscopy in coordination chemistry. *Coord. Chem. Rev.* **1999**, *190-192*, 1101-1123.

(215) Schneider, H.; Schreuer, J.; Hildmann, B. Structure and properties of mullite—A review. *Journal of the European Ceramic Society* **2008**, *28* (2), 329-344.

(216) Ihan A. Aksay, D. M. D., Mehmet Sarikaya. Mullite for Structural, Electronic, and Optical Applications. *J. Am. Ceram. Soc.* **1991**, *74* (10), 15.

(217) Andrini, L.; Gauna, M. R.; Conconi, M. S.; Suarez, G.; Requejo, F. G.; Aglietti, E. F.; Rendtorff, N. M. Extended and local structural description of a kaolinitic clay, its fired ceramics and intermediates: An XRD and XANES analysis. *Appl. Clay. Sci.* **2016**, *124-125*, 39-45.

(218) Küper, G.; Peitz, B.; Winter, I.; Hormes, J.; Schneider, H.; Schmücker, M.; Voll, D.; Hoffbauer, W. Aluminum K-Edge Absorption (XANES) Studies of Noncrystalline Mullite Precursors. *J. Am. Ceram. Soc.* **2005**, *79* (3), 813-816.

(219) Omegna, A.; Prins, R.; van Bokhoven, J. A. Effect of Temperature on Aluminum Coordination in Zeolites H−Y and H−USY and Amorphous Silica−Alumina: An in Situ Al K Edge XANES Study. *J. Phys. Chem. B* **2005**, *109* (19), 9280-9283.

(220) Altman, A. B.; Pemmaraju, C. D.; Alayoglu, S.; Arnold, J.; Booth, C. H.; Braun, A.; Bunker, C. E.; Herve, A.; Minasian, S. G.; Prendergast, D.; et al. Chemical and Morphological Inhomogeneity of Aluminum Metal and Oxides from Soft X-ray Spectromicroscopy. *Inorg. Chem.* **2017**, *56* (10), 5710-5719.

(221) Squire, D. W. Mechanistic studies of the decomposition of trimethylaluminum on heated surfaces. *J. Vac. Sci. Technol.* **1985**, *3* (5).

(222) Zhang, Z.; Pan, Y.; Yang, J.; Jiang, Z.; Fang, H. Experimental study of trimethyl aluminum decomposition. *J. Cryst. Growth* **2017**, *473*, 6-10.

(223) Liu, N.; Huo, K.; McDowell, M. T.; Zhao, J.; Cui, Y. Rice husks as a sustainable source of nanostructured silicon for high performance Li-ion battery anodes. *Sci. Rep.* **2013**, *3*, 1919.

(224) Peng, K.; Jie, J.; Zhang, W.; Lee, S.-T. Silicon nanowires for rechargeable lithium-ion battery anodes. *Appl. Phys. Lett.* **2008**, *93* (3).

(225) Xu, Y.; Yin, G.; Ma, Y.; Zuo, P.; Cheng, X. Nanosized core/shell silicon@carbon anode material for lithium ion batteries with polyvinylidene fluoride as carbon source. *J. Mater. Chem.* **2010**, *20* (16).

(226) Yang, G.; Frisco, S.; Tao, R.; Philip, N.; Bennett, T. H.; Stetson, C.; Zhang, J.-G.; Han, S.-D.; Teeter, G.; Harvey, S. P.; et al. Robust Solid/Electrolyte Interphase (SEI) Formation on Si Anodes Using Glyme-Based Electrolytes. *ACS Energy Lett.* **2021**, *6* (5), 1684-1693.

(227) Ababtain, K.; Babu, G.; Lin, X.; Rodrigues, M. T.; Gullapalli, H.; Ajayan, P. M.; Grinstaff, M. W.; Arava, L. M. Ionic Liquid-Organic Carbonate Electrolyte Blends To Stabilize Silicon Electrodes for Extending Lithium Ion Battery Operability to 100 degrees C. *ACS Appl. Mater. Interfaces* **2016**, *8* (24), 15242-15249.

(228) Xu, K.; Wang, C. Batteries: Widening voltage windows. *Nat. Energy* **2016**, *1* (10).

(229) Chen, M.; Li, B.; Liu, X.; Zhou, L.; Yao, L.; Zai, J.; Qian, X.; Yu, X. Boron-doped porous Si anode materials with high initial coulombic efficiency and long cycling stability. *J. Mater. Chem. A* **2018**, *6* (7), 3022-3027.

(230) Ren, Y.; Zhou, X.; Tang, J.; Ding, J.; Chen, S.; Zhang, J.; Hu, T.; Yang, X. S.; Wang, X.; Yang, J. Boron-Doped Spherical Hollow-Porous Silicon Local Lattice Expansion toward a High-Performance Lithium-Ion-Battery Anode. *Inorg. Chem.* **2019**, *58* (7), 4592-4599.

(231) Qu, X.; Zhang, X.; Wu, Y.; Hu, J.; Gao, M.; Pan, H.; Liu, Y. An eggshell-structured N-doped silicon composite anode with high anti-pulverization and favorable electronic conductivity. *J. Power Sources* **2019**, *443*.

(232) Domi, Y.; Usui, H.; Shimizu, M.; Kakimoto, Y.; Sakaguchi, H. Effect of Phosphorus-Doping on Electrochemical Performance of Silicon Negative Electrodes in Lithium-Ion Batteries. *ACS Appl. Mater. Interfaces* **2016**, *8* (11), 7125-7132.

(233) Ette, P. M.; Bhargav, P. B.; Ahmed, N.; Chandra, B.; Rayarfrancis, A.; Ramesha, K. Nanocrystalline silicon embedded highly conducting phosphorus doped silicon thin film as high power lithium ion battery anode. *Electrochim. Acta* **2020**, *330*.

(234) Chen, M.; Zhou, Q.; Zai, J.; Iqbal, A.; Tsega, T.; Dong, B.; Liu, X.; Zhang, Y.; Yan, C.; Zhao, L.; et al. High power and stable P-doped yolk-shell structured Si@C anode simultaneously enhancing conductivity and Li+ diffusion kinetics. *Nano Res.* **2020**, *14* (4), 1004-1011.

(235) Tang, F.; Tan, Y.; Jiang, T.; Zhou, Y. Phosphorus-doped silicon nanoparticles as high performance LIB negative electrode. *J. Mater. Sci.* **2022**, *57* (4), 2803-2812.

(236) Ryu, J.; Seo, J. H.; Song, G.; Choi, K.; Hong, D.; Wang, C.; Lee, H.; Lee, J. H.; Park, S. Infinitesimal sulfur fusion yields quasi-metallic bulk silicon for stable and fast energy storage. *Nat. Commun* **2019**, *10* (1), 2351.

(237) Trumbore, F. A. Solid Solubilities of Impurity Elements in Germanium and Silicon. *Bell Syst. Tech. J.* **1959**, *39*, 205-233.

(238) Thurber, W. R.; Mattis, R. L.; Liu, Y. M. Resistivity-Dopant Density Relationship for Boron-Doped Silicon. *J. Electrochem. Soc* **1980**, *127*, 2291-2294.

(239) Spear, W. E.; Le Comber, P. G. Substitutional Doping of Amorphous Silicon. *Solid State Commun.* **1975**, *17* (9), 1193-1196.

(240) Daali, A.; Zhao, C.; Zhou, X.; Yang, Z.; Amine, R.; Liu, Y.; Wilkistar, O.; Xu, G.-L.; Amine, K. Tuning working potential of silicon-phosphorus anode via microstructure control for high-energy lithium-ion batteries. *J. Solid State Electrochem.* **2022**.

(241) Giessen, V.; Vogel, R. About the silicon-phosphorus system. *Z. Met* **1959**, *50*, 274.

(242) Kooi, E. Formation and Composition of Surface Layers and Solubility Limits of Phosphorus During Diffusion in Silicon. *J. Electrochem. Soc.* **1964**, *111* (12), 1383.

(243) Trumbore, F. A. Solid solubilities of impurity elements in germanium and silicon. *Bell Syst. Tech. J.* **1960**, *39* (1), 205-233.

(244) Makintosh, I. M. The Diffusion of Phosphorus in Silicon. *J. Electrochem. Soc.* **1962**, *109*, 392.

(245) McQuhae, K. G.; Brown, A. S. The lattice contraction coeffecient of boron and phosphorus in silicon. *Solid State Electron.* **1972**, *15* (3), 259-264.

(246) Pearson, G. L.; Bardeen, J. Electrical Properties of Pure Silicon and Silicon Alloys Containing Boron and Phosphorus. *Phys. Rev.* **1949**, *75* (5), 865-883.

(247) Kane, S.; Warnat, S.; Ryan, C. Improvements in methods for measuring the volume conductivity of electrically conductive carbon powders. *Advanced Powder Technol.* **2021**, *32* (3), 702-709.

(248) Fuller, C. S.; Ditzenberger, J. A. Diffusion of Boron and Phosphorus into Silicon. *J. Appl. Phys.* **1954**, *25* (11), 1439-1440.

(249) *Handbook of Porus Silicon*, 1 ed.; Canham, L., Ed.; Springer Cham, 2014. DOI: doi.org/10.1007/978-3-319-05744-6.

(250) Cao, L.; Fan, P.; Barnard, E. S.; Brown, A. M.; Brongersma, M. L. Tuning the color of silicon nanostructures. *Nano Lett.* **2010**, *10* (7), 2649-2654.

(251) Meng, C.-Y.; Chen, J.-L.; Lee, S.-C.; Chia, C.-T. Doping effects on the Raman spectra of silicon nanowires. *Phys. Rev. B Condens. Matter* **2006**, *73* (24).

(252) Li, H.; Huang, X.; Chen, L.; Wu, Z.; Liang, Y. A High Capacity Nano-Si Composite Anode Material for Lithium Rechargable Batteries. *Electrochem. Solid-State Lett.* **1999**, *2* (11), 547-549.

(253) Orsini, F.; Du Pasquier, A.; Beaudoin, B.; Tarascon, J. M.; Trentin, M.; Langenhuizen, N.; De Beer, E.; Notten, P. In situ Scanning Electron Microscopy (SEM) observations of interfaces within plastic lithium batteries. *J. Power Sources* **1998**, *76* (1), 19-29.

(254) Cohen, Y. S.; Cohen, Y.; Aurbach, D. Micromorphological Studies of Lithium Electrodes in Alkyl Carbonate Solutions Using in Situ Atomic Force Microscopy. *J. Phys. Chem B* **2000**, *104* (51), 12282-12291.

(255) Long, B. R.; Chan, M. K. Y.; Greeley, J. P.; Gewirth, A. A. Dopant Modulated Li Insertion in Si for Battery Anodes: Theory and Experiment. *J. Phys. Chem . C.* **2011**, *115* (38), 18916-18921.

(256) Arie, A. A.; Lee, J. K. Electrochemical Properties of P-Doped Silicon Thin Film Anodes of Lithium Ion Batteries. *Mater Sci. Forum.* **2013**, *737*, 80-84.

(257) McAlister, A. J.; Murray, J. L. The Al-Si (Aluminum-Silicon) system. *Bull. alloy phase diagr.* **1984**, *5*, 74-84.

(258) Olesinski, R. W.; Abbaschian, G. J. The B-Si (Boron-Silicon) system). *Bull. alloy phase diagr.* **1984**, *5*, 478-484.

(259) Olesinski, R. W.; Abbaschian, G. J. The Si-Zn (Silicon-Zinc) System. *Bull. alloy phase diagr.* **1985**, *6* (6), 545-548.

(260) Jain, A.; Ong, S. P.; Hautier, G.; Chen, W.; Richards, W. D.; Dacek, S.; Cholia, S.; Gunter, D.; Skinner, D.; Ceder, G.; et al. Commentary: The Materials Project: A materials genome approach to accelerating materials innovation. *APL Materials* **2013**, *1* (1).

(261) Wang, Y. L.; Sun, Q. L.; Zhao, Q. Q.; Cao, J. S.; Ye, S. H. Rechargeable lithium/iodine battery with superior high-rate capability by using iodine–carbon composite as cathode. *Energy Environ. Sci.* **2011**, *4* (10).

(262) Lu, K.; Hu, Z.; Ma, J.; Ma, H.; Dai, L.; Zhang, J. A rechargeable iodine-carbon battery that exploits ion intercalation and iodine redox chemistry. *Nat. Commun* **2017**, *8* (1), 527, From NLM PubMed-not-MEDLINE.

(263) Gauthier, M.; Mazouzi, D.; Reyter, D.; Lestriez, B.; Moreau, P.; Guyomard, D.; Roué, L. A low-cost and high performance ball-milled Si-based negative electrode for high-energy Li-ion batteries. *Energy Environ. Sci.* **2013**, *6* (7).

APPENDICIES

APPENDIX A

HETEROATOM-DOPED GRAPHITIC CARBON SYNTHESIS CALCULATION

To determine the mols of reagents for pyrolysis of heteroatom-doped graphitic carbon materials, the evolution of gaseous products inside a sealed quartz ampule must be considered. For safety concerns the chosen maximum pressure is 20 bar. Using the ideal gas law (equation A.1.), the total number of mols of benzene and dopant-containing precursor are tabulated based on known ampule volume (V), maximum allowed pressure (P_{max}) and maximum temperature (T_{max}). Measurable quantities of benzene and the dopant containing precursor are calculated by multiplying the molecular weight (MW = g mol^{-1}) of each precursor by the total number of moles allowed in the reaction (0.002182 or 0.004974 moles for small or large ampules, respectively) and lastly by a ratio factor that accounts for the total gas evolved. Reactions for desired PC_x and AlC_x nominal compositions (where x = 1-8) and ratio factors are shown in Table A.1. Molecular weight and density of all relevant chemical precursors used in the synthesis of phosphorus- or aluminum-doped graphitic carbon are shown in Table A.2.

$$(A.1.) \qquad P_{max}V_{max} = NRT_{max}$$

Table A.1. Phosphorus- and aluminum-doped graphitic carbon reaction schemes.

Nominal Composition	Reaction	Ratio* (C_6H_6)	Ratio* (P or Al precursor)
PC$_x$ reaction schemes			
Precursor: Phosphorus containing halide PX_3 where X = Cl, Br, and I			
PC	$C_6H_6 + 6PX_3 \rightarrow 6PC + 9X_2 + 3H_2$	0.08	0.50
PC$_2$	$2C_6H_6 + 6PX_3 \rightarrow 6PC_2 + 9X_2 + 6H_2$	0.13	0.40
PC$_3$	$C_6H_6 + 2PX_3 \rightarrow 2PC_3 + 3X_2 + 3H_2$	0.17	0.33
PC$_4$	$4C_6H_6 + 6PX_3 \rightarrow 6PC_4 + 9X_2 + 12H_2$	0.19	0.29
PC$_5$	$5C_6H_6 + 6PX_3 \rightarrow 6PC_5 + 9X_2 + 15H_2$	0.21	0.25
PC$_6$	$2C_6H_6 + 2PX_3 \rightarrow 2PC_6 + 3X_2 + 6H_2$	0.22	0.22
PC$_7$	$7C_6H_6 + 6PX_3 \rightarrow 6PC_7 + 9X_2 + 21H_2$	0.23	0.20
PC$_8$	$8C_6H_6 + 6PX_3 \rightarrow 6PC_8 + 9X_2 + 24H_2$	0.24	0.18
AlC$_x$ reaction schemes			
Precursor: Aluminum Trichloride			
AlC	$C_6H_6 + 6AlCl_3 \rightarrow 6AlC + 9Cl_2 + 3H_2$	0.08	0.50
AlC$_2$	$2C_6H_6 + 6AlCl_3 \rightarrow 6AlC_2 + 9Cl_2 + 6H_2$	0.13	0.40
AlC$_3$	$C_6H_6 + 2\,AlCl_3 \rightarrow 2AlC_3 + 3Cl_2 + 3H_2$	0.17	0.33
AlC$_4$	$4C_6H_6 + 6\,AlCl_3 \rightarrow 6AlC_4 + 9Cl_2 + 12H_2$	0.19	0.29
AlC$_5$	$5C_6H_6 + 6\,AlCl_3 \rightarrow 6AlC_5 + 9Cl_2 + 15H_2$	0.21	0.25
AlC$_6$	$2C_6H_6 + 2\,AlCl_3 \rightarrow 2AlC_6 + 3Cl_2 + 6H_2$	0.22	0.22
AlC$_7$	$7C_6H_6 + 6\,AlCl_3 \rightarrow 6AlC_7 + 9Cl_2 + 21H_2$	0.23	0.20
AlC$_8$	$8C_6H_6 + 6P\,AlCl_3 \rightarrow 6AlC_8 + 9Cl_2 + 24H_2$	0.24	0.18
Precursor: Trimethyl Aluminum			
AlC$_3$	$2Al(CH_3)_3 \rightarrow 2AlC_3 + 9H_2$	--	0.22

*Ratio is based on desired moles of reactant dived by total moles gas products evolved.

Table A.2. Molecular weight and density of relevant chemical precursors used in the synthesis of heteroatom-doped graphitic carbon materials.

Precursor	State	Molecular Weight (g mol^{-1})	Density (g mL^{-1})
C_6H_6	Liquid	78.11	0.876
PCl_3	Liquid	137.33	1.57
PBr_3	Liquid	279.69	2.88
PI_3	Solid	411.69	4.18
$AlCl_3$	Solid	133.34	2.40
$Al_2(CH_3)_6$	Liquid	72.09	0.75

APPENDIX B

BINARY SILICON PHASE DIAGRAMS

Table B.1. Eutectic temperature, retrograde temperature, and maximum solubility of dopants in silicon

Dopant	Eutectic Temperature °C	Retrograde Solubility Temperature °C	Maximum Solubility (at%)	Ref
Al	577	~1190	0.016 +/- 0.003	[257]
B	1385	--	3.00	[258]
Mg	947	~1200	0.03	[145]
P	1131 +/-2	1180	2.4	[115]
Zn	419.58	~1350	0.00015	[259]
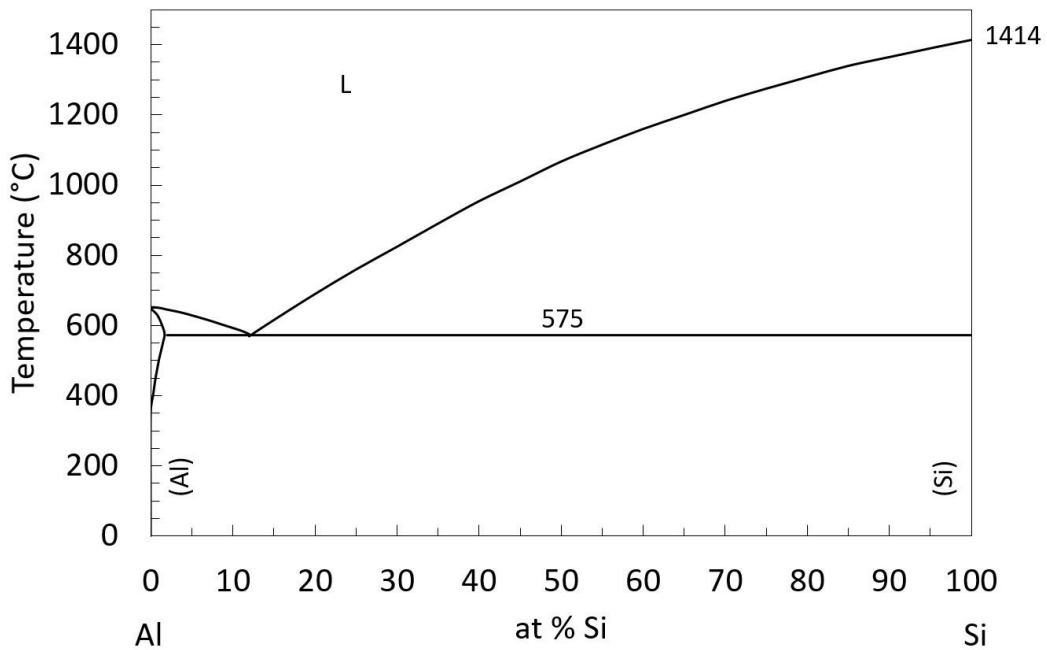
Figure B.1. Aluminum-silicon binary phase diagram. Adapted from reference [257]
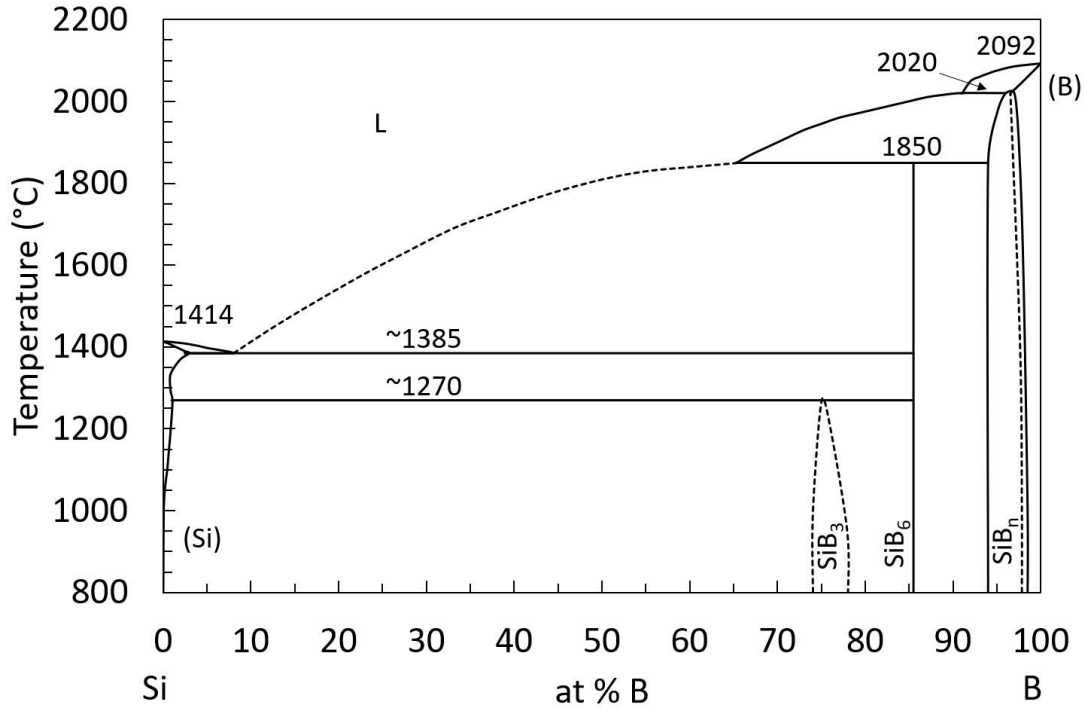
Figure B.2. Boron-Silicon Phase Diagram. Adapted from reference [258]
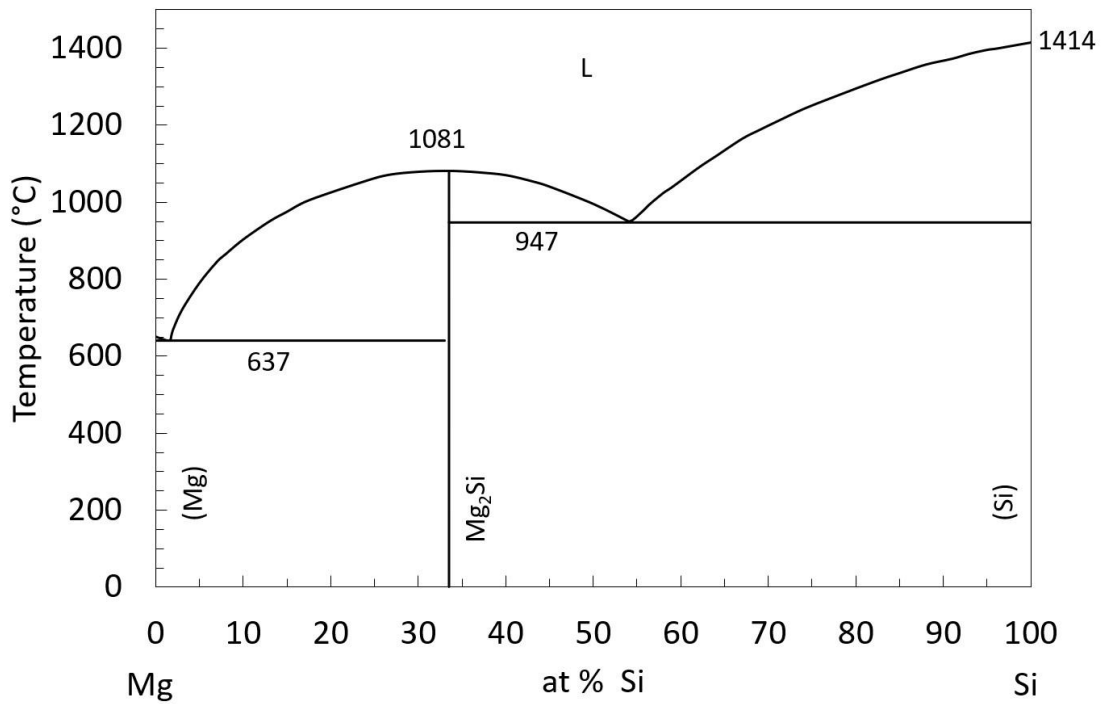
Figure B.3. Magnesium-Silicon Phase Diagram. Adapted from reference [145]
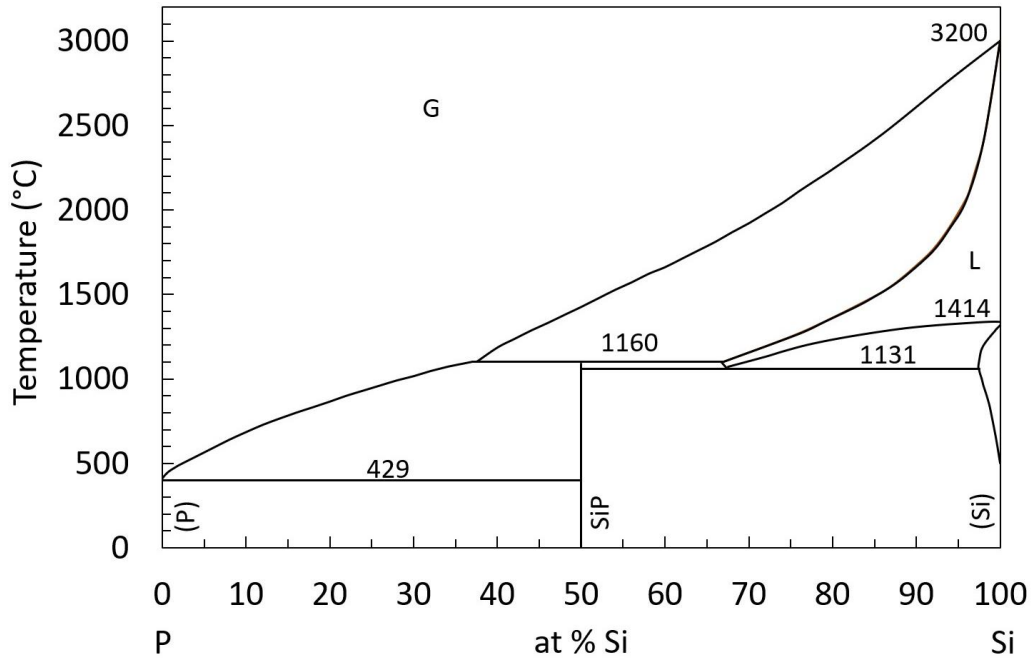
Figure B.4. Phosphorus-Silicon Phase Diagram. Adapted from reference [115]
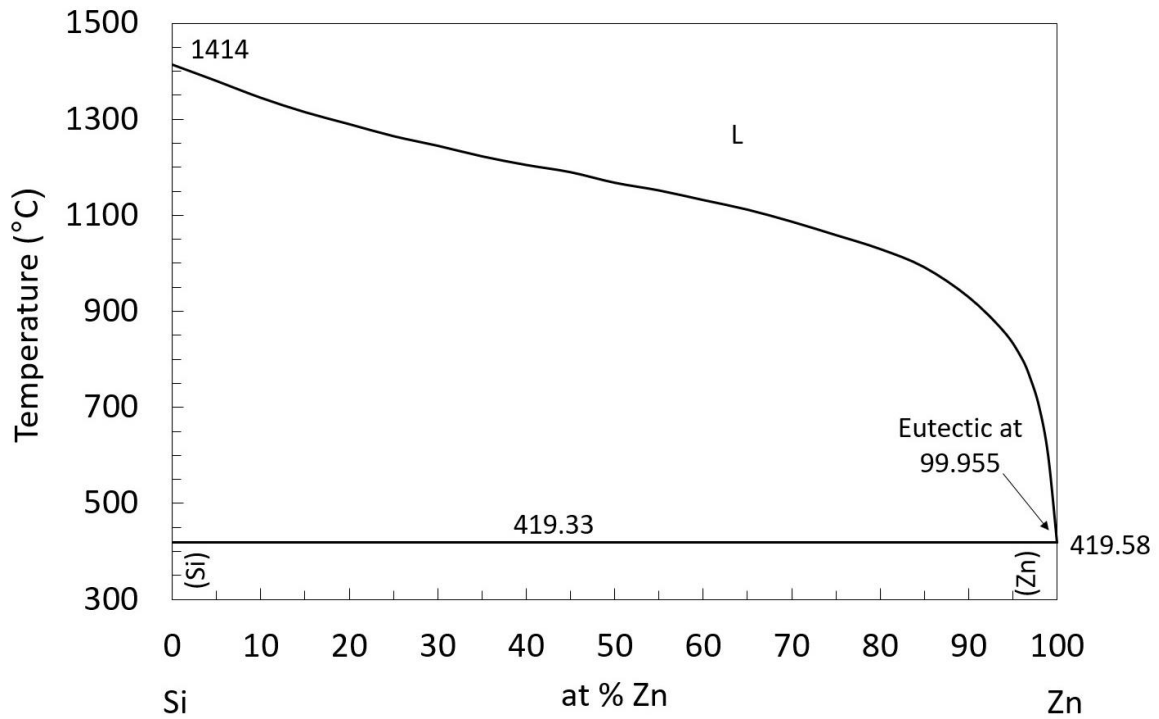
Figure B.5. Zinc-Silicon Phase Diagram. Adapted from reference [259]

APPENDIX C

EXPECTED PHOSPHORUS VOLUME EXPANSION UNDER LITHIATION/SODIATION

The total unit cell volume (V) and number of P atoms per unit cell (N) were determined

for each crystal, according to the references shown in Table C.1. The volume per P atom ($\tilde{V}$) was

then determined by:

$$(C.1.) \quad \tilde{V} = \frac{V}{N}$$

Table C.1. Tabulated volume expansion for phosphorus allotropes when lithiated/sodiated

Phase	Composition	Space Group	Volume per P atom [Å^3 P^{-1}]	Volume Expansion upon Lithiation (%)	Volume Expansion upon Sodiation (%)	Ref*
--	Li_3P	P6$_3$/mmc	59	--	--	ICSD 240861
--	Na_3P	P6$_3$/mmc	93	--	--	ICSD 1771177
RP (Hittorf's)	P	P2/c	23	254	405	MP 568348
RP (Violet)	P	P2/c	22	269	428	ICSD 29273
RP (Fibrous)	P	P-1	22	270	430	ICSD 1771177
BP	P	Cmca	19	308	491	ICSD 23836
WP	P	P-1	26	225	359	ICSD 406793

*MP and ICSD are abbreviations for Materials Project Open Data Base[260] and the Inorganic Crystal Structure Database, respectively.

<u>APPENDIX D</u>

HALIDE TRAPPING IN GRAPHITIC CARBON

Residual halide content in P/C materials is determined by EDX. Figure D.1 shows the X/P (where X = Br, or I) ratio for -PBr$_3$ and -PI$_3$ materials over a range of nominal compositions (P:C, 1:1-1:8). On average, -PI$_3$ materials contain more residual halide than -PBr$_3$ materials, likely owing to the heavier mass of iodine than bromine. At nominal composition P/C-1:1-PI$_3$ the X/P ratio is ~0.8; meaning that for every 1 phosphorus atom incorporated in the P/C structure, nearly 1 iodine atom remains.

To drive off residual iodine a material of high nominal P composition, P/C-1:1-PI$_3$, was subjected to a heat treatment at 150 °C for 2 hours under vacuum (6.5 x 10^{-3} mbar) in an oven (Büchi glass oven B-585). Iodine content was measured before and after heat treatment. Upon introduction into the oven the vacuum initially pumped down to 6.5 x 10^{-3} mbar, at 15 minutes the pressure spiked to (1.1 x 10^{-2} mbar) and then at 25 minutes returned to 6.5 x 10^{-3} mbar. The pressure spike is likely related to the off-gassing of iodine at slightly elevated temperature. The iodine content before and after the heat treatment was 4.26 ± 0.15 at% and 0.35 26 ± 0.11 at%. This experiment demonstrates that halide is likely trapped between graphitic sheets or at the very least a residual surface contaminant. While initially thought to be an undesired byproduct, iodine incorporation into graphitic carbon has merit towards dual ion-intercalation and iodine redox battery chemistries[261, 262], remaining an avenue of future work.
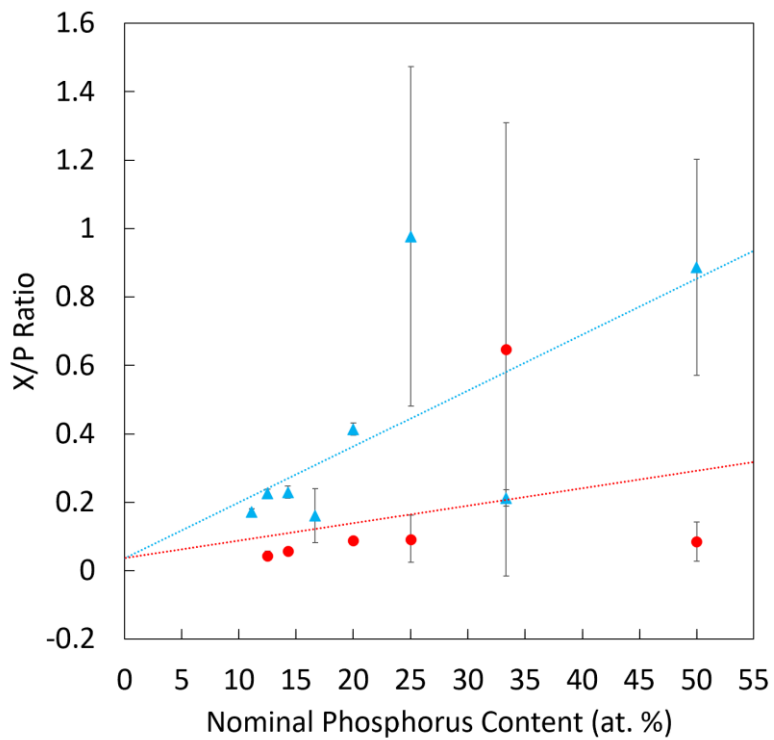
Figure D.1. Residual halide content for PBr_3 (red) and PI_3 (blue) derived P/C materials over a range of nominal phosphorus compositions. Halide is normalized per phosphorus content.

APPENDIX E

TABULATING TOTAL LITHIABLE PHOSPHORUS FROM CYCLIC VOLTAMMETRY

To determine the total lithiable P content in a P/C material, the assumption is made that most of the capacity measured within the limited voltage window (0.25-2.00 V vs. Li/Li$^+$) is attributable to the lithiation of P (as opposed to the graphitic carbon, which primarily lithiates at < 0.25 V). To verify this assumption, a pure carbon control (via the direct pyrolysis of benzene at 800 °C without any P-precursor), with similar underlying graphitic structure as that found in the P/C composite materials, was tested within the same potential window to determine its contribution to the overall capacity in that range. Capacity was determined in each case by integration of the slow-rate (1 mV s^{-1}) cyclic voltammogram (CV) along the anodic branch. The "lithiable P content" (shaded region, Figure E.1) was determined by subtraction of the pure carbon capacity from the P/C capacity. This reflects a minimum estimate of the lithiable P, and hence a positive error bar was assigned by considering the entire capacity of the P/C composite material alone as the maximum estimate of lithiable P.
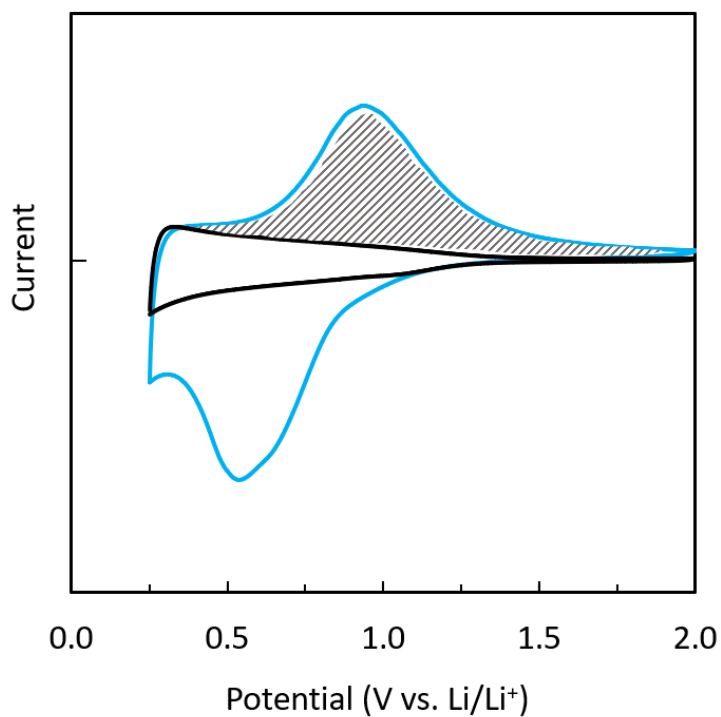
Figure E.1. Schematic depiction of the calculation of total lithiable capacity in P/C composite materials using cyclic voltammetry (CV). The region of interest (attributed to solely to phosphorus capacity) is shaded.

APPENDIX F

EXPECTED THEOERTICAL CAPACITY OF P/C MATERIALS

Between the first and second GCD cycle, P/C materials experience significant capacity fading on the order of several hundred mAh g^{-1}. The question remains whether or not capacity loss is due to SEI formation or irreversible lithiation of phosphorus. Insight can be gained by comparing the tabulated theoretical capacity of P/C materials to the actual measured capacity on the first cycle. In doing so, two assumptions are made; i) the total measured phosphorus content, determined by EDX, is accessible to lithiation (either in the form of WP or RP), and ii) any graphitic carbon within the P/C system undergoes intercalation of lithium (LiC$_6$ stoichiometry).

Theoretical capacity can be determined by equation F.1. which requires knowledge of the number of electrons stored during lithiation (n), Faraday's constant (F = 96,485 C mol^{-1}) and the molecular weight (MW) of respective P/C materials. The corresponding nominal and measured P/C composition, determined by EDX, are shown in Table F.1. Using the measured P/C composition a MW can be determined (neglecting impurities). Expected lithiation reactions and tabulated theoretical capacities are shown in Table 4.4.1.

$$(F.1.) \quad Q = \frac{n \cdot F}{MW}$$

PCl$_3$ and PI$_3$ derived P/C materials have remarkably similar expected theoretical capacities relative to measured capacities on the first cycle (1 A g^{-1}) a strong indication that capacity loss between the first and second cycle is due to irreversible lithiation at phosphorus sites. PBr$_3$ derived materials, however, tell a more complicated story. In the case of P/C-1:3-PBr$_3$ the expected and measured capacities are ~1199 and ~286 mAh g^{-1}. This discrepancy can be attributed to the composite-like nature of this material where bulk RP resides between and around graphitic sheets, potentially blocking lithiation channels.

Table F.1. Expected theoretical capacity and measured capacity of PC_x materials on first cycle at 1 A g^{-1}

P Precursor	Nominal Composition PC_x	P Content (at%)	Measured Composition PC_x	MW of Measured PC_x	Lithiation Reaction	Expected Q mAh g^{-1}	Actual Q mAh g^{-1}
PCl_3	(1:3) PC_3	10.1 ± 4.9	$PC_{9.9}$	139.07	$PC_{9.9} + 4Li^+ + 4e^- \rightarrow Li_3P + LiC_{9.9}$	770	771
	(1:5) PC_5	6.3 ± 2.0	$PC_{15.9}$	211.13	$PC_{15.9} + 5Li^+ + 5e^- \rightarrow Li_3P + Li_2C_{15.9}$	634	604
PBr_3	(1:3) PC_3	28.1 ± 17.5	$PC_{3.5}$	67.01	$PC_{3.5} + 3Li^+ + 3e^- \rightarrow Li_3P + C_{3.5}$	1199	286
	(1:5) PC_5	6.1 ± 3.7	$PC_{16.4}$	223.15	$PC_{16.4} + 5Li^+ + 5e^- \rightarrow Li_3P + Li_2C_{16.5}$	360	552
PI_3	(1:3) PC_3	4.5 ± 2.0	$PC_{22.2}$	295.21	$PC_{22.2} + 6Li^+ + 6e^- \rightarrow Li_3P + Li_3C_{22.2}$	544	461
	(1:5) PC_5	4.7 ± 2.7	$PC_{21.3}$	283.20	$PC_{21.3} + 6Li^+ + 6e^- \rightarrow Li_3P + Li_3C_{21.3}$	567	594

APPENDIX G

DETERMINING REVERSIBLE LITHIATION OF STABILIZED WHITE PHOSPHORUS

P/C-1:5-PCl$_3$ is subjected to CS$_2$ treatment for 24 hours followed by a heat treatment (80 °C) to dissolve out P$_4$ molecules. P/C-1:5-PCl$_3$ was electrochemically tested before and after CS$_2$ treatment and show nearly identical CV and GCD performance (Figure G.1). This implies that either WP stabilized between graphitic sheets is inaccessible to CS$_2$ and not properly dissolved out, or that WP domains are destroyed after the first lithiation cycle yet remain of electrochemical importance.

Differential scanning calorimetry (DSC) is used to determine the presence of WP in P/C-1:5-PCl$_3$ materials pre and post CS$_2$ treatment (Figure G.2). P/C-1:5-PCl$_3$ materials dried at 35 °C and 80 °C both contain an exothermic peak at ~86 and ~77 °C respectively. P/C-1:5-PCl$_3$ dried at elevated temperature (80 °C) has a slightly lower exothermic peak, suggesting P$_4$ is susceptible to degradation/decomposition. DSC of P/C-1:5-PCl$_3$ treated with CS$_2$ and dried at 40 °C shows no presence of a WP exothermic peak, verifying the dissolution of P$_4$ molecules. These findings preliminarily suggest the polymerization of P$_4$ molecules after first cycle lithiation. Future work is needed to determine so.
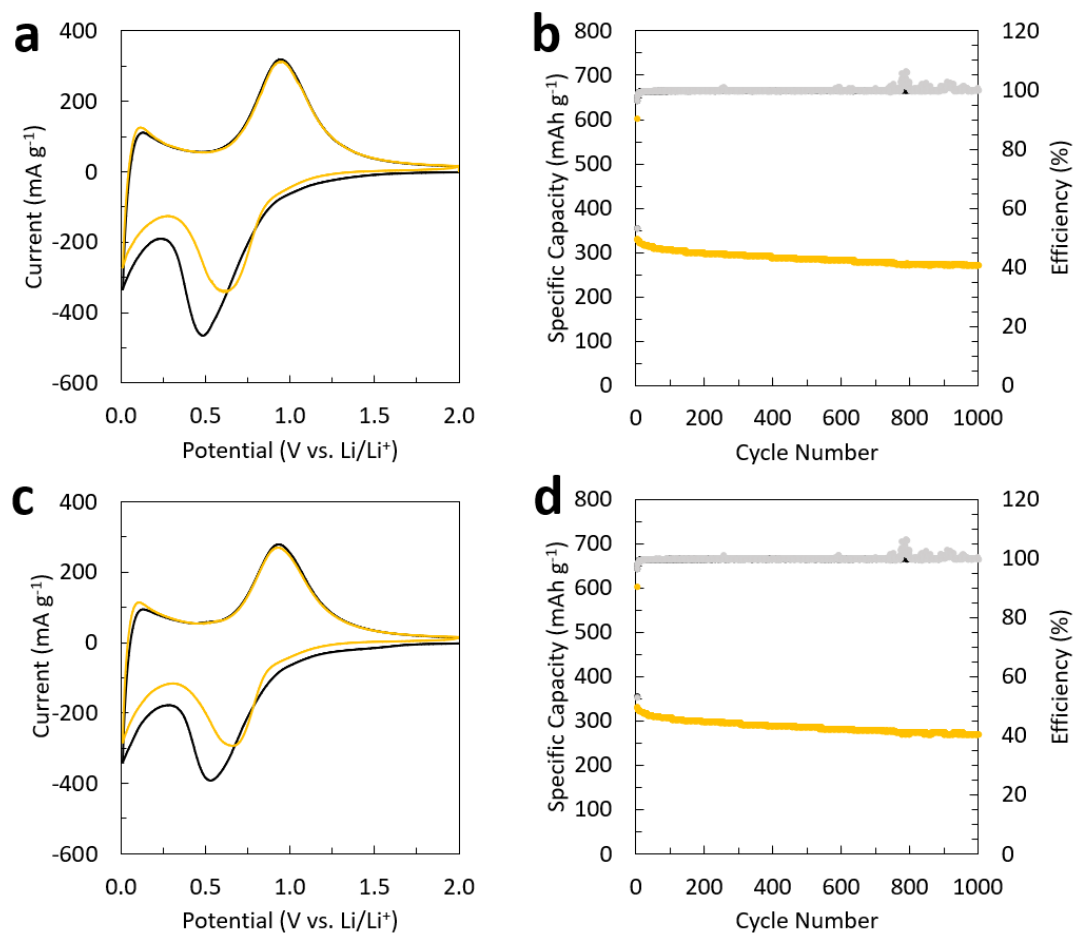
Figure G.1. Electrochemical performance of P/C-1:5-PCl$_3$ before (a-b) and after (c-d) CS$_2$ treatment. CV and GCD are carried out at 0.1 mV s^{-1} and 1 A g^{-1} respectively between 0.01-2.0 V.
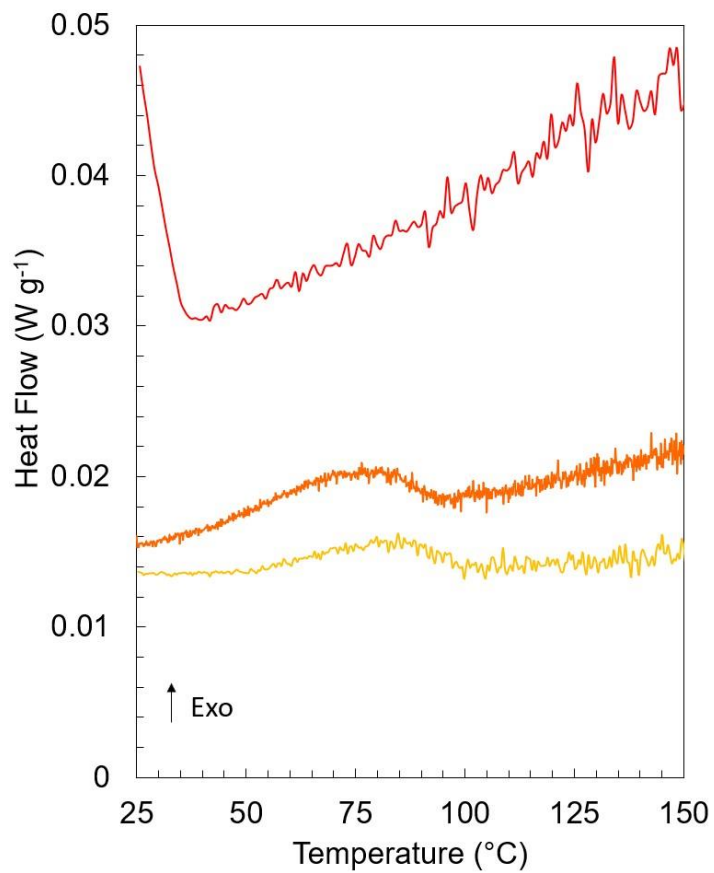
Figure G.2. DSC of CS_2 treated P/C-1:5-PCl_3 (red) and untreated P/C-1:5-PCl_3 dried at 35 °C (yellow) and 80 °C (orange).

APPENDIX H

STRUCTURAL PACKING LIMIT OF WHITE PHOSPHORUS IN GRAPHITE

The relative amount of WP in both P/C-1:3-PCl$_3$ and P/C-1:5-PCl$_3$ is ~15 wt%. It is no coincidence that both materials contain the same amount of WP and can likely be related to a structural packing limit within graphitic sheets. To demonstrate this, two scenarios ae examined; i) maximum possible packing of WP molecules between graphitic sheets and ii) the "true" packing of WP based on PC$_5$-PCl$_3$. We examine this from a purely geometric lens, neglecting repulsive /electronic forces. WP molecules are treated as perfect spheres where the radius is equal to its centroid (1.338 Å). We assume that all measured P is in the form of WP and that WP is stabilized between graphitic sheets.

The diameter of a WP sphere (2.676 Å) is marginally less than the diameter of a 6 membered carbon ring (2.848 Å). In an extreme packing scenario let's assume a WP sphere occupies the space above a 6 membered ring; this gives a stoichiometry of P$_4$C$_6$, or PC$_{1.5}$. We can compare this to P/C-1:5-PCl$_3$ which based on EDX data, has an "measured" composition of PC$_{15.9}$, meaning for every stabilized P$_4$ group, a total of ~64 carbon atoms are occupied. WP molecules do not reach near to the expected *maximum* structural packing limit within graphitic carbon as initially expected. Future work of this work should consider the repulsive forces and energetics of the system.

APPENDIX I

STRATAGIES TO PREVENT FORMATION OF MULLITE

Two approaches to eliminate the formation of mullite byproduct were attempted; i) passivation of quartz ampules, and ii) use of molybdenum packets to isolate chemical precursors from quartz ampule. Above approaches were unsuccessful in preventing the formation of mullite during synthesis.

Quartz ampules were first passivated using a dilute nitric acid (HNO_3) in deionized water. 3.79 mL of 15.8 M HNO_3 was added to 26.7 mL of deionized water. Prepared ampules were filled with dilute HNO_3 for 24 hours. Ampules were rinsed with deionized water and dried at 120 °C. AlC_x was synthesized using the passivated ampules at 1100 °C with a 1 °C min^{-1} ramp rate and 1 hour dwell time. Powder XRD patterns were collected and are shown in Figure I.1. The resulting materials all contain peaks representative of mullite.
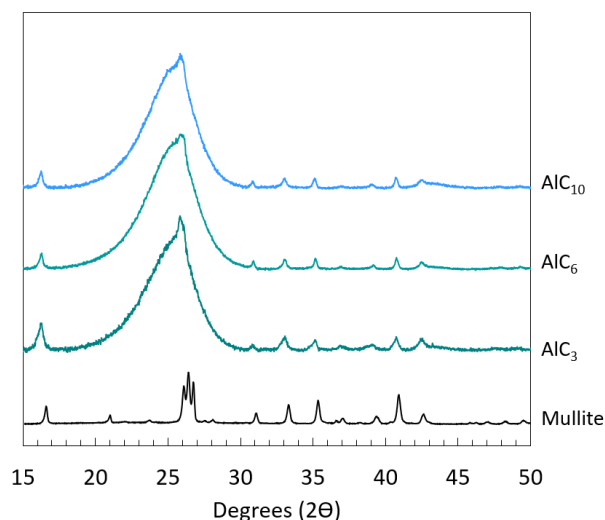
Figure I.1. XRD patterns of AlC_x synthesized in HNO_3 passivated ampules at 1100 °C with a 1 °C min^{-1} ramp rate and 1 hour dwell.

In another attempt to prevent the formation of mullite, synthesis was carried out by placing chemical precursors within a sealed molybdenum packet to minimize aluminum's contact with the quartz ampule (Figure I.2). 1/8-inch diameter cylindrical packets of at least 2 inches in length were

constructed with 0.025 mm thick Mo foil (Sigma Aldrich). Chemical precursors were carefully

sealed within the Mo packets under inert conditions. The Mo packet was placed inside of a quartz

ampule and sealed according to methods described in chapter 5. Upon opening the ampule, all of

the pyrolyzed material was contained inside of the Mo packet. Unexpectedly peaks indicative of

mullite intensify for AlC_x materials synthesized in a Mo packet (Figure I.2). The experiment was

repeated again with the presence of a Mo strip instead of a packet and again a slight increase in

mullite was observed (Figure I.2), indicating that molybdenum acts as a catalyst.
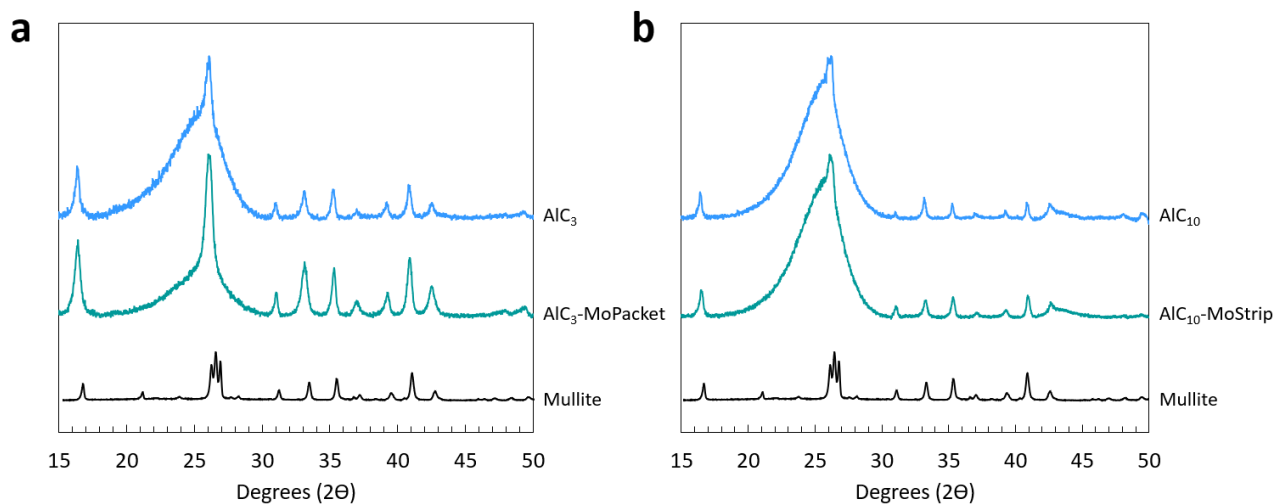
Figure I.2. XRD patterns of a) AlC_3 synthesized with and without Mo packet at 800 °C with 1 °C min^{-1} ramp rate and b) AlC_{10} synthesized with and without a Mo strip at 1100 °C with 1 °C min^{-1} ramp rate.

APPENDIX J

COMMERCIALLY AVAILABLE SILICON POWDERS

Ten different commercially available silicon powders ranging in particle size and purity were characterized to best determine a model material for silicon anodes whereby modest capacity (>500 mAh g^{-1}) is retained over 200 cycles. Silicon powders, respective suppliers, purities, and nominal particle size are shown in Table J.1. XRD patterns and crystallite size of commercially available silicon powders are shown in Figure J.1. The Si(111) reflection for various Si powders is between 28.35 and 28.45 2θ. The Si(111) peak broadness increases relatively as a function of nominal particle size. Using the Scherrer equation the FWHM of the Si(111) reflection is related to crystallite size and is shown in Table J.2.

Three commercial silicon powders of varying size (44 μm, 500 nm and 100 nm) were selected and studied electrochemically to elucidate the effects of particle size on cycling stability (Figure J.2). Small nominal particle size in the case of NP-SA-100 (100 nm nominal particle size) lends to at best modest cycling stability. In contrast MP-SA-44000 (44 μm nominal particle size) suffers severe capacity loss within the first ten cycles. Relative cycling performance can be related to crystallite size (See Table J.2.) where NP-SA-100 and NP-US-500 and MP-SA-44000 have average crystallite sizes of 5, 7, and 22 nm respectively. Large crystallites in MP-SA-44000 likely slows lithium kinetics during (de)lithiation[73, 263] and leads to catastrophic degradation within the first 20 cycles.

Table J.1. Commercially available silicon powders. NPs, MPs, and NWs correspond to nanoparticles, microparticles, and nanowires.

Material ID	Si	Supplier	Purity	Nominal Particle Size (nm)
NP-AA-50	NPs	Alfa Aesar	98%	50
NP-SA-100	NPs	Sigma Aldrich	98%	100
NP-MTI-100	NPs	MTI Corp.	97%	100
NW-US-100	NWs	US Nano	99%	100
NP-US-500	NPs	US Nano	99.99%	500
MP-US-1000	MPs	US Nano	99.99	1000
MP-US-1000/3000	MPs	US Nano	99.9%	1000-3000
MP-Elk-1000/10000	MPs	Elkem	--	1000-10000
MP-SA-44000	MPs	Sigma Aldrich	99%	44000
NREL-macro	Beads	NREL	99.999%	macro
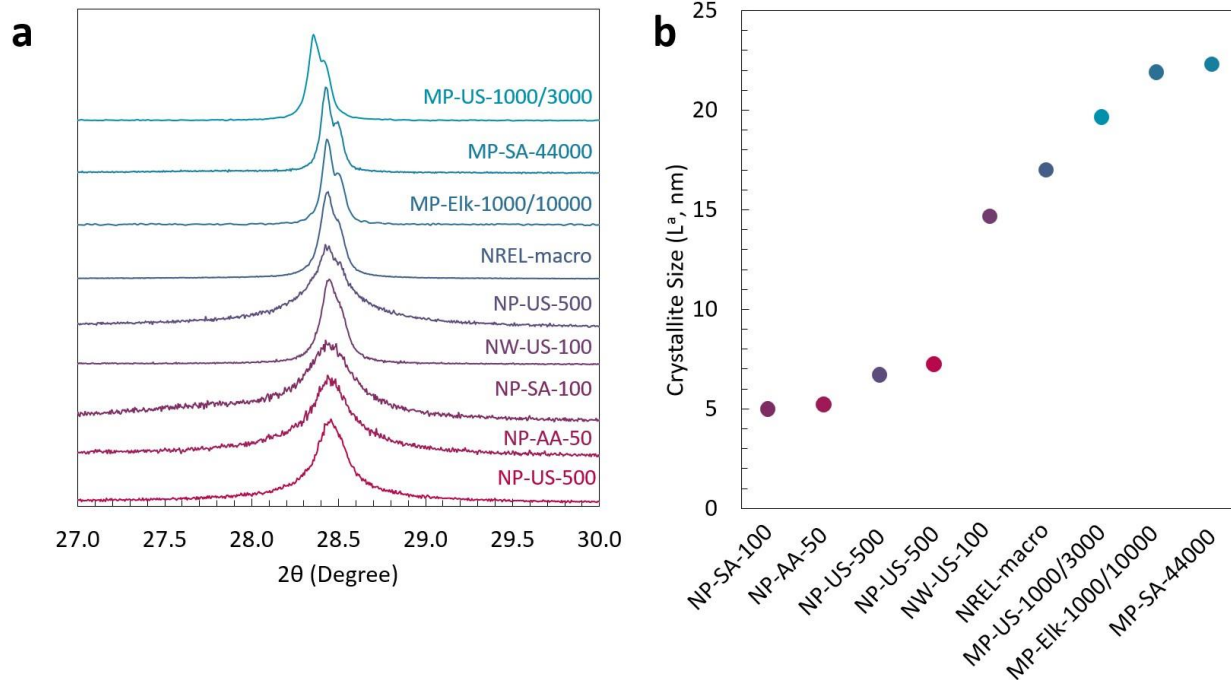
Figure J.1. (a) XRD pattern of the Si(111) reflection and (b) crystallite sizes of commercially available silicon.

Table J.2. Commercial Silicon Powder Structural Properties

Material ID	Si(111) 2θ (degree)	Lattice Parameter (Å)	Si(111) FWHM (degree)	Crystallite Size L_a (nm)
MP-US-1000/3000	28.35326	5.44555	0.08	20
MP-SA-44000	28.42472	5.43214	0.07	22
MP-Elk-1000/10000	28.42799	5.43152	0.07	22
NREL-macro	28.43386	5.43043	0.09	17
NP-US-500	28.43507	5.43020	0.22	7
NW-US-100	28.44489	5.42836	0.10	15
NP-SA-100	28.44648	5.42807	0.30	5
NP-AA-50	28.45092	5.42724	0.29	5
NP-US-500	28.45502	5.42647	0.21	7
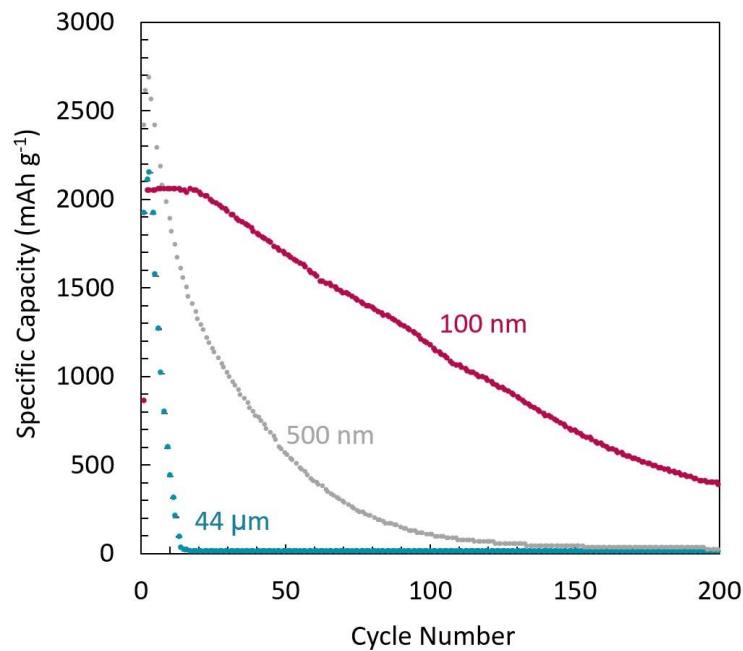
Figure J.2. GCD capacity retention of pure as-received 100 nm, 500 nm, and 44 μm Si NPs and MPs.

NP-SA-100 powder initially reigned as the model silicon material in this work owing to its cycling stability, uniform particle size (evidenced by SEM), and reproducibility in electrode casting relative to other commercial powders. Significant early work was done to vet phosphorus

doping and optimize electrochemical performance (exploring new electrolytes and additives) using this model material. Unfortunately, however, unforeseen batch to batch variability of the NP-SA-100 Si powder due to supply shortages during the Covid-19 pandemic ultimately led us to instead explore NP-US-500 as a model material and is the primary material studied in chapter 6.

APPENDIX K

THERMAL STABILITY OF PHOSPHORUS-DOPED SILICON ANODES
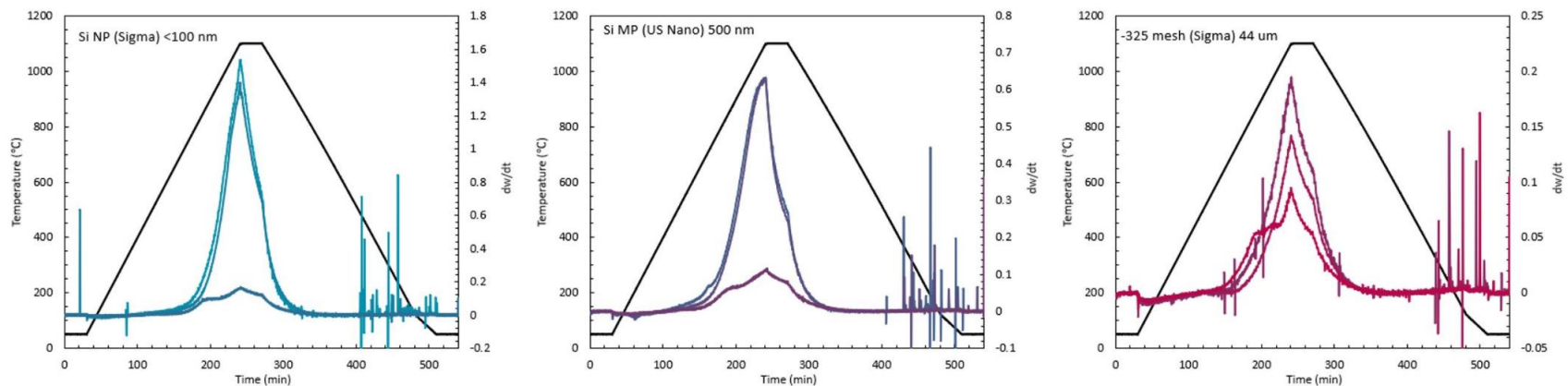
Figure K.1. Differential TGA profiles for three series of SiP$_x$ samples, based on three silicon precursors: (left) 100 nm NPs, (middle) 500 nm NPs, and (right) 44 μm MPs. The compositions of the samples are 0 at%, 0.1 at%, and 3.0 at% P in Si, from lightest to darkest.

Electrochemical isothermal micro-calorimetry data (Figure K.2) was collected by the Army Research Laboratory (ARL) under the ARL-MSU collaborative effort. 500 nm pure Si and heterogeneously doped SiPx (0.1P-L-50R-0h) electrodes were fabricated in coin cells with Li metal acting as the counter and reference electrode. 2 wt% VC + 5 wt% FEC in LP57 electrolyte (100 μL) was used. Cells were tested at 35 ℃. Over the course of 11 cycles SiPx samples demonstrate higher stability compared to pure Si NP.
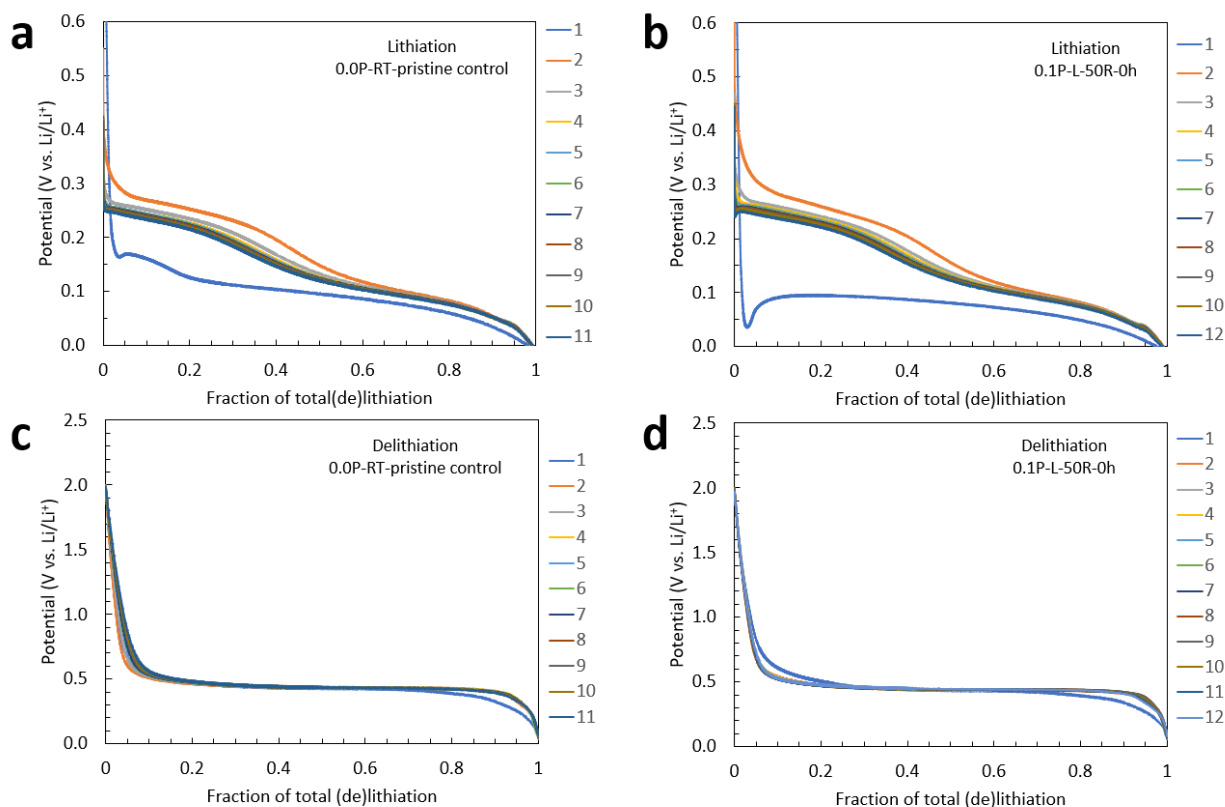
Figure K.2. Lithiation (a-b) and delithiation (c-d) potential curves for pure silicon and heterogeneously doped SiP$_x$ anodes at 500 μA at 35 ℃. Data was generated at Army Research Laboratory (ARL) under ARL-MSU collaborative effort.

APPENDIX L

EXPLORTION OF ALTERNATIVE DOPANTS IN SILICON

A natural extension of phosphorus-doped silicon presented in chapter 6 is to explore alternative dopants to include aluminum, boron, magnesium, and zinc. Goals of this work are to establish doping selection guidelines for silicon anodes based on dopant atomic size, electronegativity, valence and so on. Synthesis methods of SiM_x materials follow the same procedures as SiP_x (chapter 6). Both homogenously and heterogeneously doped SiM_x materials (where "M" = Al, B, Mg, P or Zn) containing 0.1 at% "M" were prepared. Commercial supplier, purity, and nominal composition of "M" dopants are listed in Table L.1 Homogenously doped materials are prepared at 1200 °C with a 5 °C min^{-1} ramp rate and 1 hr dwell time. Heterogeneously doped materials are prepared at 1200 °C with a 50 °C min^{-1} ramp rate and no dwell time. All characterization and cell assembly are performed as described in chapter 6 with the exception of 10 wt% FEC electrolyte additive instead of 2 wt%.

Table L.1. Alternative dopant's suppliers, purity, and nominal particle size

Dopant	Supplier	Purity %	Nominal Particle Size (μm)
Al	Sigma Aldrich	99.95	<75
B	Alfa Aesar	98.00	44
Mg	Sigma Aldrich	99.00	100
P	Sigma Aldrich	99.99	'powder/chunks'
Zn	Goodfellow	99.00	1-5

Relevant phase diagrams of "M" dopants are shown in appendix B. Table L.2 shows the eutectic temperatures, retrograde temperatures and maximum solubility of "M" dopants in silicon.

Table L.2. Eutectic temperature, retrograde temperature, and maximum solubility of dopants in silicon

Dopant	Eutectic Temperature (°C)	Retrograde Solubility Temperature (°C)	Maximum Solubility (at%)	Ref
Al	577	~1190	0.016	[257]
B	1385	--	3.00	[258]
Mg	947	~1200	0.03	[145]
P	1131	1180	2.4	[115]
Zn	419.58	~1350	0.00015	[259]

Based on computational calculations (Figure L.1) a contraction of the silicon lattice can be expected upon the addition of boron and phosphorus, whereas an expansion of the lattice is expected with the addition of magnesium, zinc, and aluminum. Figure L.2 shows powder X-ray diffraction data and lattice parameters of homogeneously doped SiM_x materials. Boron and phosphorus-doped silicon both show a contraction of the lattice parameter relative to pure silicon due to larger solubility limit within silicon (~1.2 and 3.0 at%). Magnesium, zinc, and aluminum, however, show negligible shift in lattice parameters relative to silicon owing to low solubility limits within silicon.
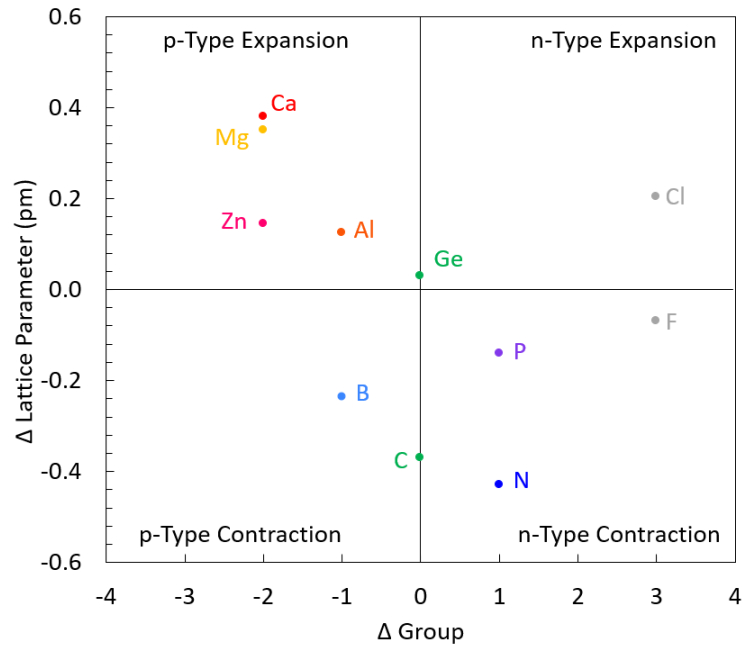
Figure L.1. Expected lattice shifts of p-type and n-type dopants with respect to silicon. Calculations were performed by Juan M. Marmolejo-Tejad.
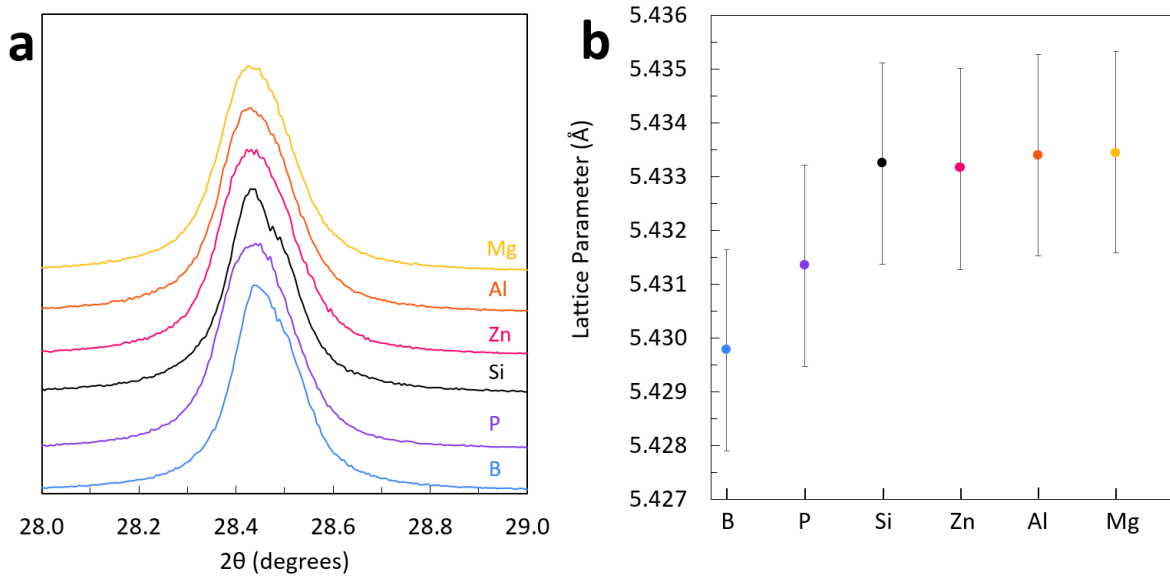
Figure L.2. Homogenously doped SiM_x synthesized at 1200 °C at 5 °C min^{-1} with a one-hour hold time. (a) Powder XRD of SiM_x and (b) lattice parameters. Error bars indicate instrument resolution error.

Bulk and surface Raman measurements of homogenously and heterogeneously doped SiM_x materials are shown in Figure L.3. It is important to note that measurements made at the surface and in the bulk were recorded respectively +10 and -10 µm from the detectors most intense point of focus. Almost all homogenously doped materials with the exception of $SiAl_x$ exhibit almost identical peak position for both bulk and surface measurements centered around ~513 cm^{-1}. Heterogenous SiM_x materials, on the other hand, have different peak centers for bulk and surface measurements. Consistently, peak centers of bulk measurements (503-506 cm^{-1}) are shifted to lower wavenumbers than surface measurements (506-510 cm^{-1}) confirming that doping under heterogenous conditions does in fact lead to different structural environments at the surface of silicon nanoparticles.

Peak broadness of heterogeneous SiM_x materials is larger than homogenous SiM_x materials. Pure silicon in the absence of any dopants was heat treated under homogenous conditions (1200 °C, 5 °C min^{-1}, 1 hour dwell) and also exhibit peak broadness similar to heterogenous SiM_x suggesting that narrowing of the Si peak FWHM is not dependent on the temperature heating profile but rather homogeneous distribution of dopants.
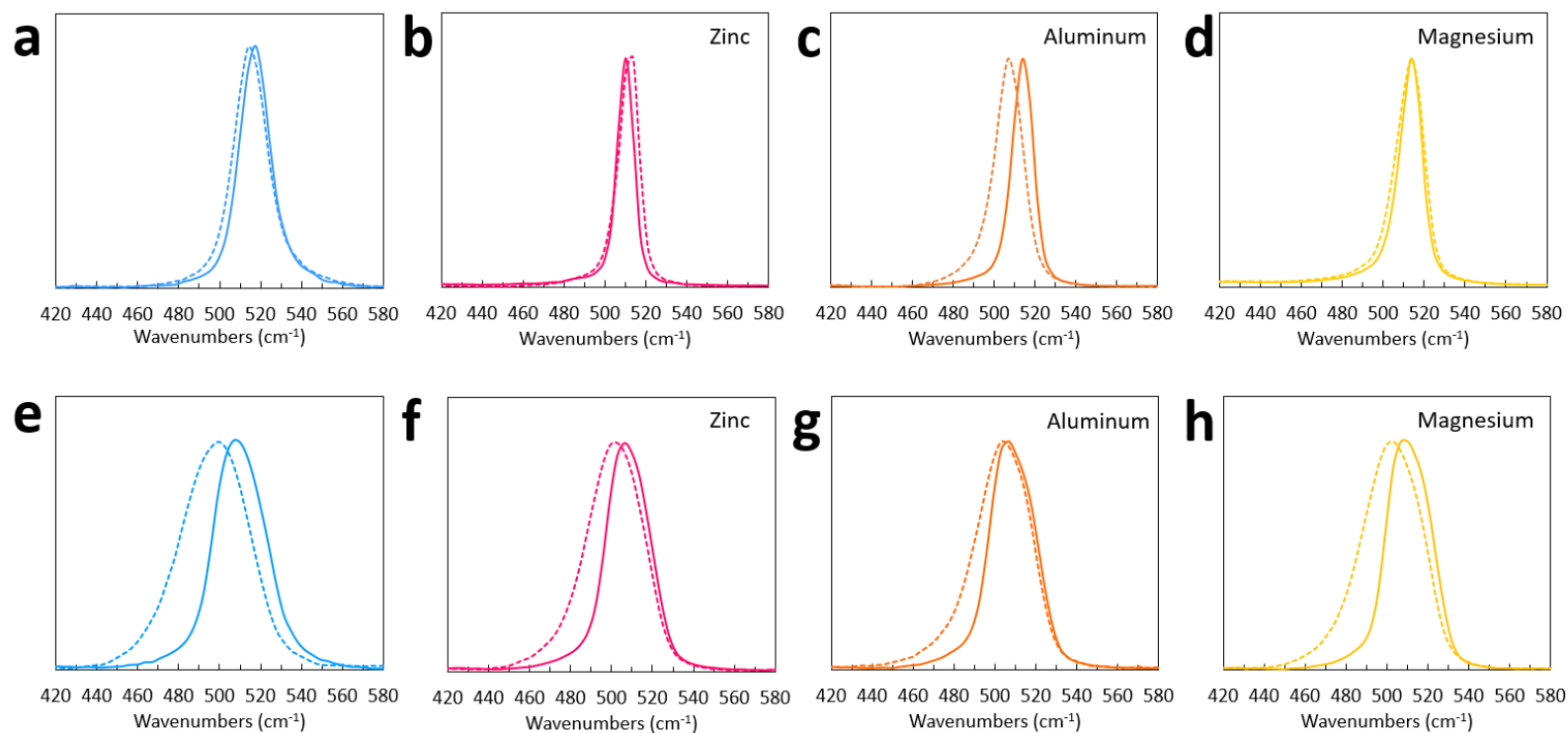
Figure L.3. Raman spectroscopy of (a-d) homogenously doped SiM$_x$ materials synthesized at 5 °C min^{-1} at 1200 °C for 1 hour and (e-h) heterogeneously doped SiM$_x$ materials synthesized at 50 °C min^{-1} at 1200 °C for 0 hours. Dashed and solid lines respectively represent bulk and surface measurements.

GCD lithiation of homogeneous and heterogeneously doped SiM_x materials are shown in Figure L.4. Homogenous doping by Al, B, Mg, and P inhibit cycling performance as compared to the pure Si electrode. Homogenous doping by Zn does not positively or negatively affect cycling performance of Si NPs which can be attributed to its nearly negligible solubility limit (0.00015 at%). In chapter 6 homogenously doped SiP_x materials demonstrated higher capacity and stability compared to pure Si NPs. The opposite is true in the work presented herein and can be attributed to the use of 10 wt% FEC additive instead of 2 wt%. All heterogeneously doped SiM_x materials improve cycling capacity and stability. Figure L.5. Shows overlays of homogenously and heterogeneously doped SiM_x materials. A divergence in capacity is observed after the first ~10 cycles.
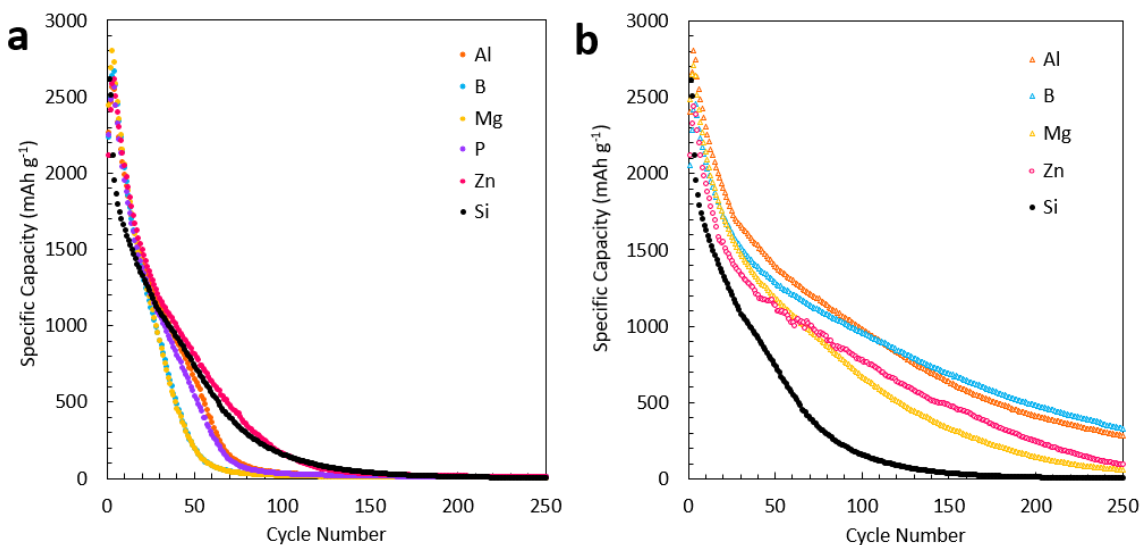
Figure L.4. GCD lithiation capacity retention of a) homogenously (0.1P-H-5R-1h) and b) heterogeneously (0.1P-L-50R-0h) doped silicon NPs.
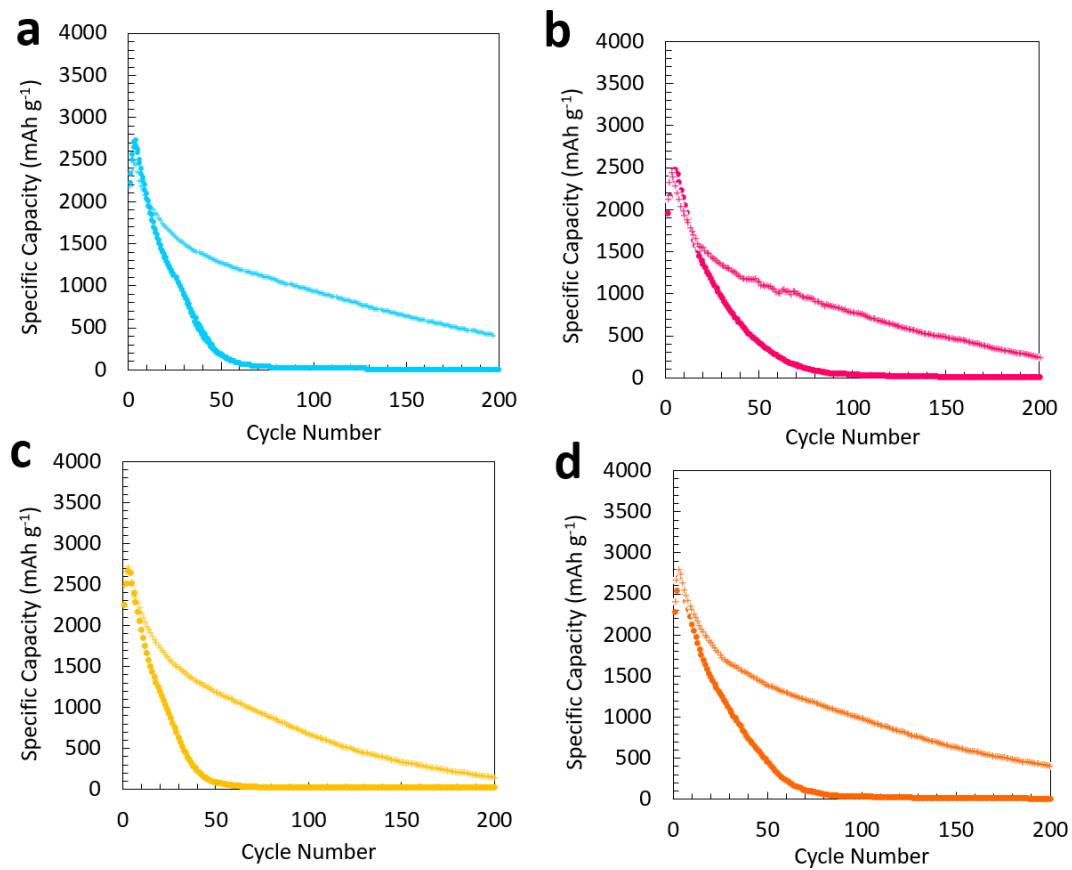
Figure L.5. GCD lithiation of a) boron-doped silicon, b) zinc-doped silicon, c) magnesium-doped silicon and d) aluminum-doped silicon. Homogenously (0.1P-H-5R-1h) and heterogeneously (0.1P-L-50R-0h) doped materials are shown by ○ and + symbols.